



Final Report for the Shuttle Flight Experiment on USMP-4: In Situ Monitoring of Crystal Growth Using MEPHISTO

R. Abbaschian
University of Florida, Gainesville, Florida

H.C. de Groh III
Glenn Research Center, Cleveland, Ohio

E. Leonardi and G. de Vahl Davis
The University of New South Wales, Sydney, Australia

S. Coriell
National Institute of Standards and Technology, Gaithersburg, Maryland

G. Cambon
Centre National d'Etudes Spatiales, Toulouse, France

The NASA STI Program Office . . . in Profile

Since its founding, NASA has been dedicated to the advancement of aeronautics and space science. The NASA Scientific and Technical Information (STI) Program Office plays a key part in helping NASA maintain this important role.

The NASA STI Program Office is operated by Langley Research Center, the Lead Center for NASA's scientific and technical information. The NASA STI Program Office provides access to the NASA STI Database, the largest collection of aeronautical and space science STI in the world. The Program Office is also NASA's institutional mechanism for disseminating the results of its research and development activities. These results are published by NASA in the NASA STI Report Series, which includes the following report types:

- **TECHNICAL PUBLICATION.** Reports of completed research or a major significant phase of research that present the results of NASA programs and include extensive data or theoretical analysis. Includes compilations of significant scientific and technical data and information deemed to be of continuing reference value. NASA's counterpart of peer-reviewed formal professional papers but has less stringent limitations on manuscript length and extent of graphic presentations.
- **TECHNICAL MEMORANDUM.** Scientific and technical findings that are preliminary or of specialized interest, e.g., quick release reports, working papers, and bibliographies that contain minimal annotation. Does not contain extensive analysis.
- **CONTRACTOR REPORT.** Scientific and technical findings by NASA-sponsored contractors and grantees.

- **CONFERENCE PUBLICATION.** Collected papers from scientific and technical conferences, symposia, seminars, or other meetings sponsored or cosponsored by NASA.
- **SPECIAL PUBLICATION.** Scientific, technical, or historical information from NASA programs, projects, and missions, often concerned with subjects having substantial public interest.
- **TECHNICAL TRANSLATION.** English-language translations of foreign scientific and technical material pertinent to NASA's mission.

Specialized services that complement the STI Program Office's diverse offerings include creating custom thesauri, building customized data bases, organizing and publishing research results . . . even providing videos.

For more information about the NASA STI Program Office, see the following:

- Access the NASA STI Program Home Page at <http://www.sti.nasa.gov>
- E-mail your question via the Internet to help@sti.nasa.gov
- Fax your question to the NASA Access Help Desk at 301-621-0134
- Telephone the NASA Access Help Desk at 301-621-0390
- Write to:
NASA Access Help Desk
NASA Center for Aerospace Information
7121 Standard Drive
Hanover, MD 21076



Final Report for the Shuttle Flight Experiment on USMP-4: In Situ Monitoring of Crystal Growth Using MEPHISTO

R. Abbaschian
University of Florida, Gainesville, Florida

H.C. de Groh III
Glenn Research Center, Cleveland, Ohio

E. Leonardi and G. de Vahl Davis
The University of New South Wales, Sydney, Australia

S. Coriell
National Institute of Standards and Technology, Gaithersburg, Maryland

G. Cambon
Centre National d'Etudes Spatiales, Toulouse, France

National Aeronautics and
Space Administration

Glenn Research Center

Trade names or manufacturers' names are used in this report for identification only. This usage does not constitute an official endorsement, either expressed or implied, by the National Aeronautics and Space Administration.

Available from

NASA Center for Aerospace Information
7121 Standard Drive
Hanover, MD 21076

National Technical Information Service
5285 Port Royal Road
Springfield, VA 22100

Available electronically at <http://gltrs.grc.nasa.gov/GLTRS>

Acknowledgments

The authors would like to thank CEA and the Société Européenne de Propulsion, France for their support during ground-based experiments and flight preparations. We would also like to acknowledge the entire USMP-4 team, especially Philippe Beaugrand, Kirk Beatty, P. Y. P. Chen, Victoria Timchenko, Vincent Gounot, Philippe Le, Regis Rieu, Bill Foster, Gil Santoro, Richard DeWitt, Minwu Yao, Nick Barbosa, Jeff Clancy, Gordon Seuell, and the superb support of the NASA Marshall USMP-4 team. Financial support for this research by NASA and the Australian Research Council is gratefully acknowledged.

Principal Investigator: Prof. Reza Abbaschian
Team members: F. Chen, J.R. Mileham, and Yunfei Lian
Department of Materials Science and Engineering
University of Florida
Gainesville, Florida 32611

Co-Investigator: Dr. Sam Coriell
National Institute of Standards and Technology
Gaithersburg, Maryland 20899



Co-Investigator and Project Scientist: Henry C. de Groh III
Project Managers: W.M. Foster II, R. DeWitt, and G.J. Santoro
NASA Glenn Research Center, M.S. 105-1
Cleveland, Ohio 44135
Phone: 216-433-5025



Co-Investigator: Prof. Graham de Vahl Davis
Team members: Prof. E. Leonardi, Dr. V. Timchenko,
Dr. P.Y.P. Chen, Dr. S.S. Leong,
J. Kaenton, and C. Benjapiyaporn
Computational Fluid Dynamics Research Laboratory
The University of New South Wales
Sydney, Australia 2052



THE UNIVERSITY OF
NEW SOUTH WALES

Team members: Prof. Suresh Garimella and J. Simpson
School of Mechanical Engineering
1288 Mechanical Engineering
Purdue University
West Lafayette, Indiana 47907-1288



Co-Investigator:
Team members:

Gerard Cambon
Sylvie Leon-Hirtz, Gabin Hieu, and Regis Rieu
Centre National d'Etudes Spatiales
Toulouse, France 31055



Team members:

Philippe Beaugrand, Vincent Gounot, Christophe Cordelle,
Phillippe Le, and Jean-Francois Pierre
Société Européenne de Propulsion
Small Propulsion and Equipment Department
Aerodrome de Melun-Villaroche
F 77550 Moissy-Cramayel, France

CEA

Team members:

Jean-Pierre Praizey, Jean-Philippe Nabet,
Jean-Paul Garandet, and Nellie Kernevez
Commissariat A L'Energie Atomique
DEM/Service Matériaux et Génie des Procédés/L.E.S.
CENG-85 X-38041 Grenoble Cedex, France

Table of Contents

	Page
Acknowledgments	iii
1. Summary	1
2. Overview	1
3. Background	2
4. USMP-4 Mission Description	3
4.1 Experimental Facility and Techniques	3
4.2 Experiments and Growth Conditions	5
4.3 Flight Summary	5
5. Microstructural and Data Analysis.....	6
5.1 Microstructural Analysis	6
5.1.1 Overview of Microstructural Evolution.....	6
5.1.2 Plane Front Solidification	6
5.1.3 S/L Interface Shape.....	6
5.1.4 Transition to a Cellular Growth Mode.....	7
5.2 Kinetics Data Analysis	7
5.2.1 Temperature Profile	7
5.2.2 Growth Rate Measurement	7
5.2.3 Interfacial Undercooling	8
5.3 Compositional Measurements	10
5.4 Structural Seebeck.....	11
6. Numerical Modelling	13
6.1 Introduction	13
6.2 Mathematical Formulation	13
6.2.1 Heat Transfer with Phase Change.....	14
6.2.2 Solute Transport with Phase Change	16
6.2.3 Extrapolation Scheme for Interface Concentration.....	17
6.2.4 Transition of Adiabatic Boundary Conditions	18
6.3 Solution Methods	19
6.4 Model and Code Validations.....	20
6.5 Preflight Modelling	21
6.5.1 Void Compensation	21
6.5.2 Analysis of Rehomogenization Times.....	22
6.5.3 Effects of g-jitter on Directional Solidification	23
6.5.4 Radial Segregation.....	24
6.6 Flight Experiment Modelling and Comparisons	25
6.6.1 MEPHISTO Events.....	25
6.6.2 Seebeck Signal	27
7. Conclusions and Discussion of Significant Findings.....	29
8. Success Assessment.....	30
Appendix A: List of Publications for MEPHISTO-2 and -4	33
Appendix B: MEPHISTO-4 Timeline, on USMP-4, STS-87	39
References.....	45
Tables	47
Figures	51

1. Summary

This is the final report submitted to NASA detailing the results of the MEPHISTO-4 experiment conducted on orbit in the cargo bay of NASA's Space Shuttle Columbia on STS-87, Nov. 19 – Dec. 5, 1997. This experiment was an international effort involving NASA, the Principal Investigator's institution – University of Florida at Gainesville, groups from France – which developed and built the MEPHISTO furnace, National Institute of Standards and Technology – which was responsible for analytical modeling, and groups from The University of New South Wales, Australia and Purdue University – who provided numerical modeling support. This was a solidification study in which three long rods of the metal Bismuth (Bi), mixed (alloyed) with 1 at% Tin (Sn), were directionally solidified. The scientific goals of this study were to: determine the relationship between the solidification growth velocity and the mode of growth at the growing solid/liquid interface (often termed morphological stability); determine the relationship between growth velocity and the temperature at the solid/liquid interface (often referred to as the undercooling, or supercooling, or interface kinetics); and determine the extent of atomic mixing of Sn atoms among the Bi atoms at the interface and in the liquid near the solid/liquid interface (termed the diffusivity of Sn in Bi). The general experimental goal of the project was for the melt to be stagnant, thus to solidify in an environment free of natural convection.

By all accounts the furnace hardware preformed flawlessly. All scheduled, and 22 additional, experiment cycles were completed during MEPHISTO-4. Examination of the space grown solid indicates that the samples grew with a planar solid/liquid interface at velocities less than 3.4 $\mu\text{m/s}$, and that cellular growth was present at growth velocities greater than 6.7 $\mu\text{m/s}$; these data characterize the morphological stability of this system under the conditions of these experiments (the temperature gradient in the liquid being 204 K/cm). It was found that grain orientation influenced the planar to cellular transition. The s/l interface was flat with slight concavity as viewed from the liquid. The steady nature of the Seebeck signal and temperature measurements indicate quiescent liquid, and taken together with the composition measurements (which indicate segregation profiles characteristic of a convection free environment) indicate diffusion dominated conditions were present during MEPHISTO-4. The Seebeck technique was used in an effort to determine the s/l interface temperature during growth. No problems with the use of this technique were observed during the flight experiment, however, to date, the analysis of the Seebeck results have not yielded a reliable measurement of the interface temperature. Through numerically modeling the system and comparing modeling results to concentration measurements in the solid, the diffusion coefficient of Sn in Bi was estimated to be $2.0 \times 10^{-9} \text{ m}^2/\text{s}$. The partition coefficient for Bi alloyed with Sn was measured and found to be $k = 0.029$.

2. Overview

This report summarizes the results of the In Situ Monitoring of Crystal Growth Using MEPHISTO (Material por l'Etude des Phenomenes Intéressant de la Solidification sur Terre et en Orbite) experiment on USMP-4 (the fourth United States Microgravity Payload). The report includes microstructural, compositional and the structural Seebeck data obtained during the post flight analysis, as well as numerical simulation of the flight experiment. The experiments were performed to gain a detailed understanding of the solidification and melting behavior of bismuth

alloyed with 1 at% tin. Two fundamental and interrelated aspects of the transformation from liquid to solid were studied: (a) morphological stability of the solid/liquid interfaces as affected by interfacial kinetics and anisotropy; (b) solute redistribution and materials transport kinetics. The goals of MEPHISTO-4, as stated in June 1996 at the Hardware Reflight Review, were:

G1. To determine the morphological stability threshold of faceted interfaces in the absence of convection and to understand the role of interface kinetics on the morphological stability under diffusion dominated conditions.

G2. To determine Bi growth kinetics as a function of orientation and to use the data to calculate the step edge free energy and the atomic mobility at the interface as a function of supercooling.

G3. To obtain a conclusive ruling on the kinetic roughening phenomenon and diffusiveness of the interface.

The research program was conducted with the collaboration of a multi-national team involving the University of Florida (UF), NASA Glenn Research Center, the National Institute of Standards and Technology (NIST), and Purdue University in the USA, the Centre National d'Etudes Spatiales (CNES), Departmente d'Etudes des Materiaux at Commissariat A L'Energie Atomique (CEA) and the Societe Europeenne de Propulsion (SEP) in France, and The University of New South Wales (UNSW) in Australia.

The experiments utilized MEPHISTO hardware to study the solidification and melting behavior of bismuth alloyed with 1 atomic percent (at%) tin. The experiments involved repeated melting and solidification of three samples, each approximately 900 mm long and 6 mm diameter. Half of each sample also included a 2 mm diameter growth capillary, to assess the possible influence of the sample diameter on the growth and mass transport. One sample provided the Seebeck voltage generated during melting and freezing processes. Another one provided temperature data and Peltier pulsed demarcation of the interface shape for post flight analysis. The third sample provided resistance for velocity measurements, as well as additional thermal data. The third sample was also quenched at the end of the mission to preserve the interface composition for post flight determination. A total of more than 450 mm of the alloy was directionally solidified at the end of the flight for post mission structural and compositional characterization. Metallurgical analysis of the samples has shown that the interfacial kinetics plays a key role in controlling the morphological stability of faceted alloys. Substantial differences were observed in the Seebeck signal between the ground-based experiments and the space-based experiments. The temperature gradient in the liquid for the ground-based experiments was also significantly lower than the gradient in the liquid for the space-based experiments. Both of these observations indicate significant influence of liquid convection for the ground-based experiments.

3. Background

The formation of dendrites generally follows morphological instability of a planar solid/liquid interface [Coriell and McFadden, 1993]. The morphological stability criterion of Mullins and Sekerka, 1964, can be utilized to predict the onset of instability in planar interfaces. The criterion determines the conditions for the growth or decay of a perturbation on a planar interface under a given steady state condition. More recent theoretical models indicate that

anisotropic interfacial properties play a role in the morphological stability of planar interfaces, as well as the evolution of cellular and dendritic structures; this has been predicted theoretically by Coriell and Sekerka, 1976, and Coriell *et al.*, 1994, by extending the linear stability analysis of Mullins and Sekerka, 1964, and by Young, Davis, and Brattkus, 1987, in the weakly nonlinear regime. These treatments indicate that such anisotropies tend to stabilize the growth of a planar interface. Experimental observations reported by Tiller and Rutter, 1956, for lead-tin alloys and by Trivedi, 1990 and Trivedi, Seetharaman, and Eshelman, 1991, for transparent organic systems have been found to be generally consistent with the theoretical predictions.

The influence of anisotropic interfacial kinetics on the morphological stability threshold was recently demonstrated by the present investigators for solidification of bismuth alloyed with 0.1% Sn [Abbaschian *et al.*, 1995; Abbaschian *et al.*, 1996]. The experiments were conducted under microgravity conditions during STS-62 (Shuttle Transportation System) flight of the space shuttle Columbia, using the MEPHISTO directional solidification facility. Similar to the USMP-4 experiments, the experiments yielded 150 mm of three parallel-processed samples, each grown directionally at six velocities ranging from 1.85 to 40 $\mu\text{m/s}$. The microstructural evaluation of the space grown samples indicated that for 1.85 and 3.4 $\mu\text{m/s}$ interface velocities, the growth occurred in a planar mode. The microstructural evolution at a higher velocity of 6.7 appeared to be cellular in one grain, and planar in another, whereas for 13.3, 26.9 and 40 $\mu\text{m/s}$ velocities, cellular/dendritic morphologies were observed in both grains. The most interesting aspect of the planar-cellular transition at 26.9 $\mu\text{m/s}$ velocity was the existence of distinct preferential breakdown in one grain versus the other. One grain became cellular approximately 0.6 mm after the initiation of growth, forming cells, which were tilted about 6.5° with respect to the heat flow and growth directions. The neighboring grain, on the other hand, continued with planar growth for about 12.2 mm until it became cellular, with cells parallel to the growth direction. The cell spacing within the two grains was approximately the same; 265 and 276 μm , respectively.

The USMP-4 flight experiments were intended to build on the findings of USMP-2 flight [Abbaschian *et al.*, 1995; Abbaschian *et al.*, 1996]. In particular to provide additional data on the dominant role of interfacial kinetics on the morphological instability of facet forming materials. Since the interfacial kinetics and morphological instabilities also depend on the solute concentration, obtaining additional data at a higher solute concentration was also another aim of the experiment. As such, the Sn concentration for the USMP-4 flight was selected as 1 at% Sn instead of the 0.1 at% used for the USMP-2 flight.

4. USMP-4 Mission Description

4.1 Experimental Facility and Techniques

The MEPHISTO hardware is shown schematically in Figure 1 [Abbaschian *et al.*, 1995; Rouzard, 1988]. The apparatus is capable of simultaneous processing of three rod shaped samples, each of which is approximately 900 mm in length, 6 mm in diameter, and contained in 10 mm outer diameter silica tubes. The central part of MEPHISTO consists of two furnaces each with a neighboring heat sink, which is cooled by a refrigerant. One of the furnace-heat sink structures is stationary, while the other is on a moving platform. Between these heaters, special

reflectors and insulation are used to maintain a nearly uniform temperature. For the experiments, the furnaces were heated to 750° C, while the cold zones were kept near 50° C, resulting in a molten zone in the middle of each as illustrated in Figure 1. When the movable furnace-heat sink structure is translated away from the fixed furnace, the extent of the hot zone is lengthened, increasing the extent of the molten zone in the sample. Near the solid-liquid interfaces, which are located between each furnace and its accompanying heat sink, a temperature gradient on the order of 200° C/cm is established. The furnace heaters are in contact with cylindrical thermal diffusers made of graphite and are regulated using thermocouples within the diffusers. The graphite diffusers have three holes to accommodate the samples. The uniform temperature field produces a very similar thermal profile for the three samples. In order for the heat sinks to efficiently remove the heat from the samples, a metal seal of a low melting point (45° C) alloy was utilized. When the heat sink reached its operating temperature, the liquid alloy of the seal made a direct contact between the heat sink and the outer silica wall of the samples.

The alloy used for the experiments was Bi with 1 at% Sn. As shown in Figure 2, Bi and Sn form a simple eutectic diagram, with a maximum solubility of 1.63 at% Sn at the eutectic temperature of 140° C. The distribution coefficient for Sn in Bi was measured to be around 0.03 (Abbaschian, unpublished work). Schematics of the three samples inserted into the MEPHISTO apparatus and their dimensions are shown in Figure 3. Each of the three samples, which will be referred to as the "Quenching", "Peltier", and "Seebeck", has a special purpose in the study of alloy solidification. A 2 mm ID, 3 mm OD silica capillary is located on the moving furnace side, which extends about 250 mm into the sample. Thin capillaries (approximately 0.6 mm OD) for the thermocouples were also inserted for the thermocouples in the Peltier and Quenching samples. The capillaries were filled with the alloy during sample preparation. The samples used in the ground-based processing were similar except the capillaries were about 40 mm shorter.

The Quenching sample is used to measure the rate of solidification using the resistance change across the sample during processing and to produce a short quenched section near the interface at the end of the experiments. To achieve the latter, the sample is attached to a mechanism which quickly pulls the sample about 2 cm towards the cold zone and freezes the sample. The Quenching sample was electrically connected for the resistance measurements. The contact for the Quenching sample on the capillary side is with the alloy outside the capillary, insulated from the alloy in the center by silica. The change in the resistance of the sample was used to calculate the solidification rate as will be explained later in the report.

The Peltier sample has connections to allow marking the sample with short electrical pulses which cause heating or cooling at the solid-liquid interface according to the equation:

$$Q_p = -(\pi_s - \pi_L) J \Delta t$$

Q_p is the heat generated at the solid-liquid interface, π_s and π_L are the Peltier coefficients of the solid and liquid alloy, respectively, J is the current (positive for flow from solid to liquid), and Δt is the pulse duration. As shown in Figure 3, a small slit was put in the capillary to allow current pulses to pass through the entire sample during Peltier pulsing. If the current direction results in cooling at the interface, the rate of solidification will momentarily increase and there will be a buildup of solute at the interface.

The Seebeck sample is used in theory to measure the difference between the temperature of the stationary and moving solid-liquid interfaces. The relationship between the measured Seebeck signal and the temperature of the moving interface, TC, and the temperature of the stationary interface, TD, will be discussed together with the experimental results. Details of Seebeck interface temperature measurement can be found elsewhere [Peteves, 1986].

4.2 Experiments and Growth Conditions

The flight experiments were performed with the help of Société Européenne de Propulsion (SEP) by telecommanding. The experiments were initiated by heating the movable and stationary furnaces to 750° C. This established a liquid zone approximately 340 mm long as depicted in Figure 1. Melting and solidification experiments were performed by commanding the apparatus to move the mobile furnace/heat sink structure. The fully open position was referenced as 1 mm and the fully closed 150 mm. Increasing the furnace position corresponded to freezing and decreasing the furnace position to melting. Figure 4 is a plot of the MEPHISTO movable furnace position during the USMP-4 mission. More detailed timeline can be found in Appendix B. Many of the experiments consisted of a freezing period where the furnace was moved forward, a hold period where the furnace was kept stationary, and a melt period where the furnace was moved back to the original position. Figure 5 is an example with a start position of 115 mm, freezing for 15 mm at 13.5 $\mu\text{m/s}$, and a hold period of 30 minutes, and then melting back to the 115 mm position at 13.5 $\mu\text{m/s}$. The detailed analysis of the Seebeck, resistance and thermocouple measurements benefited from the large number of experiments performed aboard USMP-4. As shown in Figure 4, the experiments included thirty-five freeze-hold-melt cycles during the mission and eleven periods of final directional solidification. The experiments were performed over a range of solidification rates from 0.74 to 40 $\mu\text{m/s}$.

The MEPHISTO apparatus monitored many of the growth conditions using the furnace position, thermocouples, change of sample resistance, Peltier interface demarcation, and Seebeck measurements. In the following section, the use of these measurements/techniques to determine the temperature gradients (in the solid and liquid), growth velocity, and interface undercoolings will be explained and applied to both the ground- and space-based experiments.

4.3 Flight Summary

The entire flight experiment was commanded and controlled via telemetry from the NASA-Marshall Payload Operations and Control Center. The performance of the hardware and samples, and the quality of telemetric data received were superb throughout the entire mission. We gathered approximately 0.5 Gb of data for 35 Seebeck solidification and melting cycles. The experiment covered a range of velocities as low as 2.67 millimeters per hour (mm/hr) to as high as 144 mm/hr (0.1-55 inches per hour). Thirteen of these Seebeck cycles were as planned in the original timeline. The productivity and quality of the science and engineering teams and hardware performance provided the opportunity for the additional 22 cycles. It should be noted that lowering the design velocity specification for MEPHISTO performance by a factor of more than two beyond its original specifications clearly indicates the outstanding design and workmanship of the hardware. In addition, 150 mm of each sample was directionally solidified at the end of the mission, with

different velocities from 6.6 to 144 mm/hr, providing 450 mm of directionally grown samples under microgravity environment. The resistance sample was quenched at the end of the mission.

5. Microstructural and Data Analysis

5.1 Microstructural Analysis

5.1.1 Overview of Microstructural Evolution-Figure 6 shows a general view of the flight samples processed. An overview of the microstructural evolution of the samples grown in space was obtained from the low magnification composite of a microsection of all three samples. Figure 7 shows the location and orientation of the microsection with respect to the furnace graphite diffuser center. Note that the microsection orientations of all the samples were cut so that they are thermally equivalent. The growth conditions during the final solidification are summarized in Table 1. The micrographs in Figures 8(a)-(b) show the successive development of the microstructure as a function of the distance and the growth velocity for the Seebeck sample. The overall microstructural features of the sample, as is shown in Figure 8 and schematically in Figure 9, can be categorized as follows: (1) The cellular/dendritic region of the earth grown sample; (2) The plane front directionally solidified positions grown at velocities V1 and V2, or at the beginning of cycles at the other velocities; (3) The cellular region directionally solidified at velocities V3 and higher; (4) The microstructures formed at the end of cycles at velocities V3 and higher by the coarsening of the two phase cellular regions. A summary of processing lengths and velocities as well as the microstructure in each section is shown schematically in Figure 9. The successive development of the microstructure as a function of the growth velocity can also be seen. As detailed later, for solidification at velocities below V2 the growth occurs in a planar mode, while cellular morphology is seen at V3 through V6 velocities. The planar to cellular transition reveal many important aspects of the solidification of faceted materials in microgravity as discussed in more detail in the following section.

The initial (Earth grown) microstructure of the samples is shown in Figure 10. The samples were produced from a homogeneous liquid through quenching. The optical micrograph in Figure 10 shows relatively uniform microstructure with a faceted cellular/dendritic morphology.

5.1.2 Plane Front Solidification-The development of a plane-front microstructure is illustrated in Figures 11(a)-(c) which show the transition from a facet cellular/dendritic structure of the Earth-grown portion of the samples to a plane-front morphology at the moving furnace interface. At all three interfaces, the initial cellular to plane-front transition interface was sharply delineated. The optical micrographs show that only a few dominant orientations emerge from the initial microstructure, which was found to be a common feature of all three samples. The microstructure is characterized by a complete absence of the Sn-rich second phase indicating plane-front solidification. It was found that the interface was associated with a sharp compositional change, detected via electron microprobe analysis as presented later.

5.1.3 S/L Interface Shape-When an interface was revealed, for example during the interface breakdown, it was found that the interface was nearly flat, with a slight curvature near the s/l/crucible triple junction. Upon closer examination, the boundary across each grain appears to

be fairly flat, with the small angles between them giving the appearance of an overall slight curvature of the interface, as shown by the micrograph of the interface where the sample was quenched in Figure 12.

5.1.4 Transition to a Cellular Growth Mode-Microstructural examination of the microgravity-processed sections indicated that those regions of samples grown at V3 through V6 velocities exhibited a morphological transition to a cellular growth mode. The microstructural appearance of the cellular breakdown of event 15, V5 (Peltier sample) is shown in Figure 13. Figure 14 shows the planar to cellular transition, at velocity V4 for the Seebeck sample. A much narrower planar to cellular transition zone was seen at a higher growth velocity (V5, V6) than that at lower growth velocity (V3, V4). The distances from the initiation of the growth to the position where the cellular microstructure was observed, called the incubation distance, for the samples are given in Table 2. It should be noted that for velocities V1 and V2, because of the short solidification distance, no cellular morphology was observed. For the other velocities, the incubation distance varied slightly from one grain to another, as well as within and outside of the capillary. Figure 15 gives the breakdown distance as a function of growth velocity.

5.2 Kinetics Data Analysis

5.2.1 Temperature Profile-The thermal profiles in the MEPHISTO apparatus were monitored using nine thermocouples located in each of the furnace diffusers and heat sinks. Four thermocouples were also placed inside the small silica capillaries within the Quenching and Peltier samples. The thermocouples in the heater and heat sink diffusers were used to control the overall thermal conditions of the furnace. The thermal profile of the samples, however, is not fully determined by the temperatures imposed by the diffusers, but also by the properties of the sample to be processed. Therefore, the temperature field in the samples was monitored using the four experimental thermocouples located within the samples. A typical thermal measurement by three of the thermocouples is shown in Figure 16. Also shown in the figure are the corresponding furnace position and the melting temperature. The temperature gradients in the solid and liquid near the interface were measured as 260 and 204 K/cm, respectively, for growth within the 6 mm silica tube.

Figure 17 gives the temperature profile for ground- and space-based experiments within the Peltier sample using thermocouple T4 in the ground-based experiment, and T4 and T6 in the space-based experiments. (The positions of these thermocouples are marked in Figure 3.) Note the temperature gradient for the space-based experiments within and outside the capillary for the space-based experiments are both about 260° C/cm. The thermal profile in the solid (below about 270° C) for the ground-based experiments is very similar to the space-based measurements. However, the average temperature gradient in the liquid for the ground-based mission is only about 100° C/cm.

5.2.2 Growth Rate Measurement-In the MEPHISTO apparatus there are two complementary techniques for ascertaining the solidification rate during an experiment. The simplest method is to use the translation rate of the MEPHISTO Moving Furnace. Since the temperature gradient in the MEPHISTO apparatus is fairly steep, it is anticipated that the moving interface would follow the movement of the moving furnace very closely. However, the interface movement may not

exactly correlate with the furnace translation because of the thermal lag between the temperature imposed on the exterior of the ampoule and the temperature within the sample. The decrease in the melting temperature of the solid-liquid interface because of the buildup of solute at the moving interface would also cause the interface to lag the furnace. In addition to this chemical undercooling, there is also a kinetic undercooling associated with a finite growth rate for faceted interfaces.

A more accurate determination of the interface migration was made from the change in resistance of the Quenching sample. The resistance change as a function of the processing time during a typical cycle is shown in Figure 18, together with the furnace position. The small steps in the resistance data are due to the resolution of the measurements. While the two data sets correlate nicely, more detailed analysis show that there is a slight lag in the resistance change at the beginning of solidification. The resistance of the sample is the sum of the contributions from the solid and the liquid. When a section of liquid is replaced by solid the change in resistance is:

$$\Delta R = \frac{\Delta L_1 \rho_1}{A_1} + \frac{\Delta L_2 \rho_2}{A_2}$$

where ΔR is the change in resistance, ΔL is the change in length, ρ is the resistivity, and A is the cross-sectional area. The subscripts 1 and 2 refer to the solid and the liquid respectively. Figure 19 is a plot of the Quenching sample resistance as a function of the movable furnace position. Two different lines are used to fit the data. The dashed line is for resistance measurements within the capillary, while the solid line fits data outside the capillary. The steeper slope within the growth capillary is due to the smaller cross-sectional area for A_1 and A_2 .

5.2.3 Interfacial Undercooling-A non-intrusive technique for studying interfacial undercooling is to measure the Seebeck signal generated by a solid-liquid-solid structure [Peteves and Abbaschian, 1991, and Sixou, Rouzaud, and Favier, 1994]. The technique in theory enables a quantitative investigation of interfacial undercooling including compositional and kinetic terms. For the current loop pictured in Figure 1, if it is assumed that the Seebeck coefficients for the solid and liquid do not vary with concentration, temperature or structure, the resulting signal for the simplified conditions will be:

$$E_s = \eta_s(T_c - T_B) + \eta_L(T_E - T_D) + \eta_s(T_E - T_D)$$

where η_s is the Seebeck coefficient for the solid, and η_L is the Seebeck coefficient for the liquid. For the setup shown in Figure 1, T refers to temperature, and the subscript, the position, and the wires from A to B and F to E are the same material. The MEPHISTO apparatus can monitor and control the end temperatures of the sample to within 0.01°C , as such $T_B=T_E$ and $T_A=T_F$, the above equation therefore, simplifies to $E_s = -(\eta_s - \eta_L)(T_D - T_C)$. If the Seebeck coefficient of the liquid and solid are known, then one can determine the difference in temperatures of the two solid-liquid interfaces. The temperature at the stationary interface, T_D , is given by the phase diagram in Figure 2. The temperature of the moving interface, T_i is given by

$$T_i = T_l + \frac{E_s}{\eta_s - \eta_L} = T_l + \frac{E_s}{\eta_{s/L}}$$

where η_{SL} is the difference in the Seebeck coefficient of the solid and liquid near the melting temperature. It should be noted that the above-mentioned simplification is not correct for non-isotropic and non-homogeneous materials, such as the alloy for the present experiments. More accurate determination requires the contributions from the solid sample as it translates through any temperature gradient. The overall Seebeck voltage will be given by:

$$E_s = \int_A^F \eta(\phi(w), c(w), \theta(\bar{w}), T(w)) \nabla T \cdot d\bar{w}$$

where w is the path, η is the Seebeck coefficient, and ∇T is the temperature gradient. Here we have assumed the Seebeck coefficient depends on the phase of material, ϕ , the composition, c , and the crystallographic orientation, θ . For the equation to be valid, a necessary condition is that the integral does not depend on the path taken within the material. This could be violated, for example, if there are alternate paths through materials with different Seebeck coefficients. This generalized equation included contributions to the Seebeck voltage from the temperature difference at the two interfaces as well as from the solidified structure behind the interface. The determination of the "Structural Seebeck" contribution is described later. Although estimates of the structural Seebeck were made, no estimate of the kinetic undercooling that we consider reliable was successful.

Figure 5 gives the Seebeck signals acquired for a ground- and a space-based experiment. Each consisted of solidification, hold, and melt period as previously described. The Seebeck signal for the ground-based experiment rose during freezing, fluctuated around an average value for the hold, then decreased during melting. The fluctuations in the signal are due to hydrodynamic mixing in the liquid. It was observed that the magnitude of the fluctuations strongly depended on the maximum temperature of the melt. The signal for the space-based experiment had an initial increase, then decreased during freezing. After the furnace stopped, the signal increased due to the interface temperature increase caused by the exponential decay of solute at the interface. During melting the signal decreased, then increased back to near its initial value before the freeze-hold-melt cycle was began. The differing behavior of the ground- and space-based Seebeck results may be due to the differences in the amount of solute buildup at the interfaces as well as structural changes in the solid. As discussed later, the structural Seebeck contributions were determined from post-flight sample analysis, which enabled us to calculate the net interfacial contributions to the measured Seebeck voltage.

As indicated earlier, the temperature gradient in the liquid, G_L , for the ground-based mission was significantly smaller than G_L for the space-based experiments. This is evidence of hydrodynamic mixing on the ground-based experiments, as well as the differences in the heat transfer coefficient between the metals, the silica tube, and the surrounding graphite diffuser. The existence of hydrodynamic mixing during the ground-based experiments with a maximum liquid temperature of about 750° C is further supported by fluctuations in the Seebeck signal while the mobile furnace/heat sink structure was at rest. Figure 20 shows the moving and fixed furnace diffuser temperatures and Seebeck signal during part of the heat-up of the MEPHISTO furnaces. When the fixed furnace diffuser temperature was held at 400° C, fluctuations in the Seebeck signal are not noticeable. However, as the temperature of the fixed furnace diffuser rose above 550° C, strong fluctuations in the Seebeck signal become apparent, presumably from the onset of

strong hydrodynamic mixing in the liquid. Fluctuations in the Seebeck signal were not observed for the space-based experiments.

5.3 Compositional Measurements

For solidification of Bi-Sn alloys, the concentration of the solute, in the solid at the interface is considerably smaller than that in the liquid. The ratio of the two solute concentrations is given by the distribution coefficient k , which is approximately 0.03 according to the phase diagram shown in Figure 2. For growth into a liquid with C_0 composition, the initial solid concentration is kC_0 . Because of the solute rejection, Sn builds up ahead of the interface, resulting in an increase in the solute concentration of the subsequent solidification segment. Eventually a steady growth is reached when the solid concentration reaches C_0 . The length of the initial transient region before the establishment of the steady state growth is approximately $4D/\nu k$, where D is the diffusion coefficient for Sn in liquid Bi, and ν is the growth velocity. For the present experiments, since both k and ν are small, the solidification cycles do not reach steady growth for any of the plane front solidification performed at velocities V_2 or lower. For the higher velocities, the interface becomes cellular before reaching a steady state growth.

During the hold period at the end of a plane front solidification, the solute buildup ahead decays by the diffusion of Sn into the remaining liquid. As a result, the next growth cycle again initiates with kC_0 composition, and goes through another initial transient. It should be noted that when the interface becomes unstable by the formation of the cells, the solute rejected away from the interface is interrupted by the deposition of Sn at the cell boundaries. During the hold period, the two-phase cellular region goes through a coarsening process, leading to the formation of a plane front before the initiation of the next growth cycle.

Microprobe analyses were performed to determine the solute concentration throughout the directionally solidified samples. The analysis used a 10 μm beam at 15 kV accelerating voltage. Pure Bismuth (99.99999% metal base purity) and Tin (99.999%) were used as standards.

Figure 21 shows an example of the microprobe line scan measurement at the centerline of the capillary tube for the Seebeck sample. The line scan, which included a portion of the earth-grown sample, covered plane front solidification sections at velocities V_1 (1.8 $\mu\text{m/s}$), V_2 (3.4 $\mu\text{m/s}$) and V_3 (6.7 $\mu\text{m/s}$). The sections correspond to event 11A, 11B and 12 shown in Figure 4. The location of the line scan is also shown by the line #2 on the sample cross section shown in Figure 22. As can be seen, the Sn concentration in the earth grown portion varies considerably with distance because of the cellular structure in this section. For the plane front solidification at the other velocities, on the other hand, the solute concentration increases gradually from the start of solidification until the growth was stopped. For the growth at V_3 , the growth became cellular at the end of the measurement location. As discussed in the numerical simulation section, the solute buildup data in these sections were used to estimate the diffusivity of Sn in liquid Bi.

The radial segregation profiles in the 6 mm section of the Seebeck sample during the plane solidification at velocities V1 and V2 (corresponding to events 11E and 11F in Figure 4, respectively) are shown in Figure 23. The line numbers correspond to those drawn in the micrographs of Figure 22. For clarity of the compositional data presentation, the Y-axis in Figures 23 and 24 are equal to the line number (20, 21, etc) plus the measured composition at each location. Similar radial composition measurements for the Quench sample during events 11E and 11F are shown in Figure 24, with the corresponding line positions shown in Figure 25. An example of the compositional determination outside the capillary tube is shown for the Peltier sample in Figure 26. The data corresponds to the event 11A and 11B for the lines shown in Figure 27.

5.4 Structural Seebeck

The total Seebeck voltage, ΔE , measured through the circuit shown in Figure 1 is generated through the three separate but interrelated components, ΔE_c , ΔE_k and ΔE_s , as described below:

1. ΔE_c is the voltage generated because of the temperature difference between the stationary and moving interface, ΔT_c , as a result of the solute buildup at the moving interface;
2. ΔE_k is the voltage generated because of the kinetic undercooling, ΔT_k , at the moving interface;
3. ΔE_s is structural Seebeck voltage generated by the translation of a non-homogeneous and non-isotropic solid sample through a temperature gradient behind the interface.

The compositional component will depend on the solidification velocity and distance solidified, whereas the kinetics component will mostly depend on the velocity, orientation and the nature of the interface. For a faceted interface, the interfacial kinetics depends on the growth mechanism, 2-D nucleation and growth versus dislocation-assisted growth [Coriell and McFadden, 1993, Mullins and Sekerka, 1964]. The structural component of the Seebeck, on the other hand, depends on the structure and composition of the solidified sample. This component was approximately determined by post-flight measurements as described below. It should be noted that the measurements were done on the as-grown space processed sample, and prior to its sectioning for microstructural and compositional analysis.

The experimental setup used to measure the structural Seebeck of the sample is schematically shown in Figure 28. The setup consisted of two constant temperature compartments, separated by insulation, through which the sample was passed. The temperature of one compartment was maintained at 20° C, and the other at between 40 and 95° C using constant temperature water circulators. An O-ring mechanism allowed for the translation of the sample through the separation wall; a temperature gradient of about 200° C/cm was achieved in the sample. The two ends of the sample were connected by copper wires to a nano-voltmeter and data recording system. The actual temperature gradient in the sample was determined by a sample which contained a thermocouple, similar to the quenching sample. The temperature gradients measured with the hot end of the sample at 75 and 95° C are shown in Figures 29 and 30, respectively.

For the structural Seebeck determination, the space grown Seebeck sample was placed in the apparatus and electrically attached to the nano-voltmeter as outlined previously. Then using a rod connected to a translation stage controlled by computer, it was translated from the cold zone to hot zone at a pre-determined rate of 0.29 mm/s. Figure 31 shows the thermoelectric voltage generated during the experiments under five different temperature settings. It should be noted that the cold end temperature for all the measurements was 20° C. The position designated by zero in the x-axis corresponds to the initiation of the space-grown sample. The results show that the Seebeck voltage responds in a systematic manner to the changes in the microstructural and/or compositional changes in the sample.

Although the sample is an inhomogeneous material because of its microstructure shown in Figure 8, it can be divided into several sections based on their similar microstructure features within the same segment. These segments included (1) earth grown section, (2) plane front space grown sections, (3) cellular space grown regions, and (4) the coarsened mushy regions. If we assume these segments are homogeneous, an average Seebeck coefficient can be assigned for each section. Thus the Seebeck voltage generated by each segment is only dependent on the temperature at both ends of the segment. Total Seebeck emf output of the sample would be the algebraic sum contributed by each segment. Given all the above, we can have the following equation for the total structural Seebeck generated:

$$V_S = \int_{x_B}^{x_E} \eta(\alpha) T'(\alpha) d\alpha$$

where η is the Seebeck coefficient, T is the temperature profile and V_S is the structural Seebeck voltage.

With the equation above and the measured voltage presented in Figure 31, the structural Seebeck coefficient for each segment was estimated. The results are given in Table 3. The results indicate that structural Seebeck coefficient for the plane front regions are -0.055 mv/K and -0.05 mv/K for coarsened regions. For the cellular regions, the Seebeck coefficients vary from -0.03 mv/K to -0.01 mv/K depending on the solidification rate. The coarsened cells, which formed at V3, have the coefficient -0.03 mv/K, whereas the coefficient for the finest cells formed at V6 is -0.01 mv/K. The structural Seebeck voltage calculated based on the coefficients given in Table 3 are compared with the measured values in Figures 32-36. As can be seen, the results agree fairly well for the temperatures tested.

The structural Seebeck data was also used to calculate the kinetic undercooling for plane front solidification cycles at velocities V1, V2 and V3. These preliminary results, which are not included in this report, show that the undercooling increases with the solidification distance, goes through a maximum, and then declines until the growth stops. The maximum undercooling depends on the growth rate as well. The results are being further analyzed to incorporate the influence of the solute buildup on the undercooling.

6. Numerical Modelling

6.1 Introduction

In this section, a review is presented of the modelling work of the flight experiment performed by the Computational Fluid Dynamics Research Laboratory at The University of New South Wales, Sydney, Australia, in conjunction with the flight of MEPHISTO-4. Numerical simulations allow us to investigate the effects of natural convection on the interface shape, to predict planar (*i.e.*, non-dendritic) front instabilities and to calculate the segregation or redistribution of solute during solidification. The results of the calculations have been compared with those of the experiments for the purpose of better interpretation of the data, as well as the determination of the property values for bismuth.

For modelling transient phase change processes, a fixed-grid single domain approach (commonly called the enthalpy method) is widely accepted to be simpler and lower in computational cost than front tracking methods. In the present work the fixed-grid approach has been modified and employed for studying unidirectional plane front solidification of a Bi-1 at% Sn alloy in a Bridgman furnace. Thermal conductivity differences between the solid and liquid phases are included. The problem involves heat conduction in the solid alloy and in the walls of the ampoule containing the alloy; thermal and solutal convection; and diffusion in the liquid. Solute diffusion in the solid is neglected. The effects of concentration-dependent melting temperature on the phase change processes are incorporated.

Two numerical approaches are employed. In the first, the primitive variable equations are solved by a finite volume discretization, using a commercial flow code CFX 4.2 (CFX-4.2: Solver, Harwell Laboratory, 1997). In the second, a finite difference/finite volume discretization of the vorticity-stream function formulation of the equations is solved by an in-house code SOLCON (Timchenko *et al.*, 1998).

Validation of the codes has been obtained by a comparison of CFX calculations with an experiment in earth gravity using the material succinonitrile (de Groh and Lindstrom, 1994; Chen *et al.*, 1998) and by comparison of SOLCON with CFX.

A computational study of the transient directional solidification for Bi-1 at% Sn with different pulling velocities corresponding to events of the MEPHISTO-4 experiment was undertaken. Results were compared with analytical solutions and with actual microprobe and Seebeck signal results obtained from the MEPHISTO experiments.

6.2 Mathematical Formulation

The governing time-dependent equations describing momentum, heat and solute transport for laminar flow are

$$\nabla \cdot \tilde{\mathbf{V}} = 0 \quad (1)$$

$$\rho \left(\frac{\partial \tilde{\mathbf{V}}}{\partial t} + \tilde{\mathbf{V}} \cdot \nabla \tilde{\mathbf{V}} \right) = -\nabla P + \nabla \cdot \left\{ \mu \left[\nabla \tilde{\mathbf{V}} + (\nabla \tilde{\mathbf{V}})^T \right] \right\} + \tilde{\mathbf{B}} \quad (2)$$

$$\rho \left(\frac{\partial h}{\partial t} + \nabla \cdot (\tilde{V} h) \right) = \nabla \cdot (k \nabla T) \quad (3)$$

$$\frac{\partial C}{\partial t} + \nabla \cdot (\tilde{V} C) = \nabla \cdot (D \nabla C) \quad (4)$$

where ρ , μ , k , D are respectively the density, viscosity and thermal conductivity of the alloy and the diffusivity of the solute. P , h , T , \tilde{V} and C are respectively the pressure, enthalpy, temperature, velocity vector and solute concentration. \tilde{B} is a body force which, in the Boussinesq approximation, is

$$\tilde{B} = \rho_0 [-\beta_T(T - T_0) + \beta_C(C - C_0)]\tilde{g} \quad (5)$$

where ρ_0 , T_0 , C_0 and \tilde{g} denote respectively the reference density, temperature and concentration, and the acceleration due to gravity. β_C and β_T are the thermal and solutal expansion coefficients, defined by

$$\beta_T = -\frac{1}{\rho_r} \frac{\partial \rho}{\partial T} \quad \text{and} \quad \beta_C = \frac{1}{\rho_r} \frac{\partial \rho}{\partial C} \quad (6)$$

and assumed to be constant. We have made the major simplifying assumption that a two-dimensional model will be adequate, an assumption which will be justified by comparison between the calculations and experiments.

6.2.1 Heat Transfer with Phase Change-Latent heat evolution during phase change is incorporated in the energy equation through the use of an appropriate source term. For each phase ϕ , and for a constant specific heat, the enthalpy h is given by

$$h = C_{p\phi} T + f_\ell L = h_{sens} + f_\ell L \quad (7)$$

where L is the latent heat of fusion, $C_{p\phi}$ is the specific heat, h_{sens} is the sensible heat and f_ℓ is the local liquid volume fraction. For isothermal phase change, the liquid fraction is determined by the melting temperature T_m :

$$\begin{aligned} \text{for } T > T_m \quad f_\ell &= 1 \\ \text{for } T < T_m \quad f_\ell &= 0 \end{aligned} \quad (8)$$

Substituting (7) into the energy equation (3), we obtain

$$\rho C_{p\phi} \left(\frac{\partial T}{\partial t} + \nabla \cdot (\tilde{V} T) \right) = \nabla \cdot (k \nabla T) + S_T \quad (9)$$

where

$$S_T = -\frac{\partial}{\partial t} (\rho f_\ell L) \quad (10)$$

The source term (10) is used to account for latent heat release during phase change. For a partially solidified (i,j) cell, a weighted average control volume conductivity is calculated from

$$k_{i,j} = \frac{k_l k_s}{f_s k_l + f_l k_s} \quad (11)$$

where subscripts 's' and 'l' refer to the solid and liquid phases.

Equations (9) and (10) represent the fixed-grid approach for modelling heat transfer during a phase change. An essential part of this approach is the derivation of an enthalpy-temperature-liquid fraction relationship. In the case of unequal thermal conductivities in the solid and liquid phases the temperature gradient across a solidifying cell in the direction of solidification is not constant and the expression for liquid fraction derived by Timchenko *et al.* (2000) is no longer valid. To obtain a smooth history of the temperature and interface position and to account for the change in the temperature gradient while interface travels over the solidifying cell, the following weighting procedure for estimating liquid fraction in a partially solidified control volume is suggested (see Figure 37). The weighting in this scheme is necessary in order to avoid a discontinuity when the interface passes the grid point and to provide a smooth transition in the temperature gradient and hence in the rate of solidification.

First, the fictitious cell boundary temperature $T'_{i+1/2}$ and the liquid fraction based on a linear profile between $T_{i,j}$ and $T_{i-1,j}$ (the west or solid slope) are calculated:

$$T'_{i+1/2} = T_{i,j} + 0.5(T_{i,j} - T_{i-1,j}) \quad (12)$$

$$f_l|_w = \frac{T'_{i+1/2} - T_m}{T'_{i+1/2} - T_{i-1/2}} \quad (13)$$

Then, the fictitious cell boundary temperature $T'_{i-1/2}$ and the liquid fraction based on the linear profile between $T_{i,j}$ and $T_{i+1,j}$ (the east or liquid slope) are calculated:

$$T'_{i-1/2} = T_{i,j} - 0.5(T_{i+1,j} - T_{i,j}) \quad (14)$$

$$f_l|_e = \frac{T'_{i-1/2} - T_m}{T'_{i-1/2} - T_{i+1/2}} \quad (15)$$

Finally, a weighting based on the value of liquid fraction from the previous iteration is applied:

$$f_l^p = f_l^{p-1} f_l|_w + (1 - f_l^{p-1}) f_l|_e \quad (16)$$

where p is the iteration number. As in the case of equal thermal conductivities (and hence a constant temperature gradient in the direction of solidification) the cell starts to solidify when $T_{i-1/2,j} = T_m$ and $f_l|_w = 1$ and becomes completely solid when $T_{i+1/2,j} = T_m$ and $f_l|_e = 0$. In

between, while $T_{i-1/2,j} < T_m < T_{i+1/2,j}$, the liquid fraction of the partially solidified cell is calculated from the weighted averaging of the temperature gradients in the liquid and solid.

6.2.2 Solute Transport with Phase Change-The most difficult problem in modelling solute transport during solidification is associated with the discontinuity of solute concentration at the interface. Additional difficulties occur due to the presence of a thin solute boundary layer in the liquid in which large solute gradients, induced by the low partition coefficient, develop. Unlike front-tracking techniques with deforming grids in which the interface position is calculated explicitly and interface boundary conditions may be applied at the grid points, the enthalpy method avoids direct tracking of the interface. The position of the interface is not known *a priori* and has to be recovered from the temperature field. It can and generally does lie between, rather than at mesh points, and hence solutal and thermal boundary conditions cannot be applied directly at the interface. To satisfy mass balance and handle solute redistribution at the moving solidification front, a source term is introduced into (4).

The following assumptions are made:

1. thermodynamic equilibrium exists at the solid-liquid interface: $T_m = T_s = T_\ell$ and $C_s = k_p C_\ell$ where k_p is the partition coefficient;
2. solute diffusion in the solid phase is negligible;
3. the solid phase is stationary and a distinct separation of the phases exists at the interface;
4. the densities of the liquid and solid phases are constant and equal.

A source term accounting for the release of solute into the liquid during solidification can be derived by considering an average solute concentration in an arbitrary control volume which is undergoing phase change (Voller, Brent, and Prakash, 1989). This control volume can be treated as partially solidified with an average concentration

$$C = f_s C_s + f_\ell C_\ell \quad (17)$$

where $f_s = 1 - f_\ell$ is the local solid volume fraction. Since diffusion in the solid is neglected, the concentration in the solid at any point is constant with time, although it changes with position as new solid is formed at the solid-liquid interface. Noting that $C_s = k_p C_\ell$, we can thus derive

$$\frac{\partial C}{\partial t} = -\frac{\partial f_s}{\partial t} (1 - k_p) C_\ell + (1 - f_s) \frac{\partial C_\ell}{\partial t} \quad (18)$$

When (18) is used in the solute transport equation (4), we obtain the solute conservation equation in the form

$$\frac{\partial C_\ell}{\partial t} + \nabla \cdot (\tilde{V} C_\ell) = D \nabla^2 C_\ell + S_c \quad (19)$$

in which

$$S_c = \frac{\partial f_s}{\partial t} (1 - k_p) C_\ell + f_s \frac{\partial C_\ell}{\partial t} \quad (20)$$

During solidification, the melting temperature varies due to changes in solute concentration. With the assumption that phase change takes place under local thermodynamic equilibrium, the temperature at the interface, *i.e.*, the melting temperature T_m , can be expressed

$$T_m = T_{m0} + m_l C_I \quad (21)$$

where T_{m0} is the melting temperature of pure solvent (bismuth, in the case of MEPHISTO-4), m_l is slope of the liquidus, assumed to be constant and obtained from the phase diagram and C_I is the interface solute concentration in the liquid.

6.2.3 Extrapolation Scheme for Interface Concentration-In a fixed-grid formulation the computed values of C_I obtained from equation (19) are averaged values over the liquid portion of each partially solidified cell. As the interface moves from one cell to the next, this average value suddenly decreases because of the finite discretization involved. It then gradually increases as solidification proceeds due to solute rejection at the interface, which occurs (with Bi-Sn) at a rate faster than diffusion out of the control volume. It follows that the concentration-dependent melting temperature, if calculated from the average concentration, will have an incorrect zigzag shape and hence will not be suitable for the calculation of the local liquid fraction or for the estimation of interface position. To overcome this problem, it is necessary to calculate the concentration-dependent melting temperature based on the correct interface solute concentration extrapolated from the cell average values.

The concentration gradients near the interface induced by the low values of partition and diffusion coefficients are very steep. Hence the interface concentration cannot be obtained accurately by linear extrapolation from the average cell concentrations even assuming that the position of the interface has already been accurately predicted. Noting from one-dimensional theoretical considerations that the solute decay in front of the interface can be described by an exponential function, an extrapolation scheme based on a one-parameter approach (Timchenko *et al.*, 2000) has been suggested. The disadvantage of this scheme is that it requires a knowledge of the rate of solidification and hence the extrapolation procedure needs to be adjusted to account for different rates. A three-point extrapolation scheme was used in Chen *et al.* (1998). However that extrapolation procedure produced an interface concentration which did not satisfy the computed values when the interface passed through a cell boundary.

Here we present a new extrapolation scheme given by

$$C_I = C_{i,j} (1 + f_l \alpha) \quad (22)$$

The parameter α is determined from the maximum (last) value of $C_{i-1,j}$ which occurred before the cell $i-1$ became completely solidified, and the minimum (first) value of $C_{i,j}$ calculated when the interface moved into the cell i . Using the last value of $C_{i-1,j}$ from the cell $i-1$ ensures that C_I remains a monotonically increasing function when the interface goes from one computational cell to the next during solidification. At the first occurrence of the interface in cell i

$$C_I = (C_{i-1,j})_{last} = (C_{i,j})_{first} \{1 + (f_l)_{first} \alpha\} \quad (23)$$

where

$$\alpha = \left\{ (C_{i-1,j})_{last} - (C_{i,j})_{first} \right\} / \left\{ (f_l)_{first} (C_{i,j})_{first} \right\} \quad (24)$$

To account for the interface movement through the partially solidified control volume, the diffusion flux in the direction of solidification was discretized in the manner described by Timchenko *et al.* (2000).

6.2.4 Translation of Adiabatic Boundary Conditions-To be able to use the above extrapolation scheme for concentration we need to obtain a smooth decrease in the temperature of the partially solidified cell as the interface moves through the cell. This is very much determined by how the translation of the thermal boundary conditions on the outside of the ampoule is implemented. Translation of a ramp temperature profile leads to a smooth decrease of the cell temperature. However, translation of a boundary condition consisting of an adiabatic zone followed by an isothermal zone does not generate a smooth change in the boundary temperature. The boundary cell is treated as isothermal or adiabatic depending on where the junction between the cold isothermal zone and the adiabatic zone lies with respect to the grid point. When this junction passes a grid point, the generated change in boundary temperature turns out to be not smooth in time. To overcome this problem, a weighted boundary condition was used for the ampoule boundary cell containing this junction point. Until the junction point crosses the cell boundary, the cell is under an adiabatic boundary condition. The cell boundary temperature can be calculated in terms of the first two ampoule temperatures using a second order approximation that gives the zero wall heat flux. In the case of a uniform mesh with mesh size Δx this flux can be written as:

$$q_w = \frac{-3T_w + 4T_1 - T_2}{2\Delta x} = F(T_1, T_2) = 0 \quad (25)$$

When the junction point enters the cell, the boundary conditions of this cell are partially adiabatic and partially isothermal. To account for this, the following expression is used to calculate the nodal boundary temperature

$$T_w = F(T_1, T_2) * (1 - \xi) + T_c * \xi \quad (26)$$

where ξ is the distance from the left (solid side) cell boundary to the junction point expressed as a fraction of the mesh size. When ξ is zero, the cell is fully adiabatic; when it is unity, the cell is fully isothermal. The same approach is applied to the movement of the junction point between the adiabatic and hot isothermal zones.

The treatment of temperature at the boundary between the ampoule and the solidifying alloy required the implementation of a special numerical scheme in SOLCON. An additional equation for T_b was constructed by integrating the differential equation over the half control volume adjacent to the boundary. Perfect thermal contact at the alloy/ampoule interface is assumed, so that the conductive flux across the boundary is constant:

$$q_b = k_m \left. \frac{\partial T}{\partial n} \right|_m = k_a \left. \frac{\partial T}{\partial n} \right|_a \quad (27)$$

where subscript m denotes the alloy material in either liquid or solid phases, and a denotes the ampoule. The heat flux q_b written in terms of ampoule temperatures is used as the source term in the equation for the boundary temperatures. This allows the inclusion of alloy/ampoule boundary temperatures in the solution procedure for the solidifying sample temperatures. The ampoule outer boundary temperatures are calculated using equation (26) and used for the calculation of internal ampoule temperatures in the next iteration.

6.3 Solution Methods

Two different solution methods are used. One uses a finite volume, primitive variable formulation in the commercial code CFX; the other is a finite difference vorticity-stream function formulation implemented in an in-house code called SOLCON.¹ CFX is a general purpose code designed so that complex three-dimensional geometries may be readily handled. Although it can be used for two-dimensional problems (by selecting a mesh size of three in the ‘third’ direction), it tends to be more demanding in CPU time than a purpose-written 2-D code. SOLCON is available in 2-D and 3-D versions.

CFX-A sequential solution algorithm is used. In order to simulate the solid region in which the velocity is zero, a resistive force R is introduced into the momentum equation (2). R is set to zero in the liquid and is given a very large value in the solid (typically 10^6).

The set of transport equations (1), (2), (9) and (19) was discretized using a finite volume method. The SIMPLEC algorithm was used for pressure-velocity coupling with the Rhie-Chow interpolation method to prevent oscillations of pressure on the non-staggered grid. A fully implicit scheme was used for marching in time. Discretization of convection fluxes was performed using a hybrid scheme and the diffusion fluxes were discretized using central differences. The full field Stone’s method was used to solve the complete system of equations.

SOLCON-The time-dependent primitive variables equations were converted into the vorticity-stream function formulation in the conventional way. A modified Samarskii–Andreyev (ADI) scheme was used to solve iteratively the vorticity, stream function, energy and solute equations at each time step. The modification was designed to ensure accurate coupling between the solution of the transient equations and the thermal boundary conditions and to achieve true transient “simultaneous” solution of the equations. The coupling between equations and boundary conditions becomes especially important because of the movement of the temperature boundary profile. Moreover, the use of iterations becomes necessary because of the strong non-linearity of all governing equations. To ensure stability of the computational process, all source terms and non-linear coefficients depending on liquid fraction are linearized based on the value of the liquid fraction obtained from the previous iteration. In the solid, the vorticity, stream function and velocities are set to zero.

The vorticity, stream function and energy equations were discretized using central differences and solved by this modified ADI scheme. Interface boundary conditions for vorticity and stream function were applied at the mesh points in the solid sub-region nearest to the s/l interface. For the calculation of vorticity boundary conditions, the definition of vorticity was

¹SOLidification and CONvection

used: $\tilde{\zeta} = \nabla \times \tilde{V}$. The boundary condition $\tilde{\psi} = 0$ was used for the stream function. The concentration equation (19) was discretized using a control volume approach to ensure mass balance during phase change in the partially solidified control volume. A second order upwind scheme was used for the convection fluxes with central differences for the diffusion terms.

6.4 Model and Code Validations

The mathematical model and codes were validated by (a) a comparison of the two codes with each other and with the theory of Smith (Smith, Tiller, and Rutter, 1955) for the solidification of an alloy of bismuth with 1 at% tin in a microgravity environment of $10 \mu g$ and (b) a comparison with earth based succinonitrile solidification experiments performed at NASA Lewis Research Center (de Groh and Lindstrom, 1994; Yao and de Groh, 1993). The results of these comparisons have been published elsewhere, case(a) in Timchenko *et al.* (1998) and case (b) in Chen *et al.* (1998), and will only be summarised here.

Case (a): solidification of Bi-1at% Sn-Figure 38 shows the solute concentration distribution at the mid-height of the ampoule. The first 0.01 m of sample had been solidified in this time, creating a solute rich boundary layer in front of the interface. This decayed, nominally exponentially, to C_0 . The peak value of concentration at the interface caused by solute rejection into the liquid reached almost 11 at%. The results from SOLCON and CFX are almost identical. Maximum and minimum values of concentration at the interface are shown in Table 4.

Solute concentration in the solid at the mid-height of the ampoule is shown in Figure 39. An analytical solution for one-dimensional, diffusion-controlled plane front solidification (Smith, Tiller, and Rutter, 1955) is also shown since under microgravity conditions convection is very weak.

It can be seen from Figure 39 that the computed concentrations at the mid-height of the ampoule are close to the analytical, diffusion controlled value. The actual computed values of C_s at the mid-height of the ampoule are 0.328 at% (SOLCON) and 0.309 at% (CFX), whereas the analytical value is 0.335 at%. Of course the analytical solution is one-dimensional and convection, although weak, does produce radial segregation.

Case (b): earth based succinonitrile experiments-In this case comparison was made with earth based experiments of solidification, melting and no-growth (in which the imposed temperature conditions do not vary with time) of succinonitrile contained in a glass ampoule of square cross-section (6 mm inside dimension and 150 mm long) in a horizontal Bridgman furnace.

The interface shapes observed in various planes during the experiment were compared with the numerical calculations as shown in Figure 40. The agreement in almost every case was well within the expected experimental error of 0.5 mm (which is due mainly to the finite size - about 1 mm - of the thermocouples).

6.5 Preflight Modelling

6.5.1 Void Compensation-Bridgman type directional solidification experiments were done using the French built MEPHISTO furnace on all four of NASA's USMP missions. The second flight of the MEPHISTO furnace (MEPHISTO-2 [Abbaschian *et al.*, 1995, Abbaschian *et al.*, 1996]) suffered from a void in the liquid portion of the sample, even though a piston arrangement was in place to keep the ampoule filled. There were strict specifications from the French on the size (importantly, the diameter) of the Bi-Sn sample, so that it could be safely put into the fused silica ampoule. The cylindrical samples were approximately 900 mm long with a diameter of 5.8 mm. The fused silica ampoules were 6 mm internal diameter. Upon melting, the liquid needed to fill the whole 6 mm diameter ampoule; however, in addition to needing to fill the void present due to the difference between the ampoule and sample diameters, void space is also created during melting because the Bi sample contracts upon melting. The length compensator arrangement, shown in Figure 41, on the moving furnace side was designed to push additional sample into the hot zone until all void space was consumed. For MEPHISTO-2 there was not enough available movement in the compensator to fill the ampoule with liquid. As a result, a break in the liquid formed which resulted in an open circuit and the loss of the Seebeck signal. There was also about a 200 mbar argon pressure in the gap between the ampoule and sample. This added the possibility that the void in the liquid could contain argon gas - making elimination of it (the argon bubble) nearly impossible. For the fourth flight of the MEPHISTO furnace the initial diameter of the solid sample was increased to 5.88 mm; this decreased the volume compensation need upon melting to a value within the capabilities of the compensator.

During solidification, solid of 6 mm diameter is being formed. In order for the compensator to push the solid into the liquid it must overcome the friction forces between the 6 mm solid sample just solidified and the 6 mm ampoule. This creates the risk of the 6 mm solid sample getting stuck, immobilizing the compensator and allowing a void to form. To eliminate such a void, the liquid in the hot zones of the furnace can be heated, thereby expanding the liquid and consuming any void. The problem with this approach is that if the liquid is heated too much an overpressure could result, breaking the ampoule and ending the experiment catastrophically. An animated computer program (Johnston and de Groh, 2000; de Groh, Johnston, and Wei, 1998), called MEPHISTO Volume Visualizer (MVV), was written to help avoid the formation of unwanted voids and help with the assessment of the risks associated with the formation of a void and the additional heating of the liquid in the hot zone of this Bridgman type furnace; it is written in the Delphi 2 programming language and runs under Windows 95 and NT.

The calculations done by the MVV are based on a table containing a series of steps input by the user. Each step includes the position of the moving furnace, the temperatures of the moving and fixed furnaces and an optional step name. Hot and cold zones are assumed isothermal, and linear gradients are assumed in the insulated zones. The simulation progresses from step to step, calculating the position of any solid-liquid interfaces based on the alloy melting temperature, the position of the piston, and the magnitude of any void or overpressure. The program provides facilities to create and maintain the step table as well as run the simulation. The user can step through the simulation under manual control or allow the program to automatically step through it using a specified delay between steps. The results of the calculations are displayed graphically throughout the operation of the program and can also be printed.

During flight, MEPHISTO-2 ran nominally in the very early stages of the experiment, but as more of the sample was melted, a void formed in the liquid due to inadequate filling of the ampoule. MVV was run using the parameters used in the MEPHISTO Flight experiment during USMP-2 and accurately predicts this void: upon initial melting MVV shows no void and a compensator movement of 13.7 mm, which was within the capabilities of MEPHISTO-2, but just barely. The maximum movement of the compensator in MEPHISTO-2 was about 14 mm. After 10 mm of additional sample length melted, MVV shows a void forming and growing as more material is melted, in good agreement with what happened during MEPHISTO-2. In MEPHISTO-4 the virgin sample diameter was larger and compensator movement longer (20 mm); this prevented any void during processing. MVV correctly predicts this with the ampoule fully filled and compensator movement only about 6.7 mm with the sample fully melted.

6.5.2 Analysis of Rehomogenization Times-The analysis of a complete solidification/hold/melt cycle was undertaken. During the solidification stage, a solute-rich layer is formed immediately in front of the interface. The peak concentration decays by diffusion and weak convection during the hold stage; this continues during the subsequent melt stage. During the solidification stage, solute movement across the interface and solute buildup in the liquid must be correctly computed. A linear dependency of the melting temperature on the solute concentration based on the liquidus line of the Bi-Sn phase diagram was used. Thus interface movement will occur in the hold stages due to solidification or melting as the liquid solute concentration at the interface changes, as well as during the solidification stage itself. In the melting stages, solute movement across the solid/liquid interface was assumed to be zero.

The calculations are based on the following scenario, which is illustrated in Figure 42. As a result of previous furnace operations, the solid/liquid interface is initially located at a nominal position of 5 mm, and sufficient time is assumed to have elapsed to ensure that the liquid solute concentration is uniform. Thus the initial condition is that the solid and liquid each have a uniform concentration of $C_0 = 1$ at% Sn.

Furnace movement at a speed of V_1 for a distance of 5 mm then causes approximately 5 mm of solid² to be formed (and the associated solute boundary layer in the liquid is created). The apparatus is held stationary for 30 minutes, and that 5 mm is then melted, using a pulling velocity of $-V_1$. A second hold period of 30 minutes is imposed, following which an additional 5 mm is melted at a pulling velocity of $-V_2$, so that the interface has moved to a nominal position of 0 mm.

The question is: how long would now be required for the solute concentration in the liquid to return to being within $\pm 1/e$ of C_0 ?

In these calculations, $g = 1 \mu g$ and a single orientation of 45° to the ampoule axis (directed away from the solid) was employed. The solution domain was taken to be a two-dimensional ampoule which is 6 mm high by 30 mm long, and the calculations were performed for two sets of pulling velocities:

²It is not exactly 5 mm of solid because of the “drag” of the interface caused by the depression of the melting temperature as a result of variations in solute concentration.

- (i) $V_1 = 3.34 \mu\text{m/s}$, $V_2 = 6.6 \mu\text{m/s}$ and
- (ii) $V_1 = 1.85 \mu\text{m/s}$, $V_2 = 6.6 \mu\text{m/s}$.

At these pulling velocities, the durations of the solidification stage and the two melt stages are 24.95, 24.95 and 12.63 minutes respectively for (i), and 45.05, 45.05 and 12.63 minutes for (ii). Thus the two melt stages require a total of approximately 38 minutes for (i), and 58 minutes for (ii).

Figure 43(a) summarises the longitudinal concentration profiles at the mid-height of the ampoule for case (i) at various stages, and Figures 43(b) – (f) show the profiles in more detail at times indicated in the figure captions. The progressive decay of the non-uniformities in concentration can be seen. Figure 44 shows the transverse (“radial”) concentration profiles at the end of the second melt stage. It can be seen that some radial segregation exists, especially at about 1 cm from the interface. The maximum velocity at this stage is of the order of $0.2 \mu\text{m/s}$.

Figure 43(f) shows that $C_{max} = 1.22 \text{ at\% Sn}$ and $C_{min} = 0.67 \text{ at\% Sn}$ at this time, *i.e.*, before any additional hold occurs. In other words, the rehomogenization is complete, in the sense that C lies within $\pm(1/e)$ of C_0 , at the end of the V_2 melt, without the need for a further hold period. The reason is that the two 30 minute waiting periods within the cycle and the two melt stages provide sufficient time for rehomogenization to occur.

The results for case (ii), in which $V_1 = 1.85 \mu\text{m/s}$ and $V_2 = 6.6 \mu\text{m/s}$, are similar and need not be displayed in figures. Again, rehomogenization is complete at the end of the V_2 melt, without the need for a further hold period: $C_{max} = 1.18 \text{ at\% Sn}$ and $C_{min} = 0.69 \text{ at\% Sn}$.

Allowance was made for the change of the melting temperature due to a change of the interface solute concentration as a result of rehomogenization. These changes cause a small movement of the interface during the hold periods. In Figure 43(c) it can be seen that there has been a small forward movement (about 0.4 mm) of the interface compared with its position in Figure 43(b) as a result of the decay in the peak value of C and the consequent rise in T_m during the 30 minutes between these two figures. Similarly, a comparison of the results underlying Figures 7.6(d) and (e) shows that during the second 30 minute hold period, the interface has receded by a very small amount as a result of the increase in C and decrease in T_m at the interface.

6.5.3 Effects of g-jitter on Directional Solidification-We have investigated numerically the effects of sinusoidal disturbances (perpendicular to the longitudinal axis of the ingot) of the form

$$g(t) = g_0 + A \sin(2\pi\omega t) \quad (28)$$

on the solute redistribution and segregation at the interface during directional solidification of Bi-1at% Sn alloy. The amplitude, A , was varied from 10^{-5} g to 10^{-2} g and the frequency, ω , from 10^{-2} to 1 Hz, g_0 is the steady component of the acceleration and is taken to be $1 \mu\text{g}$ or 10^{-6} g . These results are summarized in Table 5.

Solidification at steady gravity was first computed for 1500 s; the resulting conditions were used as the initial conditions for the calculations with g-jitter, which continued for a further 500 s.

At a steady gravity level of 1 μg , segregation (defined as the difference between the maximum and minimum interface concentrations divided by the average interface concentration) was computed to be 1.8%.

With g-jitter, it was found that as the frequency is increased, a higher amplitude of the g-jitter is required to produce an effect on the segregation. For example, disturbances with frequencies of 0.5 or 1 Hz and amplitudes of 10^{-3} or less produce very little effect on the segregation. However for these same frequencies, an amplitude of 10^{-2}g results in segregation levels of 20.2% and 10.9% respectively. For lower frequencies, *e.g.* 0.05 Hz and 0.1 Hz, an amplitude of 10^{-3} g results in the maximum segregation changing to 11.3% and 8.9% respectively. The largest effect on the segregation is produced by disturbances with a frequency of 0.01 Hz, where the maximum segregation is equal to 4.9% for an amplitude of 10^{-4} g, 38.2% for an amplitude of 10^{-3} g and 188.7% for an amplitude of 10^{-2}g . It is of interest to note that, at the lowest frequencies, the value of segregation might actually reach a maximum before 500 s, and that by 500 s, it had decayed somewhat. This is most noticeable at 0.01 Hz and 10^{-2} μg .

Figure 45 shows the effect of g-jitter on the average concentration at the interface for an amplitude of 10^{-2} g and a range of frequencies.

6.5.4 Radial Segregation-Our numerical results show a strong dependence of radial segregation on interface curvature. Computations have been done for solidification with a pulling velocity of 3.34 $\mu\text{m/s}$, a steady gravity of 10 μg and including the effects of unequal thermal conductivities of the solid and liquid. When conduction through the wall was not included, the interface deflection from the flat was about 26% after 1000 s of solidification with a corresponding segregation of 22%. Including the wall decreased the deflection to 11% and the radial segregation to 10%. Kaddeche *et al.* (1996) suggest that segregation as function of deflection is given by

$$\gamma = 0.8 * Pe * (1 - k_p) * \eta \quad (29)$$

where γ is the segregation of the solute at the interface, η is the deflection of the interface and Pe is the Peclet number. This formula is valid for small curvature (deflection).

To check our results, computations were performed with physical parameters taken from Kaddeche *et al.* (1996); our results showed good agreement with theirs. It is concluded that computations made without taking into account the ampoule wall introduce an unrealistic curvature and as a consequence unrealistic segregation. This is particularly important in the case of concentration-dependent melting temperature in which the increased concentration in the centre of the interface will decrease the speed of solidification and hence cause the interface curvature to increase further. As the interface deflection strongly depends on the temperature, implementation of the proper temperature boundary conditions will determine the accuracy of the calculated radial segregation.

6.6. Flight Experiment Modelling and Comparisons

6.6.1 MEPHISTO Events

Events 11E, 11F

The model has been applied to the simulation of the experiments performed during the 1997 flight of MEPHISTO-4. Typically, a simulation - like an event of the actual experiment - would be started after the solid/liquid interface had reached a certain position and been held there for sufficient time for the liquid in front of the interface to have returned to a more or less uniform concentration at the initial value of 1 at%. In the example described below (the events identified in the flight schedule as 11E and 11F), solidification at a pulling speed (the speed of the moving furnace) of $3.34 \mu\text{m/s}$ occurred for 0.333 h. The furnace was then stopped for 3.7 h (an “extended hold”) during which time almost complete rehomogenization of the liquid occurred. Solidification at a speed of $1.85 \mu\text{m/s}$ followed for 0.6 h.

The melting temperature was calculated according to (21) with $m = -2.32 \text{ K/at\%}$. The magnitude of the gravity vector was taken to be $1 \mu\text{g}$, *i.e.*, $9.81 \times 10^{-6} \text{ m s}^{-2}$, acting in a direction normal to the axis of the ampoule. The thermal conductivity of the liquid and solid phases were $k_l = 12.4 \text{ W/m K}$ and $k_s = 6.5 \text{ W/m K}$ respectively. Properties value for pure liquid bismuth (Timchenko *et al.*, 1998) taken at the reference temperature of 271.3° C (the equilibrium melting temperature of Bi) were used. The partition coefficient k_p for Sn in Bi was set at 0.029.

Agreement in the literature has not been found among various measured values of the diffusion coefficient D for dilute Sn in Bi near 271.3° C . Values vary from $1.76 \times 10^{-9} \text{ m}^2/\text{s}$ (Buell and Shuck, 1970) to $2.7 \times 10^{-9} \text{ m}^2/\text{s}$ (Niwa *et al.*, 1957). In these calculations $D = 2.0 \times 10^{-9} \text{ m}^2/\text{s}$ was chosen after a comparison of numerical solutions with post-flight microprobe results for solute concentration in the solid. The model included a 2 mm wall with thermal conductivity of 2.1 W/m K .

The moving thermal conditions imposed on the outer walls of the ampoule consisted of a cold zone ($T_c = 50^\circ \text{ C}$), an adiabatic zone and a hot zone ($T_h = 700^\circ \text{ C}$). These conditions were translated along the boundary with a speed corresponding to a particular event. The length of the adiabatic zone was 20 mm, leading to an internal temperature gradient in the liquid of approximately 20 K/mm , corresponding to the experimentally measured value.

The computed distribution of solute concentration in the solid *along the centre line* of the sample is shown in Figure 46(a). Numerical solutions are presented together with the microprobe results obtained after the flight from the experimental samples. Figure 46(b) shows the distribution of solute concentration *across* the solid. Both axial and transverse numerical distributions are in very good agreement with the experimental results. Other results such as temperature contours, velocity vectors, solute buildup during solidification, and solute decay during the hold, are shown in Figures 46(c) – (e). Figure 46(f) shows the progressive solute buildup inside and outside the capillary (for a different event). As shown in Figure 46(g), the predicted interface shape is in excellent agreement with that observed in the actual experiment.

Due to limitations imposed by the size of the thermocouples used to measure temperature, some discrepancy exists between computed and measured values. Figure 47(a) shows the computed temperature distribution along the centreline of the sample together with the in-flight measurements obtained using a thermocouple located in the sample. Figure 47(a) contains measurement data obtained from all events; finer details of the temperature distribution in the vicinity of the interface taken from one event are shown in Figure 47(b). The change in the computed temperature gradient is caused by the change in thermal conductivity between the solid and liquid phases. The measurements do not exhibit this sharp change in the gradient due to the averaging effect produced by the finite size of the thermocouple.

Event 9W

We present here calculations for event, 9W, performed at a time when the solid/liquid interface was located inside the capillary. A solution domain 2 mm high (internal diameter of the capillary) and 30 mm long was used. The value of gravity was $1 \mu g$, and a 10×200 mesh was used (uniform 0.2 mm across the ampoule; 100×0.1 mm followed by 100×0.2 mm along the ampoule). At such a low value of g , the velocities are extremely small, and although a finer mesh was tested, it was not needed for the production runs.

As shown in Figure 48, the simulation started after the solid/liquid interface had reached a certain position and had remained there for sufficient time for the liquid in front of the interface to become homogeneous (Chen *et al.*, 1998). Solidification at a pulling speed of $5.185 \mu m/s$ then occurred for 965 s (from A to B, Figure 48). The furnace was stopped for 1800 s (B to C), during which time partial rehomogenization of the liquid occurred. Melting at the same speed followed for 965 s (C to D), and then a further rehomogenization stage (D to E) for another 1800 s. The melting temperature was calculated according to equation (21) with $T_{m0} = 271.3^\circ C$ and $m = -2.32 K/at\%$. The interpolation scheme of Chen *et al.* (1998) was used.

The distributions of solute concentration along the central line at the end of each stage of the process (*i.e.*, at B, C, D and E) are shown in Figure 49. The peak solute concentration at the end of solidification is about 8 at%. The solute distribution in the liquid becomes increasingly homogeneous during the subsequent stages of the process. Note the shift in the position of the interface between stages B and C, and the accompanying drop in C_s . This is due to the additional solidification following the decay in interface C_ℓ by diffusion and the consequent rise in melting temperature T_m : the temperature in the thin layer of liquid in front of the interface is thereby lower than the new T_m and this layer therefore freezes.

The history of the solute buildup and decay on the liquid side of the interface is shown in Figure 50, as well as the corresponding melting temperature. C_ℓ rises during solidification (A-B), and decays due to diffusion during the rehomogenization stage B-C.

When melting begins (at C), the interface concentration drops to a value (C') which reflects the additional solidification described above. After this thin layer of solid has melted ($C'-C''$), the liquid is then exposed to solid which had formed during A-B and which has a solute concentration which gradually diminishes as it melts ($C''-D$).

The interface solute concentration again rises due to diffusion during the final rehomogenization (D-E). The variation in C_l has a significant effect on T_m . From the large range of values of melting temperature which results, it is clear that the effect of concentration on T_m cannot be ignored. The velocities at the low value of g and in the smaller diameter capillary are much lower – of the order of 0.01 $\mu\text{m/s}$.

Nevertheless, the flow pattern is of interest. Figure 51 shows the velocity vectors at three stages of the process: (a) early in the solidification; (b) at the end of solidification; and (c) part way through the first rehomogenization stage. In Figure 51(a) a thermally driven counter clockwise circulation can be seen, the result of which is a slight variation in interface solute concentration, of the order of about 1/2% across the ampoule. In Figure 51(b) there is a reverse, solute-driven clockwise cell which has formed in front of the interface due to the lower density accompanying the higher concentration. Finally, in Figure 51(c), the reverse cell has almost disappeared as the concentration peak decays and the liquid becomes more homogeneous. The interface movement during rehomogenization can again be seen.

6.6.2 Seebeck Signal-The Seebeck technique was used in MEPHISTO-4 in an attempt to determine undercooling and concentration buildup at the solidification front. The thermoelectric voltage exists because the solid and liquid have different Seebeck coefficients and the temperature field is not uniform.

For a given temperature field, the thermoelectric voltage due to a Seebeck coefficient, η , is given by (Rouzaud, Favier, and Thevenard, 1988)

$$E = \int \eta \, dT \quad (30)$$

In MEPHISTO, a thermal gradient field exists at both ends of the ampoule; one is moving and the other is stationary. At the start of an experiment, both ends are at the same interface temperature, T_{ref} . As solidification occurs, the interface position at the moving end changes and the temperature at the position initially occupied by the interface will now have a different value, T_β , say (see Figure 52). From equation (30), it can be shown that the voltage between the ends will change by:

$$\Delta E = \int_{T_\beta}^{T_l} (\eta_s - \eta_e) \, dT + \int_{T_l}^{T_{ref}} (\eta_e - \eta_l) \, dT = \Delta E_{struct} + \Delta E_{const} \quad (31)$$

where the subscripts s , e , and l refer respectively to the newly or space grown solid, the material present at the start, which, in the cases chosen, was earth grown, and the liquid. The first term on the right hand side of equation (31) may be interpreted as the structural contribution and the second term as the constitutional contribution to the Seebeck signal due to the difference between T_{ref} and T_l . If the observed Seebeck signal is different to that predicted by equation (31), the differences must be due to other sources of undercooling such as curvature or kinetic effects.

The foregoing discussion is only applicable to a one-dimensional analysis. For MEPHISTO, we have treated all the field variables as two-dimensional. In particular, the solute concentration varies across the interface as well as along the ampoule, producing radial segregation. However, the measured Seebeck signal is some kind of average value, which cannot distinguish local variations across the ampoule. Therefore, to take into account two-dimensional effects, the average concentration across the interface has been used. The temperature field for the calculation of the structural Seebeck voltage has been taken directly from the numerical solutions. It was found that the temperature *gradient* in the gradient zone is approximately independent of the actual interface temperatures and of the solidification time and speeds. The temperature changes from the interface value were represented by a second order polynomial in the distance from the interface. To account for the radial variation in the thermal field, polynomials were computed for a range of radial position and averaged to yield

$$T(d) = T_I 3 - 2.3d + 1.46d^2 \quad (32)$$

where d is the distance in mm measured from the interface (see Figure 52).

The principles outlined above were applied to a number of events at pulling velocities of 1.85 $\mu\text{m/s}$ (V1) and 3.33 $\mu\text{m/s}$ (V2). All the chosen events involved a nominal solidification distance of 5 mm followed by a holding period of 1800 s. Event 11R(V1) was chosen to determine the Seebeck coefficients that would give the best fit to the measured Seebeck signals based on equation (27), using a temperature field numerically determined as described above. The following set of parameter values thus developed:

$$\begin{aligned} \text{Seebeck coefficient for liquid} &= -0.005 \text{ mV/K} \\ \text{Seebeck coefficient for earth grown solid} &= 0.02 \text{ mV/K} \\ \text{Seebeck coefficient for space grown solid: } \eta_s &= .0297 + .0069(C_I - C_{ref}) - .0017(C_I - C_{ref})^2 \quad (33) \end{aligned}$$

where C_{ref} is the concentration at T_{ref} . The Seebeck coefficient for space grown solid was found following numerical procedures reported previously (Chen *et al.* 2000). However, previously only a modified Seebeck coefficient $\eta_s^* = \eta_s \partial T / \partial C_I$ was used. Since both the temperature and concentration in the gradient zone were known, they were used to obtain equation (33) from η_s^* .

Figure 53(a) shows computed Seebeck voltages for a pulling velocity of V1 compared with measured signals for three V1 events: 9A, 9G and 11R. The excellent agreement with 11R follows the fact that this event was used to calculate the above Seebeck coefficient. The agreement with 9G is also excellent. However, the character of the measured signal for 9A is quite different from the other two, due possibly to unidentified effects of prior events, because Seebeck signals are sensitive to how the solid material had been formed. Figure 53(b) shows comparisons between computations, using the same Seebeck coefficient computed from equation (33), and measurements for several V2 events; the agreement with 9H is good, that with 9B is fair and that with 11Q1 is poor.

In Figures 53(c) and (d), equation (31) has been used to determine the structural and constitutional components of the Seebeck signals. When these components are subtracted from the measured signal, the difference is the Seebeck signal due to other causes, most notably

kinetic effects. It can be seen that the Seebeck signals during solidification display various degree of 'plateau' characteristics depending on the pulling speed. This characteristic is more pronounced with higher pulling speeds. This is due to the nature of the structural component that represents the interactive effect between the thermal gradient field and the changing grain structure of the material within this field. As the interface concentration increases, a partial break down of the planar front into cellular structure would have taken place. Such a change would result in a decrease of the Seebeck coefficient and hence the Seebeck signals. In fact, the second term on the right hand side of equation (33) accounts for the increases of Seebeck coefficient due to increased concentration for a dilute tin-bismuth alloy. The third term on the other hand represents microstructure changes. However, for a tin-bismuth system, changes in microstructure have not been observed to take place uniformly and predictably, as grains of a particular type might continue long after surrounding grains had changed to another type. This unpredictable nature could be used to explain most of the differences in the Seebeck signals shown in Figures 53(a) and (b). There could be other factors as well such as g-jitter or the movement of a length compensator (incorporated to allow for volume change on melting of the initially solid alloy). Generally, during the initial period of a solidification run when a uniform grain structure was expected, there was good agreement between the numerical predictions and the experimental measurements.

At the end of a hold following solidification, the interface concentration returns to, or close to, the value at the beginning of solidification. However, the interface position is different and any Seebeck voltage changes must be "structural" according to equation (31). The fact that this structural signal was observed to be different for different events implies that each event has a different structural Seebeck coefficient. Notwithstanding the limitation associated with the structural Seebeck coefficient, it was observed that, during holding, the recorded changes in Seebeck voltage from the start to the end were largely consistent with each other, including all V1 and V2 events. Figures 53(c) and (d) show that during holding these changes were mostly due to changes in the constitutional components. It can be concluded that if the diffusion coefficient is known, the Seebeck signals during holding can be used to find the Seebeck coefficient as employed by us here. On the other hand if the Seebeck coefficient is known from other measurements, the Seebeck signals observed could be used to validate the diffusion coefficient that is responsible for the concentration changes.

Figures 53(c) and (d) show also the kinetic components of undercooling. These were included to show that the kinetic components can be obtained by subtracting both constitutional and structural components from the observed total signals. Because of the problem with the structural Seebeck coefficient, it has to be conceded that this approach cannot be very accurate. However, as an indication of magnitude, it seems that the kinetic component, if any, and together with any other sources of undercooling, would only represent a few degrees.

7. Conclusions and Discussion of Significant Findings

The furnace hardware operated without problems during the USMP-4 flight. The loss of the Seebeck signal that plagued MEPHISTO-2 was solved by modeling the sample volume and length compensator movement, increasing the starting diameter of the ingot, and carefully melting the sample from the center out. A total length of 450 mm of the alloy was directionally

solidified under diffusion-dominated conditions. At the end of the mission a small length of sample was effectively quenched by rapidly drawing it into the chill; in this ingot the resistance change across the sample during processing was monitored and by all accounts, gave an accurate determination of the rate of solidification. Current was pulsed through the Peltier sample in an effort to mark the interface. However, upon post-flight analysis and etching, no marks characteristic of Peltier demarcation were achieved. Interface shapes were found through analysis of the planar to cellular transition and the Quenched sample. During flight all operations associated with the Seebeck sample were nominal. However, analysis of the Seebeck signal has not, as yet, yielded a measurement of the interface temperature that we consider reliable.

Using a temperature gradient of 204 K/cm in the liquid, growth at less than or equal to 3.4 $\mu\text{m/s}$ resulted in planar growth, and growth at greater than or equal to 6.7 $\mu\text{m/s}$ resulted in cellular growth. The plane front interfaces were flat with a very slight concavity as viewed from the liquid. The radial composition measurements showed no significant radial segregation, thus giving an indication of diffusion dominated growth. Due to the excellent agreement between the numerical modeling and validation cases and the composition measurements taken from the space grown samples, modeling results are concluded to be accurate. The maximum convective flow parallel to the interface in the 6 mm section of the ampoule was determined to be 0.12 $\mu\text{m/s}$; thus the solutal Peclet number ($2 \times \text{flow rate/growth rate}$) during MEPHISTO-4 was less than 1 ($Pe_s = 0.13$) – showing the growth to be diffusion dominated.

The use of the Seebeck signal to determine the interface temperature was initially believed to be straightforward. However, after our first flight (MEPHISTO-2) we were concerned about the influence of grain boundaries on the signal. To solve this we incorporated the 2 mm internal diameter capillary so that a single crystal could be formed and thus eliminate any corruption of the Seebeck signal. The sensitivity of the Seebeck signal to the structure of the sample and the thermal gradient is much greater than we expected. We are presently examining this and continuing our analysis of the kinetics data.

8. Success Assessment

Three categories of success were defined and detailed in the May 1996 Project Development Plan, and presented to NASA management and the peer review panel prior to the final approval to proceed to flight. These success criteria are repeated below and the flight experiment and its results judged item by item relative to the defined criteria.

Exceeds Expectation

- E1. Full 150 mm "test length" fully solidified in all three samples.
- E2. All scheduled Seebeck measurements completed.
- E3. All scheduled Peltier pulses completed.
- E4. Sample successfully quenched.
- E5. No thermocouple failures.
- E6. No ampoule overpressure upon final solidification (i.e., no broken ampoules).

Highly Successful

- H1. One complete set of temperature histories from both the thermocouples during solidification.
- H2. No damage to the furnace due to overpressure upon solidification.
- H3. Peltier pulses completed at two solidification velocities.
- H4. Seebeck measurements within and outside the growth capillaries.
- H5. At least 2 cm solidified both inside and outside the growth capillaries.

Successful

- S1. One complete temperature history from either thermocouple during solidification.
- S2. Some interface demarcation induced.
- S3. Seebeck measurements at three growth velocities inside the growth capillary.
- S4. At least 2 cm solidified.

Of the above success criteria, E1, E4, E5, E6, H1, H2, H5, S1, S2, and S4 were all completely met and accomplished in MEPHISTO-4. All of the "Exceeds Expectation" criteria were met except E2 and E3; E2 and E3 were partially met and accomplished successfully. Regarding E2, all Seebeck measurements were in fact made, and many in addition to those originally scheduled; however, this is tempered by the complexity of the Seebeck results and the lack of a resulting conclusive interface temperature measurement. Regarding E3, all Peltier pulses were made successfully during flight, however, no resulting mark on the sample could be drawn from the ingots; interface shapes were determined from the planar to cellular transitions and the quenched interface. The shortcomings associated with E2 and E3 also apply to H3, H4, and S3.

Appendix A

List of Publications for MEPHISTO-2 and -4

MEPHISTO-2, on USMP-2, Publications:

- 1) "A Numerical and Experimental Study of Natural Convection and Interface Shape in Crystal Growth," by G.H. Yeoh, G. de Vahl Davis, E. Leonardi, H.C. de Groh III, and M. Yao, in proceeding of the First International Conference on Transport Phenomena in Processing, S.I. Güçeri, editor, 1993, pp. 98–109.
- 2) "Application of the Segregated Solution Approach in 3-D FEM Modeling of Crystal Growth," by M. Yao and H.C. de Groh III, *Advances in Finite Element Analysis in Fluid Dynamics*, edited by M.N. Dhaubhadel, M.S. Engelman, and J.N. Reddy, FED.-Vol.137, 1992, pp. 53–60.
- 3) "Segregated Solution in 3-D Modeling of Crystal Growth," by M. Yao and H.C. de Groh III, LEW-15672, NASA Tech Brief, Vol. 17, No. 11, 1993.
- 4) "Three-Dimensional Finite Element Method Simulation of Bridgman Crystal Growth and Comparison with Experiments," by M. Yao and H.C. de Groh III, *Numerical Heat Transfer, Part A*, Vol. 24, 1993, pp. 393–412.
- 5) "Interface Shape and Convection during Melting and Solidification of Succinonitrile," by H.C. de Groh III and Tiffany Lindstrom, NASA TM–107724, 1994.
- 6) "Numerical and Experimental Study of Transport Phenomena in Directional Solidification of Succinonitrile," by H.C. de Groh III and M. Yao, in *Transport Phenomena in Solidification*, edited by C. Beckermann et al., HTD-Vol. 284, AMD-Vol. 182, 1994 ASME, pp. 227–243.
- 7) "On Residual Acceleration During Space Experiments," by H.C. de Groh III and E.S. Nelson, in *Heat Transfer in Micro-g Systems*, edited by S.S. Sadhal and A. Gopinath, HTD-Vol. 290, ASME 1994, pp. 23–33.
- 8) "The Effect of Gravity on Natural Convection and Crystal Growth," by G. de Vahl Davis and H.C. de Groh III, *Microgravity Materials Science Conference*, Huntsville, Alabama, May, 1994.
- 9) "In Situ Monitoring of Crystal Growth Using MEPHISTO," by R. Abbaschian, A.B. Gokhale, R. DeWitt, G. Cambon, J.J Favier, S.R. Coriell and H.C. de Groh III, *Microgravity Materials Science Conference*, Huntsville, Alabama, May, 1994.
- 10) "Convection and Solidification with Applications to Crystal Growth," by G. de Vahl Davis, *Rep. Inst. Adv. Mat. Study*, Vol. 8, No. 1, pp. 53–59, 1994.
- 11) "Kinetic Self-Stabilization of a Stepped Interface: Binary Alloy Solidification," by S.R. Coriell, B. T. Murray, and A. A. Chernov, *J. Crystal Growth* 141, pp. 219–233, 1994.
- 12) "A Study of Directional Solidification of Faceted Bi-Sn Alloys in Microgravity," by R. Abbaschian, A.B. Gokhale, J.J. Favier, G. Cambon, S.R. Coriell, H.C. de Groh III and R.L. DeWitt, invited paper for the 33rd AIAA Aerospace Sciences Meeting, Reno, Jan. 1995, AIAA 95–0608.

- 13) "Numerical Modeling of Bridgman Growth in Space with MEPHISTO," by M. Yao, R. Raman and H.C. de Groh III, Computational Mechanics '95, Theory and Applications, Vol. 1, 1995, proceedings of Int. Conf. on Computational Eng. Sci., edited by S.N. Atluri, G. Yagawa, and T.A. Cruse, pp. 514–519.
- 14) "Numerical Simulation of Heat and Mass Transport during Space Crystal Growth with MEPHISTO," by M. Yao, R. Raman, and H.C. de Groh III, 1995, NASA TM–107015.
- 15) "Effects of Shear Flow and Anisotropic Kinetics on the Morphological Stability of a Binary Alloy," by S.R. Coriell, B.T. Murray, A.A. Chernov, and G.B. McFadden, Metallurgical and Materials Trans. 27A, pp. 687–694 (1996).
- 16) "A Study of Directional Solidification of Faceted Bi-Sn Alloys in Microgravity," by R. Abbaschian, A.B. Gokhale, D.B. Allen, and S.R. Coriell in Solidification Science and Processing, edited by I. Ohnaka and D.M. Stefanescu (The Minerals, Metals & Materials Society, Warrendale, PA, 1996) pp. 73–84.

MEPHISTO-4, on USMP-4, Publications

- 17) "Numerical Modeling of Solidification in Space with MEPHISTO-4 (Part 1)," by Minwu Yao, H.C. de Groh III, and R. Abbaschian, AIAA 35th Aerospace Sci. Meeting, Jan. 1997, AIAA 97–0449.
- 18) "A Numerical and Experimental Study of Natural Convection and Interface Shape in Crystal Growth," by G.H. Yeoh, G. de Vahl Davis, E. Leonardi, H.C. de Groh III and M. Yao, J. of Crystal Growth, Vol. 173, No. 3–4, 1997, pp. 492–502.
- 19) "Numerical Modeling of Solidification in Space with MEPHISTO-4 (Part 2)," by James E. Simpson, Minwu Yao, Henry C. de Groh III, and Suresh V. Garimella, NASA/TM—1998-206630, Feb. 1998.
- 20) "Rehomogenization: Diffusion and Convection in Microgravity," by V. Timchenko, G. de Vahl Davis, P. Chen, H.C. de Groh III, J. Keanton, E. Leonardi, S.S. Leong and R. Abbaschian, AIAA 98-0740, 36th Aerospace Sci. Meeting, Jan. 1998.
- 21) "Melt Convection Effects in the Bridgman Crystal Growth of an Alloy under Microgravity Conditions," by J.E. Simpson, S.V. Garimella, H.C. de Groh III and R. Abbaschian, AIAA/ASME Jt. Thermophys. and Heat Transfer Conf., ASME HTD-Vol. 357–4, pp. 123–132, 1998.
- 22) "A Numerical Study of Directional Solidification and Melting in Microgravity," by P.Y.P. Chen, V. Timchenko, E. Leonardi, G. de Vahl Davis, and H.C. de Groh III, Proc ASME, HTD-Vol. 361–3, edited by R.A. Nelson, L.W. Swanson, M.V.A. Bianchi and C. Camci, pp. 75–83, Nov. 1998.
- 23) "Directional Solidification in Microgravity," by V. Timchenko, P.Y.P. Chen, G. de Vahl Davis, and E. Leonardi, Proceedings of 11th IHTC, Vol. 7, Aug. 1998, Kyongju, Korea, pp. 515–520.

- 24) “MEPHISTO/USMP-4/STS-87, In-situ Monitoring of Crystal Growth Using MEPHISTO, Preliminary flight results,” by G. Cambon, G. Hieu, R. Abbaschian, K. Beatty, H. de Groh, N. Kernevez, E. Rolland, V. Gounot, Ph. Beaugrand, IAF/IAA-98-J.3.04, 49th International Astronautical Congress, Melbourne, Australia, Sept. 28 1998.
- 25) “Directional Solidification of Bi-Sn Alloys,” by R. Abbaschian, K.M. Beatty, F. Chen, T. Lenzi, H. de Groh III, G. Cambon, G. de Vahl Davis, E. Leonardi, Proceedings of 10th International Symposium on Experimental Methods for Microgravity Materials Science, San Antonio, Texas. Published on CD-Rom, ISBN-87339-432-11, 1998.
- 26) “Directional Solidification of Bi-Sn Alloys,” by Reza Abbaschian, Kirk M. Beatty, Fuwang Chen, Tyler Lerzi, Henry C. de Groh III, Gerard Cambon, Graham de Vahl Davis and Eddie Leonardi, TMS, 10th International Symposium on Experimental Methods for Microgravity Materials Science (EMMMS), Feb. 1998.
- 27) “Void Management in MEPHISTO and Other Space Experiments,” by Henry C. de Groh III, J. Christopher Johnston, and Bingbo Wei, Joint 1st Pan-Pacific Basin Workshop and 4th Japan-China Workshop on Microgravity Sci. Proc., J. Jpn. Soc. Microgravity Appl. Vol. 15, Supplement II, 1998, pp. 46–50.
- 28) “Efficient numerical calculation of unsteady free convection,” by G. de Vahl Davis, E. Leonardi, V. Timchenko and M. Wolfshtein, Advances in Computational Heat Transfer, edited by G. de Vahl Davis and E. Leonardi, Begell House Inc., New York, pp. 216–223, 1998.
- 29) “Heat and Mass Transfer with segregation in directional solidification,” by V. Timchenko, M. EL Ganaoui, A. Lamazouade, D. Morvan, E. Leonardi, P. Bontoux and G. de Vahl Davis, Advances in Computational Heat Transfer, edited by G. de Vahl Davis and E. Leonardi, Begell House Inc., New York, pp. 508–515, 1998.
- 30) “Directional solidification in microgravity,” by V. Timchenko, P.Y.P. Chen, G. de Vahl Davis and E. Leonardi, Heat Transfer 1998, edited by J.S. Lee, Taylor & Francis, pp. 241–246, 1998.
- 31) “Crystal Growth by the Bridgman Process in Microgravity,” by G. de Vahl Davis, in Advanced Computational Methods in Heat Transfer V, edited by A.J. Nowak, C.A. Brebbia, R. Bialecki and M. Zerroukat, Computational Mechanics Publications, Southampton 1998, pp. 567–581.
- 32) “An Experimental and Computational Study of Directional Solidification in Transparent Materials,” by James E. Simpson, Henry C. de Groh III, and Suresh V. Garimella, invited paper to Symp. on Fluid Flow Phenom. In Metals Processing, 1999 TMS Annual Meeting, Feb., 1999, Fluid Flow Phen. in Metals Proc., edited by N. El-Kaddah, D.G.C. Robertson, S.T. Johansen, and V.R. Voller, TMS Pub., 1999.
- 33) “Directional Solidification of Pure Succinonitrile and a Succinonitrile–Acetone Alloy” by J.E. Simpson, H.C. de Groh III and S.V. Grimella, NASA/TM-1999–209381, Aug. 1999.

- 34) "Effect of G-Jitter on Directional Solidification of a Binary Alloy," by C. Benjapiyaporn, V. Timchenko, G. de Vahl Davis, and E. Leonardi, 49th Internat. Astronautical Congress, IAF-98-J.2.01, also printed as a NASA/TM-1999-209281.
- 35) "Effects of Space Environment on Flow and Concentration during Directional Solidification," by C. Benjapiyaporn, V. Timchenko, G. de Vahl Davis, E. Leonardi, and H.C. de Groh III, NASA/TM-1999-209293.
- 36) "Numerical Simulations of Crystal Growth of an Alloy Under Microgravity Conditions," by J.E. Simpson, S.V. Garimella, H.C. de Groh III, and R. Abbaschian, 33rd Nat. Heat Transfer Conf. Aug. 1999, HTD99-204, ASME.
- 37) "Directional Solidification of Bi-Sn on USMP-4," by R. Abbaschian, H.C. de Groh III, E. Leonardi, and G. de Vahl Davis. Pub. by Trans. Tech. Pub., in the proceedings of the Third Int. Conf. on Solidification and Gravity, April 1999.
- 38) "Solidification and Melting in Microgravity," by E. Leonardi, PCC99: International Workshop on Phase Change with Convection, edited by T.A. Kowalewski, F. Stella, J. Banaszek and J. Szmyd, Polish Academy of Sciences, Warsaw, Poland, Vol. 5/1999, pp. 19-26, 1999. [Invited Keynote lecture].
- 39) "Effect of Thermal Conductivities on Heat and Mass Transfer During Directional Solidification," by V. Timchenko, M. El Ganaoui, E. Leonardi, P. Bontoux and G. de Vahl Davis, PCC99: International Workshop on Phase Change with Convection, edited by T.A. Kowalewski, F. Stella, J. Banaszek, and J. Szmyd, Polish Academy of Sciences, Warsaw, Poland, Vol. 5/1999, pp. 151-154, 1999
- 40) "Morphological Stability of Bismuth-Tin Alloys," by R. Abbaschian, S. Coriell, and A. Chernov, in Solidification 1999, edited by S.P. Marsh, N.B. Singh, P.W. Voorhees, and W.H. Hofmeister (The Minerals, Metals & Materials Society, Warrendale, PA, 1999) pp. 219-228.
- 41) "Mixed Convection in a Driven Cavity," by C. Benjapiyaporn, G. de Vahl Davis and E. Leonardi, 6th Australian Natural Convection Workshop, Murdoch University, ISBN 0-86905-723-5, Dec. 1999.
- 42) "A numerical study of Double-Diffusive Convection," by J. Kaenton, G. de Vahl Davis and E. Leonardi, 6th Australian Natural Convection Workshop, Murdoch University, ISBN 0-86905-723-5, Dec. 1999.
- 43) "Effects of finite wall conductivity on flow structures in natural convection," by E. Leonardi, T.A. Kowalewski, V. Timchenko, G. de Vahl Davis, CHMT99: Proc. of the International Conference on Computational Heat and Mass Transfer, edited by A.A. Mohamad and I. Sezai, Eastern Mediterranean University Printing-house, Gazimagusa, Nth Cyprus, pp. 182-190, 1999.
- 44) "An Experimental and Computational Study of the Bridgman Growth of an Alloy," by James E. Simpson, Suresh V. Garimella, and Henry C. de Groh III, Proceedings of Modeling of Casting, Welding and Advanced Solidification Processes IX, edited by P. Sahm, P. Hansen, and J. Conley, Aug. 2000, Aachen Germany.

- 45) "Solute Redistribution During Plane Front Solidification," by V. Timchenko, P.Y.P Chen, E. Leonardi, Gde Vahl Davis, R. Abbaschain, and H.C. de Groh III, 7th Australian Heat and Mass Transfer Conference, July 2000, Townsville, Australia.
- 46) "Seebeck Signals for Concentration Measurement During Solidification," by P.Y.P. Chen, V. Timchenko, E. Leonardi, G. de Vahl Davis, H.C. de Groh III and R. Abbaschian, Presented at the *7th Australasian Heat and Mass Transfer Conference*, Townsville, Queensland, July 2000.
- 47) "Effect of g-jitter on Directional Solidification of a Binary Alloy," by P. Santiviriyapanich, C. Benjapiyaporn, V. Timchenko, G. de Vahl Davis, E. Leonardi and H.C. de Groh III, 7th Australian Heat and Mass Transfer Conference, Townsville, Australia, July 2000.
- 48) "Crystal Growth Using MEPHISTO," by H.C de Groh III in R&T 1998, Research and Technology, NASA/TM-1999-208815, p. 156.
- 49) "A Computational Study of Transient Plane Front Solidification of Alloys in a Bridgman Apparatus Under Microgravity Conditions," by V. Timchenko, P.Y.P Chen, E. Leonardi, G. de Vahl Davis, and R. Abbaschian, *International Journal of Heat and Mass Transfer*, Vol. 43, pp. 963-980 (2000).
- 50) "Mixed Convection in a Driven Cavity," by C. Benjapiyaporn, G. de Vahl Davis and E. Leonardi., 3rd European Thermal Sciences Conference, edited by E.W.P Hahne, W. Heidemann, and K. Spindler, Edizioni ETS, Pisa, Italy, pp. 393-398, 2000.
- 51) "A Numerical Study of Double-Diffusive Convection," by J. Kaenton, G. de Vahl Davis and E. Leonardi, 3rd European Thermal Sciences Conference, edited by E.W.P Hahne, W. Heidemann, and K. Spindler, Edizioni ETS, Pisa, Italy, pp. 399-404, 2000.
- 52) "Free-Surface Effects on Solidification under Micro-Gravity Conditions," by M. Giangi, F. Stella, E. Leonardi, E. Bucchignani and G. de Vahl Davis, 3rd European Thermal Sciences Conference, edited by E.W.P Hahne, W. Heidemann, and K. Spindler, Edizioni ETS, Pisa, Italy, pp. 453-458, 2000.
- 53) "Computation of Anisotropic Conduction and Solidification," by J. Kaenton, G. de Vahl Davis and E. Leonardi, Presented at the 7th Australasian Heat and Mass Transfer Conference, 3-6 July, Townsville, Queensland, 2000.
- 54) "Crystal Growth by Travelling Heater Method in Microgravity," by G. de Vahl Davis and E. Leonardi, Chapter 9 in *Modelling of Transport Phenomena in Crystal Growth*, edited by J.S. Szmyd and K. Suzuki, WITpress, Southampton, 2000.
- 55) "Numerical Study of Marangoni Effects During Solidification Under Microgravity Conditions," by M. Giangi, F. Stella, E. Leonardi, E. Bucchignani and G. de Vahl Davis, Accepted for presentation and publication at CHT'01 Advances in Computational Heat Transfer, Palm Cove, Australia, 20-25 May, 2001.

- 56) “Computational Model for Solutal Convection during Directional Solidification,” by M. EL Ganaoui, A. Lamazouade, P. Bontoux, E. Leonardi and G. de Vahl Davis, Accepted for presentation and publication at CHT’01 Advances in Computational Heat Transfer, Palm Cove, Australia, 20–25 May, 2001.
- 57) “Anisotropy And Convection During Directional Solidification,” by J. Kaenton, G. de Vahl Davis, E. Leonardi and S.S. Leong, Accepted for presentation and publication at CHT’01 Advances in Computational Heat Transfer, Palm Cove, Australia, 20–25 May, 2001.
- 58) “A Numerical Study of the MEPHISTO Experiment,” by V. Timchenko, P.Y.P. Chen, E. Leonardi, G. de Vahl Davis and R. Abbaschian, Accepted for presentation and publication at CHT’01 Advances in Computational Heat Transfer, Palm Cove, Australia, 20–25 May, 2001.
- 59) “A study of the effects of g-jitter during the MEPHISTO Experiment,” by C. Benjapiyaporn, V. Timchenko, E. Leonardi, G. de Vahl Davis and H.C. de Groh III, Accepted for presentation and publication at CHT’01 Advances in Computational Heat Transfer, Palm Cove, Australia, 20–25 May, 2001.

Submitted for Publication

- 60) “A Numerical Method for Solidification of an Anisotropic Alloy,” by J. Kaenton, G. de Vahl Davis, E. Leonardi and S.S. Leong, Submitted for presentation at the European Community on Computational Methods in Applied Sciences (ECCOMAS) Computational Fluid Dynamics 2001 Conference, 4–7 September 2001.

Appendix B

MEPHISTO-4 Timeline, on USMP-4, STS-87

Stage Step	TYPE	V	Velocity [mm/hr]	Initial [mm]	Final [mm]	Duration [hr]	MEPH Time		D	H	M	(INITIAL FOR STAGE)		
							Begin [hr]	Final [hr]				MET [hr]	[days]	
1	CD		0.00	149	149	3.000	0.00		3.00	0	0	0.00	3.13	0.13
2	OH		0.00	149	149	5.000	3.00		8.00	0	3	0.00	6.13	0.26
3 A	HFF		0.00	149	149	1.500	8.00		9.50	0	8	0.00	11.13	0.46
	H		0.00	149	149	0.500	9.50		10.00	0	9	30.00	12.63	0.53
3 B	HFF		0.00	149	149	0.500	10.00		10.50	0	10	0.00	13.13	0.55
	H		0.00	149	149	0.500	10.50		11.00	0	10	30.00	13.63	0.57
3 C	HFF		0.00	149	149	0.500	11.00		11.50	0	11	0.00	14.13	0.59
	H		0.00	149	149	0.500	11.50		12.00	0	11	30.00	14.63	0.61
3 D	HFF		0.00	149	149	0.500	12.00		12.50	0	12	0.00	15.13	0.63
	H		0.00	149	149	0.500	12.50		13.00	0	12	30.00	15.63	0.65
3 E	HFF		0.00	149	149	3.500	13.00		16.50	0	13	0.00	16.13	0.67
	H		0.00	149	149	0.500	16.50		17.00	0	16	30.00	19.63	0.82
3 F	HMF		0.00	149	149	1.500	17.00		18.50	0	17	0.00	20.13	0.84
	H		0.00	149	149	0.500	18.50		19.00	0	18	30.00	21.63	0.90
3 G	HMF		0.00	149	149	0.500	19.00		19.50	0	19	0.00	22.13	0.92
	H		0.00	149	149	0.500	19.50		20.00	0	19	30.00	22.63	0.94
3 H	HMF		0.00	149	149	0.500	20.00		20.50	0	20	0.00	23.13	0.96
	H		0.00	149	149	0.500	20.50		21.00	0	20	30.00	23.63	0.98
3 I	HMF		0.00	149	149	4.000	21.00		25.00	0	21	0.00	24.13	1.01
	EH		0.00	149	149	1.783	25.00		26.78	1	1	0.00	28.13	1.17
7 A	PM	V3	-23.99	149	144	0.208	26.78		26.99	1	2	47.00	29.913	1.25
	EH		0.00	144	144	6.420	26.99		33.41	1	2	59.50	30.122	1.26
9 A	F	V1	6.67	144	149	0.750	33.37		34.12	1	9	22.20	36.5	1.52
	H		0.00	149	149	0.500	34.12		34.62	1	10	7.21	37.25	1.55
	M	V1	-6.67	149	144	0.750	34.62		35.37	1	10	37.21	37.75	1.57
	H		0.00	144	144	0.500	35.37		35.87	1	11	22.22	38.5	1.60
7 B	PM	V3	-23.99	144	139	0.208	35.87		36.08	1	11	52.22	39	1.63
	EH		0.00	139	139	0.500	36.08		36.58	1	12	4.73	39.209	1.63
9 B	F	V2	12.00	139	144	0.417	36.58		37.00	1	12	34.73	39.709	1.65
	H		0.00	144	144	0.500	37.00		37.50	1	12	59.73	40.126	1.67
	M	V2	-12.00	144	139	0.417	37.50		37.91	1	13	29.73	40.626	1.69
	H		0.00	139	139	0.500	37.91		38.41	1	13	54.74	41.042	1.71
10 A	F	V4	47.99	139	144	0.104	38.41		38.52	1	14	24.74	41.542	1.73
	H		0.00	144	144	1.000	38.52		39.52	1	14	30.99	41.646	1.74
	M	V4	-47.99	144	139	0.104	39.52		39.62	1	15	30.99	42.646	1.78
	H		0.00	139	139	1.000	39.62		40.62	1	15	37.24	42.751	1.78
	EH		0.00	139	139	3.907	40.62		44.53	1	16	37.24	43.751	1.82
10 B	F	V1	6.67	139	144	0.750	44.53		45.28	1	20	31.67	47.658	1.99
	H		0.00	144	144	1.000	45.28		46.28	1	21	16.69	48.408	2.02
	M	V1	-6.67	144	139	0.750	46.28		47.03	1	22	16.69	49.408	2.06
	H		0.00	139	139	1.000	47.03		48.03	1	23	1.70	50.158	2.09
	EH		0.00	139	139	2.175	48.03		50.20	2	0	1.70	51.158	2.13
7 C1	F	V3	23.99	139	148	0.375	50.20		50.58	2	2	12.20	53.333	2.22
	H		0.00	148	148	1.000	50.58		51.58	2	2	34.70	53.708	2.24
	M	V3	-23.99	148	139	0.375	51.58		51.95	2	3	34.70	54.708	2.28
	H		0.00	139	139	1.000	51.95		52.95	2	3	57.21	55.083	2.30
7 C2	PM	V3	-23.99	139	130	0.375	52.95		53.33	2	4	57.21	56.083	2.34
	EH		0.00	130	130	4.042	53.33		57.37	2	5	19.71	56.459	2.35
9 C	F	V3	23.99	130	140	0.417	57.37		57.79	2	9	22.23	60.501	2.52
	H		0.00	140	140	0.500	57.79		58.29	2	9	47.24	60.917	2.54
	M	V3	-23.99	140	130	0.417	58.29		58.70	2	10	17.24	61.417	2.56
	H		0.00	130	130	0.500	58.70		59.20	2	10	42.25	61.834	2.58
7 D	PM	V3	-23.99	130	115	0.625	59.20		59.83	2	11	12.25	62.334	2.60
	EH		0.00	115	115	2.000	59.83		61.83	2	11	49.76	62.959	2.62
9 D	F	V4	47.99	115	130	0.313	61.83		62.14	2	13	49.76	64.959	2.71
	H		0.00	130	130	0.500	62.14		62.64	2	14	8.51	65.272	2.72
	M	V4	-47.99	130	115	0.313	62.64		62.95	2	14	38.51	65.772	2.74
	H		0.00	115	115	0.500	62.95		63.45	2	14	57.27	66.084	2.75

3 I	HMF		0.00	149	149	4.000	21.00	25.00	0	21	0.00	24.13	1.01
	EH		0.00	149	149	1.783	25.00	26.78	1	1	0.00	28.13	1.17
7 A	PM	V3	-23.99	149	144	0.208	26.78	26.99	1	2	47.00	29.913	1.25
7 E	F	V3	23.99	115	135	0.834	63.45	64.29	2	15	27.27	66.584	2.77
	H		0.00	135	135	0.050	64.29	64.34	2	16	17.28	67.418	2.81
7 E1	PM	V3	-23.99	135	95	1.667	64.34	66.01	2	16	20.28	67.468	2.81
	EH		0.00	95	95	1.000	66.01	67.01	2	18	0.30	69.135	2.88
9 E	F	V5	95.98	95	115	0.208	67.01	67.21	2	19	0.30	70.135	2.92
	H		0.00	115	115	0.500	67.21	67.71	2	19	12.81	70.343	2.93
	M	V5	-95.98	115	95	0.208	67.71	67.92	2	19	42.81	70.843	2.95
	H		0.00	95	95	0.500	67.92	68.42	2	19	55.31	71.052	2.96
7 F	PM	V3	-23.99	95	75	0.834	68.42	69.26	2	20	25.31	71.552	2.98
	EH		0.00	75	75	0.865	69.26	70.12	2	21	15.32	72.385	3.02
7 G	PM	V3	-23.99	75	70	0.208	70.12	70.33	2	22	7.22	73.25	3.05
	EH		0.00	70	70	0.566	70.33	70.89	2	22	19.72	73.459	3.06
9 F	F	V3	23.99	70	90	0.834	70.89	71.73	2	22	53.68	74.025	3.08
	H		0.00	90	90	0.500	71.73	72.23	2	23	43.70	74.858	3.12
	M	V3	-23.99	90	70	0.834	72.23	73.06	3	0	13.70	75.358	3.14
	H		0.00	70	70	0.500	73.06	73.56	3	1	3.71	76.192	3.17
	EH		0.00	70	70	9.675	73.56	83.24	3	1	33.71	76.692	3.20
9 G	F	V1	6.67	70	75	0.750	83.24	83.99	3	11	14.21	86.367	3.60
	H		0.00	75	75	0.500	83.99	84.49	3	11	59.22	87.117	3.63
	M	V1	-6.67	75	70	0.750	84.49	85.24	3	12	29.22	87.617	3.65
	H		0.00	70	70	0.333	85.24	85.57	3	13	14.23	88.367	3.68
7 H	PM	V3	-23.99	70	65	0.208	85.57	85.78	3	13	34.23	88.701	3.70
	EH		0.00	65	65	2.000	85.78	87.78	3	13	46.74	88.909	3.70
9 H	F	V2	12.00	65	70	0.417	87.78	88.20	3	15	46.74	90.909	3.79
	H		0.00	70	70	0.500	88.20	88.70	3	16	11.74	91.326	3.81
	M	V2	-12.00	70	65	0.417	88.70	89.11	3	16	41.74	91.826	3.83
	H		0.00	65	65	0.500	89.11	89.61	3	17	6.75	92.242	3.84
7 I	PM	V3	-23.99	65	55	0.417	89.61	90.03	3	17	36.75	92.742	3.86
	EH		0.00	55	55	1.190	90.03	91.22	3	18	1.75	93.159	3.88
9 M	F	V5	95.98	55	75	0.208	91.22	91.43	3	19	13.15	94.349	3.93
	H		0.00	75	75	0.500	91.43	91.93	3	19	25.66	94.558	3.94
	M	V5	-95.98	75	55	0.208	91.93	92.14	3	19	55.66	95.058	3.96
	H		0.00	55	55	0.500	92.14	92.64	3	20	8.16	95.266	3.97
	EH		0.00	55	55	4.065	92.64	96.70	3	20	38.16	95.766	3.99
9 O	F	V6	144.04	55	75	0.139	96.70	96.84	4	0	42.06	99.831	4.16
	H		0.00	75	75	0.500	96.84	97.34	4	0	50.39	99.97	4.17
	M	V6	-144.04	75	55	0.139	97.34	97.48	4	1	20.39	100.47	4.19
	H		0.00	55	55	0.500	97.48	97.98	4	1	28.72	100.61	4.19
	EH		0.00	55	55	8.200	97.98	106.18	4	1	58.72	101.11	4.21
9 N	F	V3	23.99	55	75	0.834	106.18	107.01	4	10	10.72	109.31	4.55
	H		0.00	75	75	0.500	107.01	107.51	4	11	0.74	110.14	4.59
	M	V3	-23.99	75	55	0.834	107.51	108.35	4	11	30.74	110.64	4.61
	H		0.00	55	55	0.500	108.35	108.85	4	12	20.75	111.48	4.64
	EH		0.00	55	55	3.700	108.85	112.55	4	12	50.75	111.98	4.67
9 P	F	V2	12.00	55	75	1.667	112.55	114.21	4	16	32.75	115.68	4.82
	H		0.00	75	75	0.500	114.21	114.71	4	18	12.77	117.34	4.89
	M	V2	-12.00	75	55	1.667	114.71	116.38	4	18	42.77	117.84	4.91
	H		0.00	55	55	0.500	116.38	116.88	4	20	22.80	119.51	4.98
	EH		0.00	55	55	5.860	116.88	122.74	4	20	52.80	120.01	5.00
11 Q1	F	V2	12.00	55	60	0.417	122.74	123.16	5	2	44.40	125.87	5.24
	H		0.00	60	60	0.500	123.16	123.66	5	3	9.40	126.29	5.26
11 Q2	F	V2	12.00	60	65	0.417	123.66	124.07	5	3	39.40	126.79	5.28
	H		0.00	65	65	0.500	124.07	124.57	5	4	4.41	127.2	5.30
7 Q	M	V3	-23.99	65	55	0.417	124.57	124.99	5	4	34.41	127.7	5.32
	EH		0.00	55	55	7.880	124.99	132.87	5	4	59.42	128.12	5.34
9 I	F	V1	6.67	55	70	2.251	132.87	135.12	5	12	52.22	136	5.67

3 I	HMF		0.00	149	149	4.000	21.00	25.00	0	21	0.00	24.13	1.01
	EH		0.00	149	149	1.783	25.00	26.78	1	1	0.00	28.13	1.17
7 A	PM	V3	-23.99	149	144	0.208	26.78	26.99	1	2	47.00	29.913	1.25
	H		0.00	70	70	0.500	135.12	135.62	5	15	7.25	138.25	5.76
	M	V1	-6.67	70	55	2.251	135.62	137.87	5	15	37.25	138.75	5.78
	H		0.00	55	55	0.500	137.87	138.37	5	17	52.28	141	5.88
7 J	PM	V3	-23.99	55	45	0.417	138.37	138.79	5	18	22.28	141.5	5.90
	EH		0.00	45	45	3.180	138.79	141.97	5	18	47.29	141.92	5.91
9 J	F	V1.5	10.66	45	55	0.938	141.97	142.91	5	21	58.09	145.1	6.05
	H		0.00	55	55	0.500	142.91	143.41	5	22	54.35	146.04	6.08
	M	V1.5	-10.66	55	45	0.938	143.41	144.34	5	23	24.35	146.54	6.11
	H		0.00	45	45	0.500	144.34	144.84	6	0	20.62	147.47	6.14
7 K	PM	V3	-23.99	45	20	1.042	144.84	145.89	6	0	50.62	147.97	6.17
	EH		0.00	20	20	0.985	145.89	146.87	6	1	53.13	149.02	6.21
9 K	F	V5	95.98	20	55	0.365	146.87	147.24	6	2	52.23	150	6.25
	H		0.00	55	55	0.500	147.24	147.74	6	3	14.11	150.37	6.27
	M	V5	-95.98	55	20	0.365	147.74	148.10	6	3	44.11	150.87	6.29
	H		0.00	20	20	0.500	148.10	148.60	6	4	6.00	151.23	6.30
	EH		0.00	20	20	1.271	148.60	149.87	6	4	36.00	151.73	6.32
9 L	F	V6	144.04	20	55	0.243	149.87	150.11	6	5	52.23	153	6.38
	H		0.00	55	55	0.500	150.11	150.61	6	6	6.80	153.24	6.39
	M	V6	-144.04	55	20	0.243	150.61	150.86	6	6	36.80	153.74	6.41
	H		0.00	20	20	0.500	150.86	151.36	6	6	51.38	153.99	6.42
	EH		0.00	20	20	5.700	151.36	157.06	6	7	21.38	154.49	6.44
11 R	F	V1	6.67	20	25	0.750	157.06	157.81	6	13	3.38	160.19	6.67
	H		0.00	25	25	2.500	157.81	160.31	6	13	48.40	160.94	6.71
9 R	F	V1	6.67	25	35	1.500	160.31	161.81	6	16	18.40	163.44	6.81
	H		0.00	35	35	0.500	161.81	162.31	6	17	48.42	164.94	6.87
	M	V1	-6.67	35	25	1.500	162.31	163.81	6	18	18.42	165.44	6.89
	H		0.00	25	25	0.090	163.81	163.90	6	19	48.44	166.94	6.96
7 R	PM	V3	-23.99	25	1	1.000	163.90	164.90	6	19	53.84	167.03	6.96
	EH		0.00	1	1	0.600	164.90	165.50	6	20	53.86	168.03	7.00
11 A	F	V1	6.67	1	5	0.600	165.50	166.10	6	21	29.86	168.63	7.03
	EH		0.00	5	5	6.000	166.10	172.10	6	22	5.86	169.23	7.05
11 B	F	V2	12.00	5	10	0.417	172.10	172.51	7	4	5.86	175.23	7.30
	EH		0.00	10	10	9.359	172.51	181.87	7	4	30.87	175.64	7.32
9 S	F	V4	47.99	10	25	0.313	181.87	182.19	7	13	52.41	185	7.71
	H		0.00	25	25	0.500	182.19	182.69	7	14	11.17	185.32	7.72
	M	V4	-47.99	25	10	0.313	182.69	183.00	7	14	41.17	185.82	7.74
	H		0.00	10	10	0.500	183.00	183.50	7	14	59.92	186.13	7.76
	EH		0.00	10	10	3.000	183.50	186.50	7	15	29.92	186.63	7.78
8 A	F	V0.5	2.67	10	15	1.875	186.50	188.37	7	18	29.92	189.63	7.90
	H		0.00	15	15	1.000	188.37	189.37	7	20	22.45	191.5	7.98
	M	V0.5	-2.67	15	10	1.875	189.37	191.25	7	21	22.45	192.5	8.02
	H		0.00	10	10	1.000	191.25	192.25	7	23	14.98	194.38	8.10
	EH		0.00	10	10	13.878	192.25	206.13	8	0	14.98	195.38	8.14
9 T	F	V3	23.99	10	35	1.042	206.13	207.17	8	14	7.66	209.26	8.72
	H		0.00	35	35	0.500	207.17	207.67	8	15	10.17	210.3	8.76
	M	V3	-23.99	35	10	1.042	207.67	208.71	8	15	40.17	210.8	8.78
	H		0.00	10	10	0.500	208.71	209.21	8	16	42.69	211.84	8.83
	EH		0.00	10	10	5.758	209.21	214.97	8	17	12.69	212.34	8.85
9 U	F	V3.5	35.99	10	35	0.695	214.97	215.66	8	22	58.17	218.1	9.09
	H		0.00	35	35	0.500	215.66	216.16	8	23	39.84	218.79	9.12
	M	V3.5	-35.99	35	10	0.695	216.16	216.86	9	0	9.84	219.29	9.14
	H		0.00	10	10	0.500	216.86	217.36	9	0	51.52	219.99	9.17
	EH		0.00	10	10	5.794	217.36	223.15	9	1	21.52	220.49	9.19
9 V	F	V2.5	18.67	10	20	0.536	223.15	223.69	9	7	9.16	226.28	9.43
	H		0.00	20	20	0.500	223.69	224.19	9	7	41.30	226.82	9.45
	M	V2.5	-18.67	20	10	0.536	224.19	224.72	9	8	11.30	227.32	9.47

3 I	HMF		0.00	149	149	4.000	21.00	25.00	0	21	0.00	24.13	1.01
	EH		0.00	149	149	1.783	25.00	26.78	1	1	0.00	28.13	1.17
7 A	PM	V3	-23.99	149	144	0.208	26.78	26.99	1	2	47.00	29.913	1.25
	H		0.00	10	10	0.500	224.72	225.22	9	8	43.45	227.85	9.49
	EH		0.00	10	10	6.207	225.22	231.43	9	9	13.45	228.35	9.51
9 W	F	V2.5	18.67	10	15	0.268	231.43	231.70	9	15	25.87	234.56	9.77
	H		0.00	15	15	0.500	231.70	232.20	9	15	41.94	234.83	9.78
	M	V2.5	-18.67	15	10	0.268	232.20	232.47	9	16	11.94	235.33	9.81
	H		0.00	10	10	0.500	232.47	232.97	9	16	28.01	235.6	9.82
	EH		0.00	10	10	7.610	232.97	240.58	9	16	58.01	236.1	9.84
12	F	V3	23.99	10	25	0.625	240.58	241.20	10	0	34.61	243.71	10.15
	EH		0.00	25	25	1.668	241.20	242.87	10	1	12.12	244.33	10.18
9 X	F	V3	23.99	25	40	0.625	242.87	243.50	10	2	52.20	246	10.25
	H		0.00	40	40	0.500	243.50	244.00	10	3	29.71	246.63	10.28
	M	V3	-23.99	40	25	0.625	244.00	244.62	10	3	59.71	247.13	10.30
	H		0.00	25	25	0.025	244.62	244.65	10	4	37.22	247.75	10.32
9 Y	F	V1	6.67	25	30	0.750	244.65	245.40	10	4	38.72	247.78	10.32
	H		0.00	30	30	0.500	245.40	245.90	10	5	23.73	248.53	10.36
	M	V1	-6.67	30	25	0.750	245.90	246.65	10	5	53.73	249.03	10.38
	H		0.00	25	25	0.019	246.65	246.66	10	6	38.74	249.78	10.41
9 Z	F	V5	95.98	25	45	0.208	246.66	246.87	10	6	39.88	249.79	10.41
	H		0.00	45	45	0.500	246.87	247.37	10	6	52.38	250	10.42
	M	V5	-95.98	45	25	0.208	247.37	247.58	10	7	22.38	250.5	10.44
	H		0.00	25	25	0.500	247.58	248.08	10	7	34.89	250.71	10.45
	EH		0.00	25	25	1.500	248.08	249.58	10	8	4.89	251.21	10.47
9 AA	F	V5	95.98	25	45	0.208	249.58	249.79	10	9	34.89	252.71	10.53
	H		0.00	45	45	0.500	249.79	250.29	10	9	47.39	252.92	10.54
	M	V5	-95.98	45	25	0.208	250.29	250.50	10	10	17.39	253.42	10.56
	H		0.00	25	25	0.500	250.50	251.00	10	10	29.89	253.63	10.57
	EH		0.00	25	25	6.872	251.00	257.87	10	10	59.89	254.13	10.59
13	F	V5	95.98	25	45	0.208	257.87	258.08	10	17	52.21	261	10.88
	EH		0.00	45	45	2.500	258.08	260.58	10	18	4.72	261.21	10.88
11 C	F	V4	47.99	45	60	0.313	260.58	260.89	10	20	34.72	263.71	10.99
	EH		0.00	60	60	3.729	260.89	264.62	10	20	53.47	264.02	11.00
14	F	V3	23.99	60	90	1.250	264.62	265.87	11	0	37.21	267.75	11.16
	EH		0.00	90	90	6.000	265.87	271.87	11	1	52.23	269	11.21
11 D	F	V6	144.04	90	105	0.104	271.87	271.97	11	7	52.23	275	11.46
	EH		0.00	105	105	4.896	271.97	276.87	11	7	58.48	275.1	11.46
15	F	V5	95.98	105	125	0.208	276.87	277.08	11	12	52.24	280	11.67
	EH		0.00	125	125	5.791	277.08	282.87	11	13	4.74	280.21	11.68
8 D	F	V0.6	4.00	125	130	1.250	282.87	284.12	11	18	52.20	286	11.92
	H		0.00	130	130	1.000	284.12	285.12	11	20	7.20	287.25	11.97
	M	V0.6	-4.00	130	125	1.250	285.12	286.37	11	21	7.20	288.25	12.01
	H		0.00	125	125	1.000	286.37	287.37	11	22	22.20	289.5	12.06
	EH		0.00	125	125	1.500	287.37	288.87	11	23	22.20	290.5	12.10
8 E	F	V0.8	5.33	125	130	0.938	288.87	289.81	12	0	52.20	292	12.17
	H		0.00	130	130	1.000	289.81	290.81	12	1	48.45	292.94	12.21
	M	V0.8	-5.33	130	125	0.938	290.81	291.75	12	2	48.45	293.94	12.25
	H		0.00	125	125	1.000	291.75	292.75	12	3	44.70	294.88	12.29
	EH		0.00	125	125	2.000	292.75	294.75	12	4	44.70	295.88	12.33
9 AB	F	V3	23.99	125	140	0.625	294.75	295.37	12	6	44.70	297.88	12.41
	H		0.00	140	140	0.500	295.37	295.87	12	7	22.21	298.5	12.44
	M	V3	-23.99	140	125	0.625	295.87	296.50	12	7	52.21	299	12.46
	H		0.00	125	125	0.500	296.50	297.00	12	8	29.72	299.63	12.48
	EH		0.00	125	125	9.875	297.00	306.87	12	8	59.72	300.13	12.51
16	F	V3	23.99	125	140	0.625	306.87	307.50	12	18	52.22	310	12.92
	EH		0.00	140	140	2.000	307.50	309.50	12	19	29.73	310.63	12.94
11 E	F	V2	12.00	140	144	0.333	309.50	309.83	12	21	29.73	312.63	13.03
	EH		0.00	144	144	4.041	309.83	313.87	12	21	49.73	312.96	13.04

3	I	HMF		0.00	149	149	4.000	21.00	25.00	0	21	0.00	24.13	1.01
		EH		0.00	149	149	1.783	25.00	26.78	1	1	0.00	28.13	1.17
7	A	PM	V3	-23.99	149	144	0.208	26.78	26.99	1	2	47.00	29.913	1.25
11	F	F	V1	6.67	144	149	0.750	313.87	314.62	13	1	52.22	317	13.21
17		Q			149	149	0.017	314.62	314.64	13	2	37.23	317.75	13.24
18		CF			149	149	7.000	314.64	321.64	13	2	38.23	317.77	13.24
19		DE			149	149	0.083	321.64	321.72	13	9	38.23	324.77	13.53

Time line Information Sheet

V0.5 2.666 HT

V0.6 4 0.50

V0.8 5.333 MET Shift

V1 6.665 3.13

V1.5 10.66

V2 12

V2.5 18.67

V3 23.99

V3.5 35.99

V4 47.99

V5 95.98

V6 144

M Melt
F Freeze
PM Primary Melt
EH Extended hold
H Hold
CD Cold Degassing
OH Overall heat
HFF Heat Fixed Furnace
HMF Heat Movable Furnace
Q Quench
CF Cool Furnace
DE Deactivate

References

- Abbaschian, R., et al., 1995, A Study of Directional Solidification of Faceted Bi-Sn Alloys in Microgravity. AIAA Paper 95-0608.
- Abbaschian, R., et al., 1996, A Study of Directional Solidification of Faceted Bi-Sn Alloys in Microgravity. Solidification Science and Processing, I. Ohnaka and D.M. Stefanescu, eds., The Minerals, Metals and Materials Society, Warrendale, PA.
- Buell, C.H., and Shuck, F.O., 1970, Diffusion in the Liquid Bi-Sn System. Metall. Trans., vol. 1, pp. 1875-1880.
- CFX 4.2: Solver, 1997, Harwell Laboratory, Didcot, Oxfordshire, OX11 0RA, United Kingdom.
- Chen, P.Y.P., et al., 1998, Numerical Study of Directional Solidification and Melting in Microgravity. Proceedings of the 1998 ASME International Mechanical Engineering Congress and Exposition, vol. 361-3, pp. 75-83.
- Chen, P.Y.P., et al., 2000, Seebeck Signals for Concentration Measurement During Solidification. Presented at the 7th Australasian Heat and Mass Transfer Conference, Townsville, Australia.
- Coriell, S.R., and Sekerka, R.F., 1976, The Effect of the Anisotropy of Surface Tension and Interface Kinetics on Morphological Stability. J. Cryst. Growth, vol. 34, no. 2, pp. 157-163.
- Coriell, S.R., and McFadden, G.B., 1993, Morphological Stability. Handbook of Crystal Growth, vol. 1, D.T.J. Hurle, ed., Elsevier, p. 785.
- Coriell, S.R., Murray, B.T., and Chernov, A.A., 1994, Kinetic Self-Stabilization of a Stepped Interface—Binary Alloy Solidification. J. Cryst. Growth, vol. 141, no. 1-2, pp. 219-233.
- de Groh, Henry C., III, and Lindstrom, 1994, Tiffany: Interface Shape and Convection During Solidification and Melting of Succinonitrile. NASA TM-106487.
- de Groh, Henry C., III, Johnston, J. Christopher, and Wei, Bingbo, 1998, Void Management in MEPHISTO and Other Space Experiments. Journal of the Japan Society of Microgravity Application: Proceedings of the Joint 1st Pan-Pacific Basin Workshop and the 4th Japan-China Workshop on Microgravity Sciences, vol. 15, pp. 46-50.
- Johnston, J.C., and de Groh, H.C., III, 2000, Void Management in Space Experiments. NASA Glenn Research Center Disclosure of Invention and New Technology, submitted.
- Kaddeche, S., et al., 1996, Interface Curvature and Convection Related Macroseggregation in the Vertical Bridgman Configuration. J. Cryst. Growth, vol. 158, no. 1-2, pp. 144-152.
- Mullins, W.W., and Sekerka, R.F., 1964, Stability of a Planar Interface During Solidification on a Dilute Binary Alloy. J. Appl. Phys., vol. 35, no. 2, pp. 444-451.
- Niwa, K., et al., 1957, Studies on Diffusion in Molten Metals. AIME Tran., vol. 209, pp. 96-101.
- Peteves, Stathis D., 1986, Growth Kinetics of Faceted Solid-Liquid Interfaces (Crystal Growth). Ph.D. Thesis, Univ. of Florida.
- Peteves, S.D., and Abbaschian, R., 1991, Growth-Kinetics of Solid-Liquid Ga Interfaces. 1—Experimental. Metall. T-A, vol. 22, no. 6, pp. 1259-1270.

- Rouzaud, A., Favier, J.J., and Thevenard, D., 1988, A Space Instrument for Fundamental Materials Science Problems—The Mephisto Program. *Adv. Space Res.*, vol. 8, no. 12, pp. 45–59.
- Smith, V.G., Tiller, W.A., Rutter, J.W., 1955, A Mathematical Analysis of Solute Redistribution During Solidification. *Can. J. Phys.*, vol. 33, no. 12, pp. 723–745.
- Sixou, B., Rouzaud, A., Favier, J.J., 1994, Growth-Kinetics in Ultra-Pure Bismuth Using a Thermoelectric Method for Interface Temperature—Measurements. *J. Cryst. Growth*, vol. 137, no. 3–4, pp. 605–609.
- Tiller, W.A., and Rutter, J.W., 1956, The Effect of Growth Conditions Upon the Solidification of a Binary Alloy. *Vol. 34, no. 1*, pp. 97–121.
- Timchenko, V., et al., 1998, Directional Solidification in Microgravity. *Heat Transfer 1998: Proceedings of the Eleventh International Heat Transfer Conference*, J.S. Lee, ed., Korean Society of the Eleventh International Heat Transfer Conference, Seoul, Korea.
- Timchenko, V., et al., 2000, A Computational Study of Transient Plane Front Solidification of Alloys in a Bridgman Apparatus Under Microgravity Conditions. *Int. J. Heat Mass Transfer*, vol. 43, no. 6, pp. 963–980.
- Trivedi, R., 1990, Effects of Anisotropy Properties on Interface Pattern Formation. *Appl. Mech. Rev.*, vol. 43, no. 5, pt. 2, pp. S79–S84.
- Trivedi, R., Seetharaman, V., and Eshelman, M.A., 1991, The Effects of Interface Kinetics Anisotropy on the Growth Direction of Cellular Microstructures. *Metall. T-A*, vol. 22, no. 2, pp. 585–593.
- Voller, V.R., Brent, A.D., and Prakash, C., 1989, The Modeling of Heat, Mass and Solute Transport in Solidification Systems. *Int. J. Heat Mass Transfer*, vol. 32, no. 9, pp. 1719–1731.
- Yao, M.W., and de Groh, H., 1993, Three-Dimensional Finite-Element Method Simulation of Bridgman Crystal-Growth and Comparison With Experiments. *Numer. Heat Transfer, Part A—Applications*. Vol. 24, no. 4, pp. 393–412.
- Young, G.W., Davis, S.H., and Brattkus, K., 1987, Anisotropic Interface Kinetics and Tilted Cells in Unidirectional Solidification. *J. Cryst. Growth*, vol. 83, no. 4, pp. 560–571.

Table 1. Growth Conditions and Velocity Values During Final Solidification Steps

Name	MET TIME (Day/Hr.)	Velocity ($\mu\text{m}/\text{Sec.}$)	Start Position (mm)	End Position (mm)
11A (V1)	7/1	1.869	1	5
11B (V2)	7/9	3.426	5	10
12 (V3)	10/4	6.763	10	25
13 (V5)	10/21	26.86	25	45
11C (V4)	11/0	13.47	45	60
14 (V3)	11/4	6.743	60	90
11D (V6)	11/11	40.29	90	105
14 (V3)	11/16	27.01	105	125
16 (V3)	12/23	6.737	125	140
11E (V2)	13/0	3.322	140	144
11F (V1)	13/5	1.823	144	148

Notes:

Start and End Positions in MEPHISTO Coordinates

MET: Mission Elapsed Time

Table 2. Sample Breakdown Distance

Event Description (Seebeck Sample)	Distance Solidified (mm)	Distance From Start to Breakdown (mm) Seebeck	Distance From Start to Breakdown (mm) Peltier	Distance From Start to Breakdown (mm) Quench	Location
V1 11A	4	Planar	Planar	Planar	Inside and Outside Capillary
V2 11B	5	Planar	Planar	Planar	Inside and Outside Capillary
V3 12	15	3.6 3.7 3.7	3.4 4.6 3.8	2.6 Non Visible 3.2	Outside Capillary Inside Capillary Outside Capillary
V5 Start, 13	20	0.7 0.5 0.4	0.2 0.8 0.9	1.5 0.8 0.6	Outside Capillary Inside Capillary Outside Capillary
V4 11C	15	0.7 0.8 1	1.4 1.6 1.6	1.3 0.7 1.2	Outside Capillary Inside Capillary Outside Capillary
V3 14	30	2 1.7 2	None Visible 3.2 3.9	3.1 3.1 3.1	Outside Capillary Inside Capillary Outside Capillary
V6 11D	15	0.2	0.6	0.3	6 mm Tube Different Grains
V5 Start, 15	20	0.7	1	0.8	6 mm Tube Different Grains
V3 Start, 16	15	3.5	3.6	3.1	6 mm Tube Different Grains
V2 start, 11E	4	Planar	Planar	Planar	Inside and Outside Capillary
V1 Start, 11F	4	Planar	Planar	Planar	Inside and Outside Capillary

Table 3. Microstructural Distance and Calculated Structural Seebeck Coefficient

Event Description	Distance (mm)	Plane Front Zone (mm)	Cellular Zone (mm)	Coarsened Cellular Zone (mm)	Calculated Structural Seebeck Coefficient (mv/K)
Photo Start	-10.8				-0.04
V1 Start, 11A	0	4			-0.055
V2 Start, 11B	4	5			-0.055
V3 Start, 12	9	3.65			-0.055
V3 Breakdown	12.65		8.05		-0.03
Breakdown End	20.7			3.3	-0.005
V5 Start, 13	24	0.52			-0.055
V5 Breakdown	24.52		18.18		-0.015
Breakdown End	42.7			1.3	-0.05
V4 Start, 11C	44	0.82			-0.055
V4 Breakdown	44.82		9.88		-0.025
Breakdown End	54.7			4.3	-0.05
V3 Start, 14	59	1.9			-0.055
V3 Breakdown	60.9		23.3		-0.03
Breakdown End	84.2			4.8	-0.05
V6 Start, 11D	89	0.2			-0.055
V6 Breakdown	89.2		12		-0.01
Breakdown End	101.2			3.8	-0.05
V5 Start, 15	104	0.65			-0.055
V5 Breakdown	104.65		14.55		-0.01
Breakdown End	119.2			4.8	-0.05
V3 Start, 16	124	3.5			-0.055
V3 Breakdown	127.5		6.2		-0.03
Breakdown End	133.7			5.3	-0.05
V2 start, 11E	139	4	-	-	-0.055
V1 Start, 11F	143	4	-	-	-0.055
End of Translation	147				

Table 4. Comparison of Two Methods

Method	$C_{\min}(\text{at}\%)$	$C_{\max}(\text{at}\%)$	$ U_{\max} (\text{m/s})$	$V_{\max}(\text{m/s})$	$V_{\min}(\text{m/s})$	CPU time(s)
SOLCON	10.04	11.54	2.282×10^{-6}	5.943×10^{-7}	-1.224×10^{-6}	80296
CFX	9.98	11.28	2.311×10^{-6}	5.977×10^{-7}	-1.217×10^{-6}	841800

Table 5. Effect of g-jitter on Segregation

Amplitude (m/s^2)	Frequency (Hz)	Maximum velocity (mm/s)		Maximum segregation (%)	Segregation at 500s (%)
		U_{\max}	V_{\max}		
$10^{-2}g$	0.01	2.50	0.89	188.7	90.0
	0.05	1.26	0.78	192.4	188.0
	0.1	0.75	0.32	39.9	39.9
	0.5	0.19	9.66×10^{-2}	20.2	20.2
	1.0	9.78×10^{-2}	4.81×10^{-2}	10.9	10.9
$10^{-3}g$	0.01	0.22	0.11	38.2	33.0
	0.05	0.12	6.75×10^{-2}	11.3	10.3
	0.1	7.49×10^{-2}	4.13×10^{-2}	8.9	8.9
	0.5	1.90×10^{-2}	9.78×10^{-3}	3.1	3.1
	1.0	9.95×10^{-3}	4.94×10^{-3}	2.5	2.5
$10^{-4}g$	0.01	2.15×10^{-2}	1.15×10^{-2}	4.9	4.3
	0.05	1.27×10^{-2}	6.86×10^{-3}	2.7	2.7
	0.1	7.68×10^{-3}	4.23×10^{-3}	2.3	2.3
	0.5	2.06×10^{-3}	1.08×10^{-3}	1.8	1.8
	1.0	1.14×10^{-3}	6.02×10^{-4}	1.8	1.8
$10^{-5}g$	0.01	2.41×10^{-3}	1.27×10^{-3}	2.0	2.0
	0.05	1.47×10^{-3}	7.96×10^{-4}	1.8	1.8
	0.1	9.66×10^{-4}	5.29×10^{-4}	1.8	1.8
	0.5	3.85×10^{-4}	2.12×10^{-4}	1.8	1.8
	1.0	2.97×10^{-4}	1.65×10^{-4}	1.8	1.8
Steady at $g = 10^{-6}g$		2.28×10^{-4}	1.20×10^{-4}	1.8	1.8

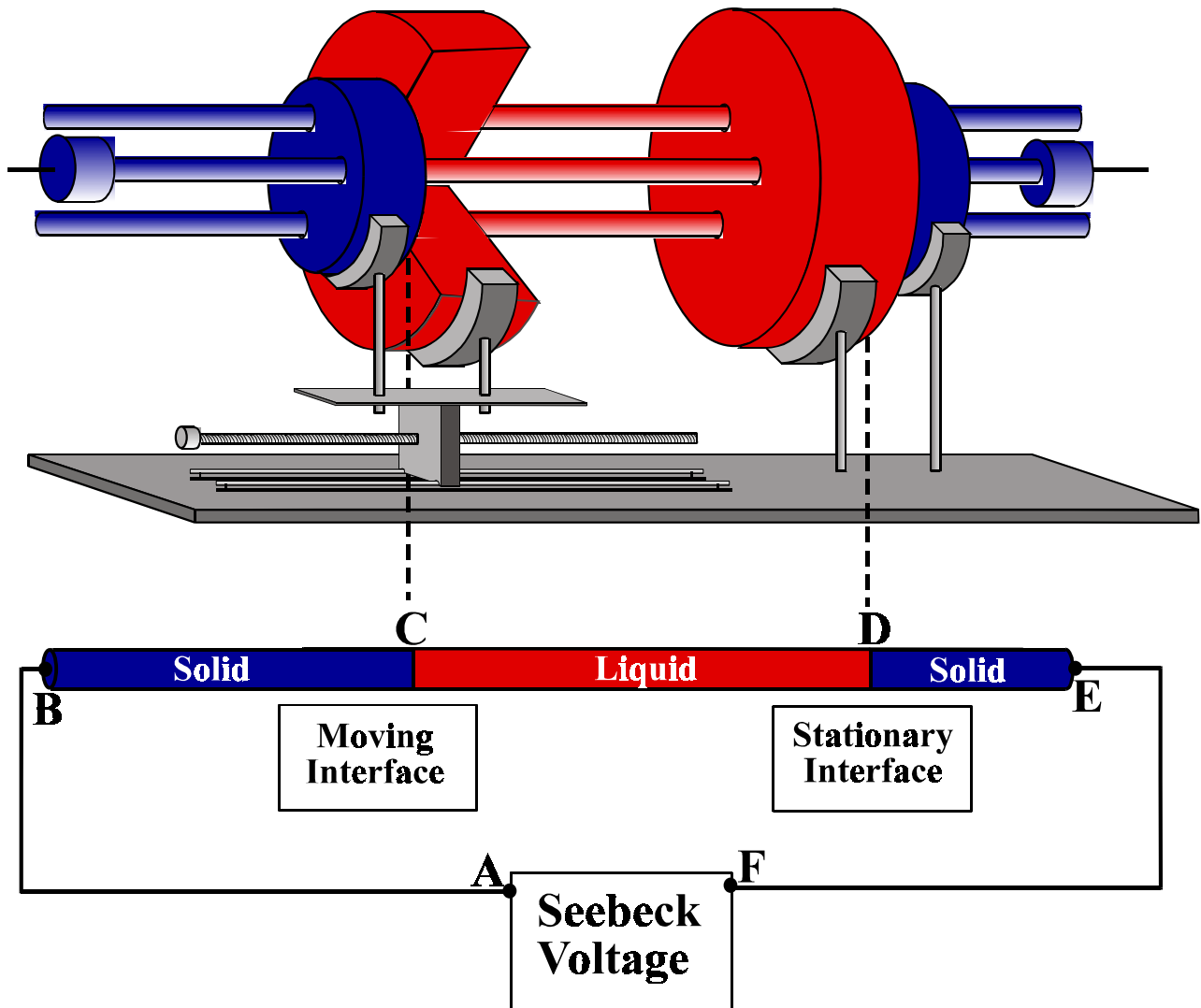


Figure 1. MEPHISTO Apparatus is shown with two furnace/heat sink structures. The three long cylinders going through the two furnace/heat sink structures are the Quenching, Peltier, and Seebeck Samples. The three samples are subjected to the same temperature field, except the Seebeck sample has additional temperature regulation to match the temperature at its ends. The furnace/heat sink structure on the left can move, causing melting or solidification at the moving solid-liquid interface. In the schematic of the Seebeck sample the ends are marked B and E while the solid-liquid interfaces are marked C and D. When solidifying/melting at the moving interface, the temperatures at C and D will not be the same due to compositional and kinetic undercooling/superheating.

Bi-Sn Phase Diagram

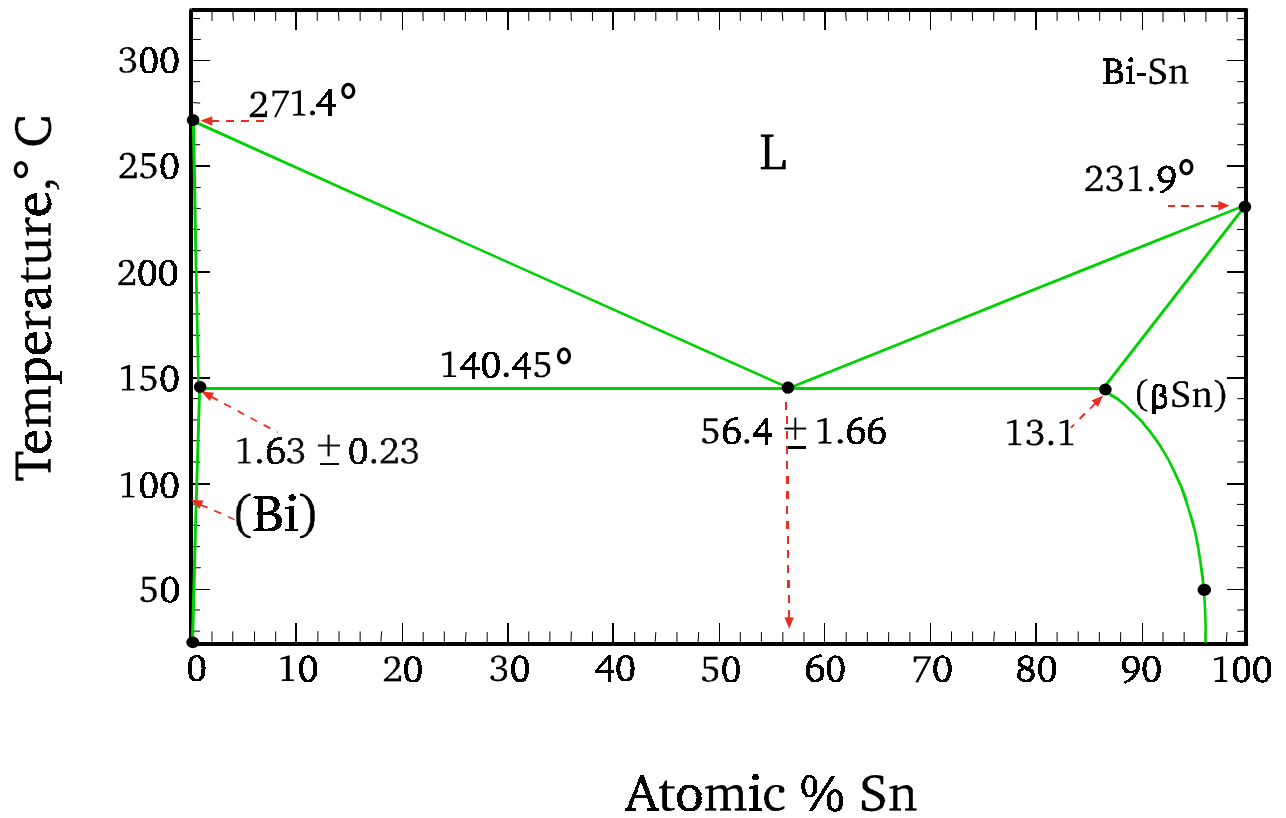


Figure 2. Phase Diagram for the bismuth-tin system.

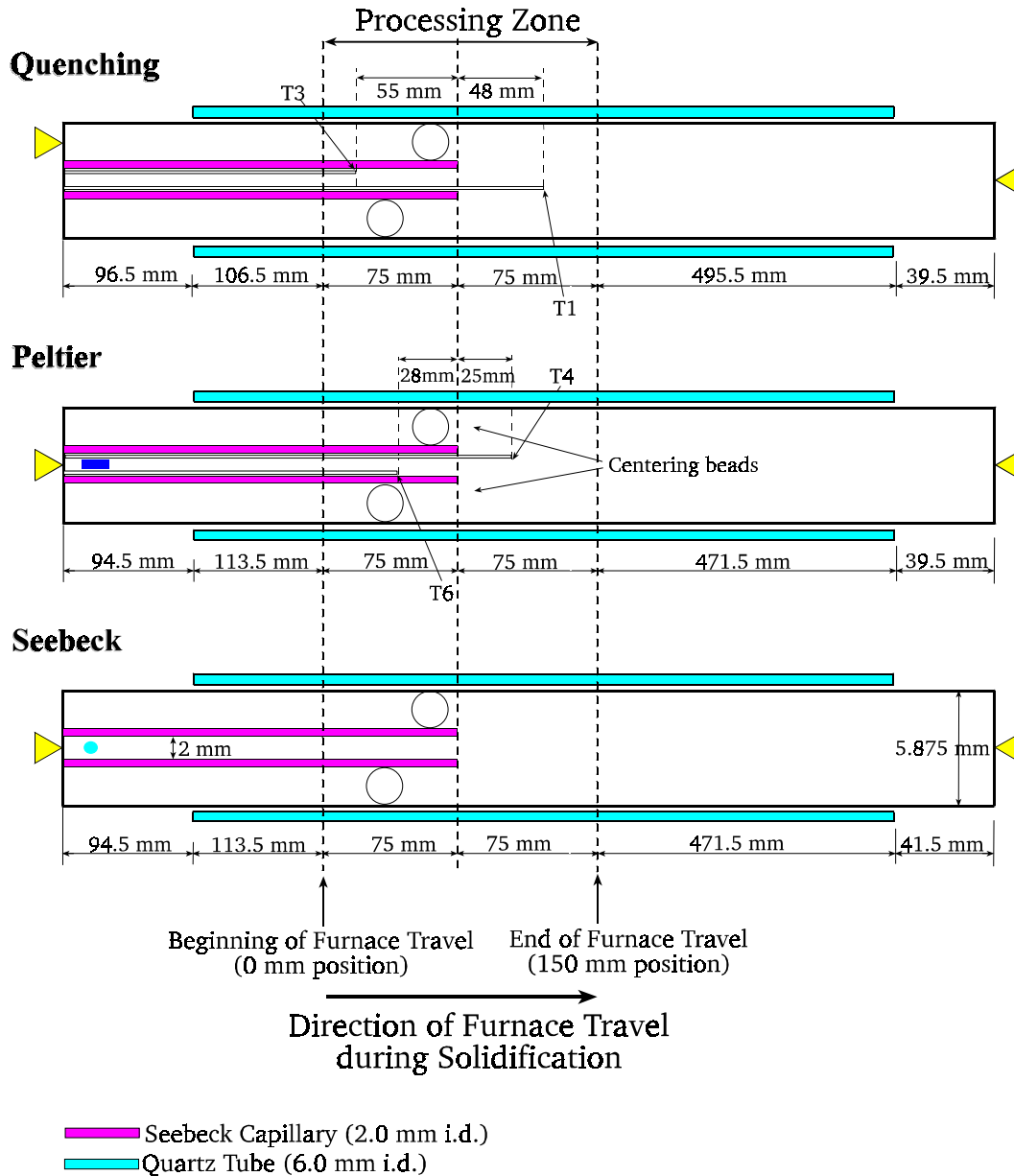


Figure 3. Configurations for the Quenching, Peltier, and Seebeck samples. The samples consist of 5.87 mm diameter cylinders of Bi- 1 atomic % Sn alloy which are contained in quartz tubing. The four thermocouples (the Quenching and Peltier each have two) are labeled T1, T3, T4 and T6. The Seebeck capillary is a 2 mm i.d. quartz tube on the left of each sample. The triangles indicate position of electrical contacts. A small cut in the capillary tube for the Peltier sample allows current to flow in the alloy inside and outside the capillary.



Figure 6. Microstructure overview of the space processed sample.

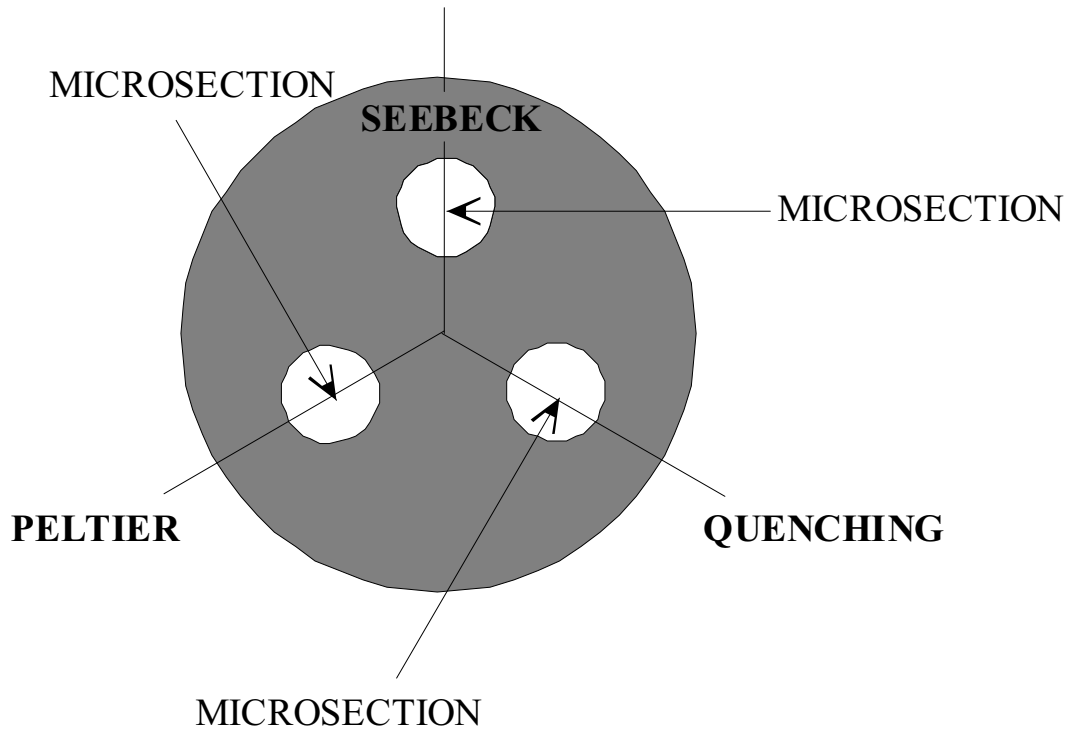


Figure 7. Orientation of microsections of the samples are taken in a direction pointing to the diffuser center and thus thermally equivalent.

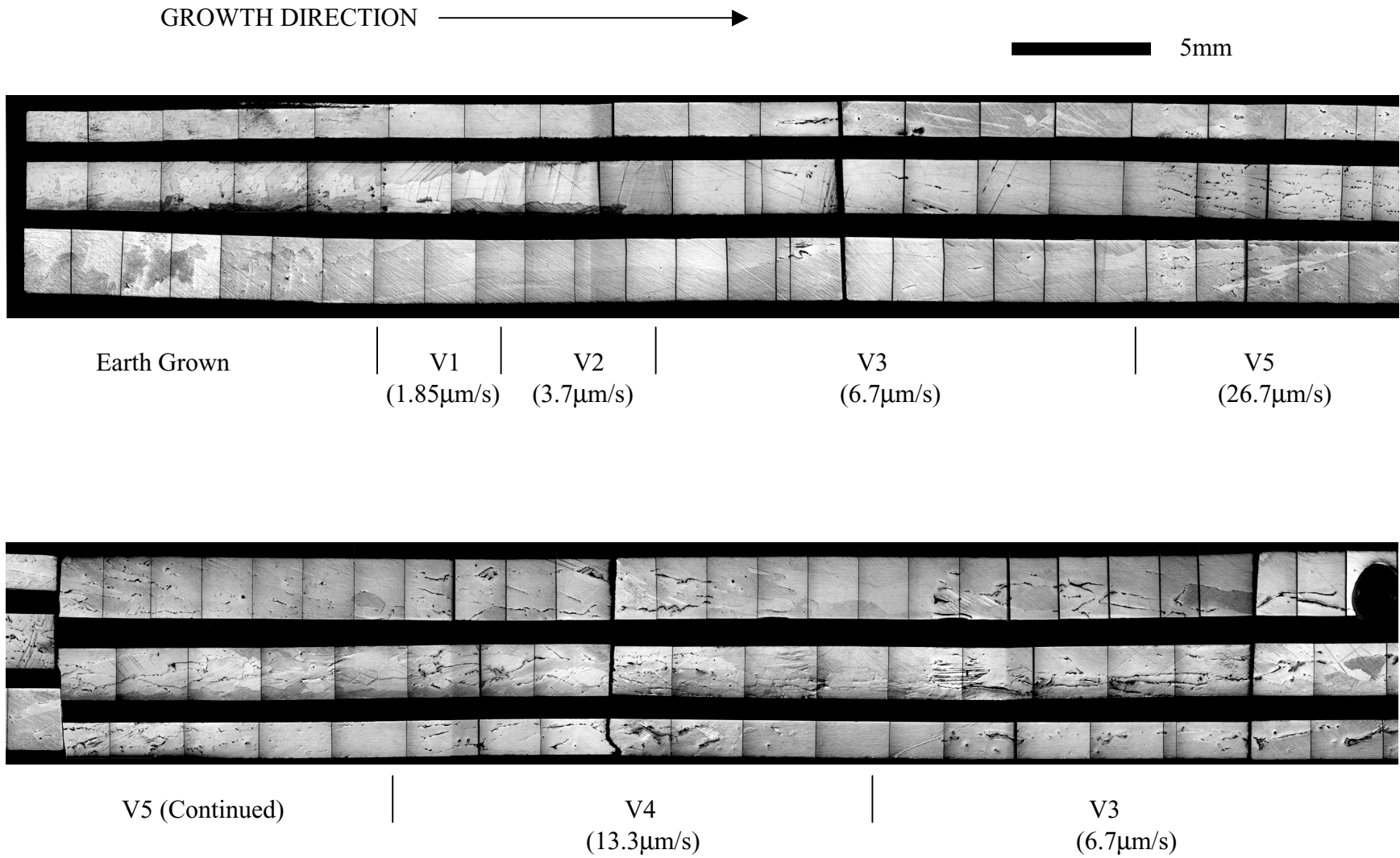


Figure 8(a). Microstructural evolution of the Seebeck sample from the earth grown material to growth in the capillary section.

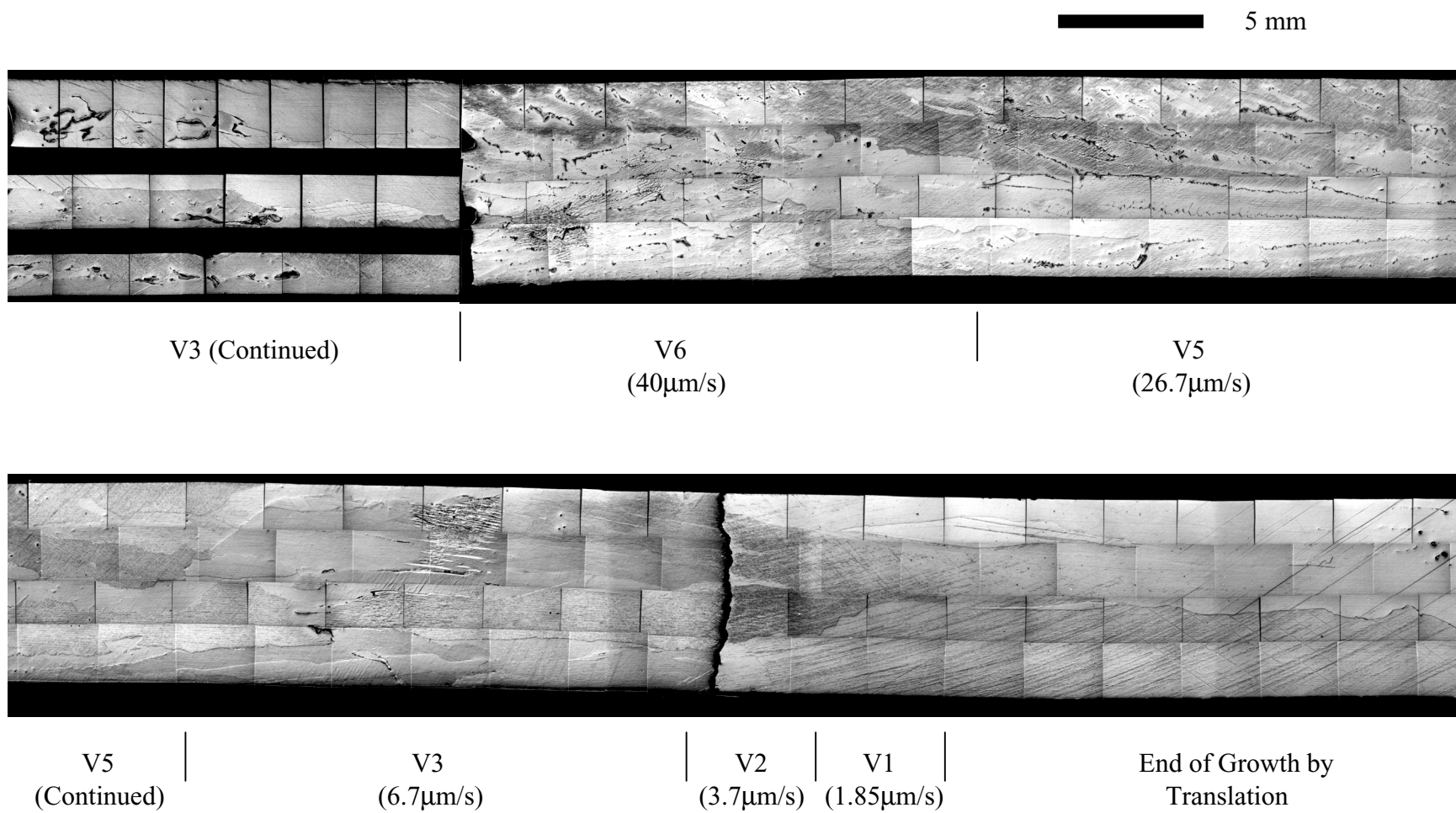


Figure 8(b). Continued microstructure of the Seebeck sample extending into the section outside the capillary and finishing in the region where translation finished.

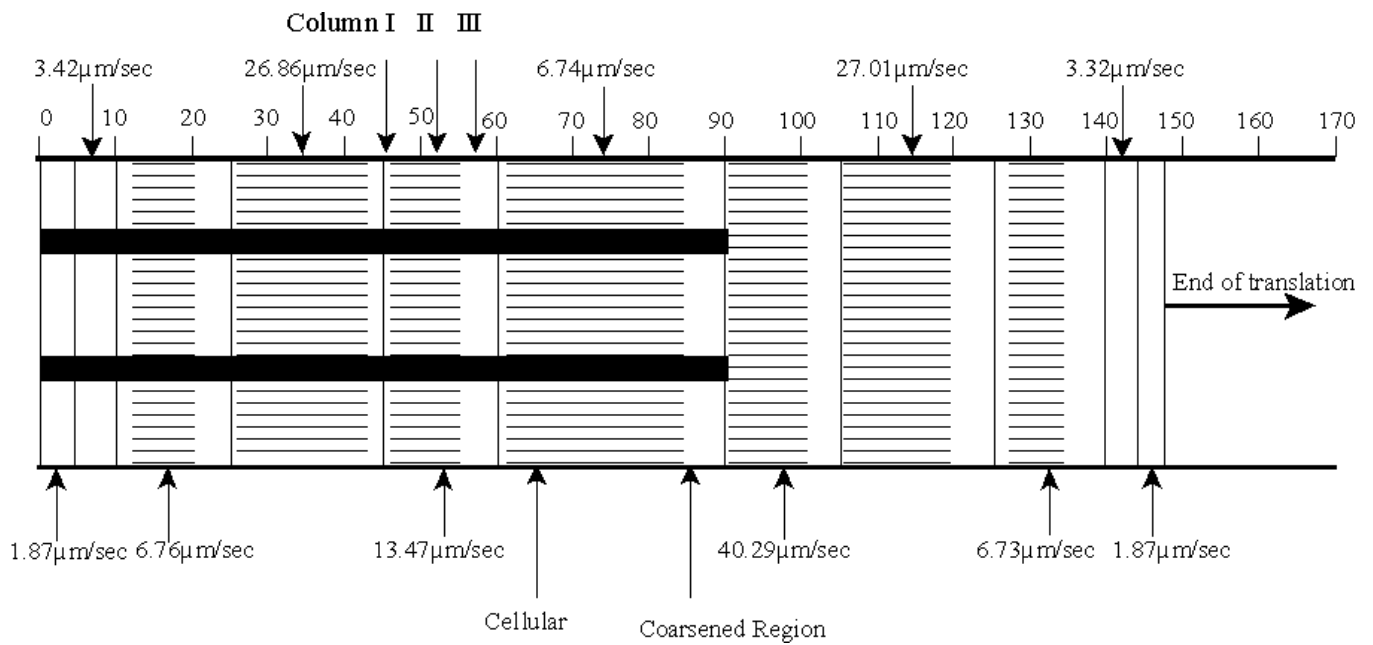
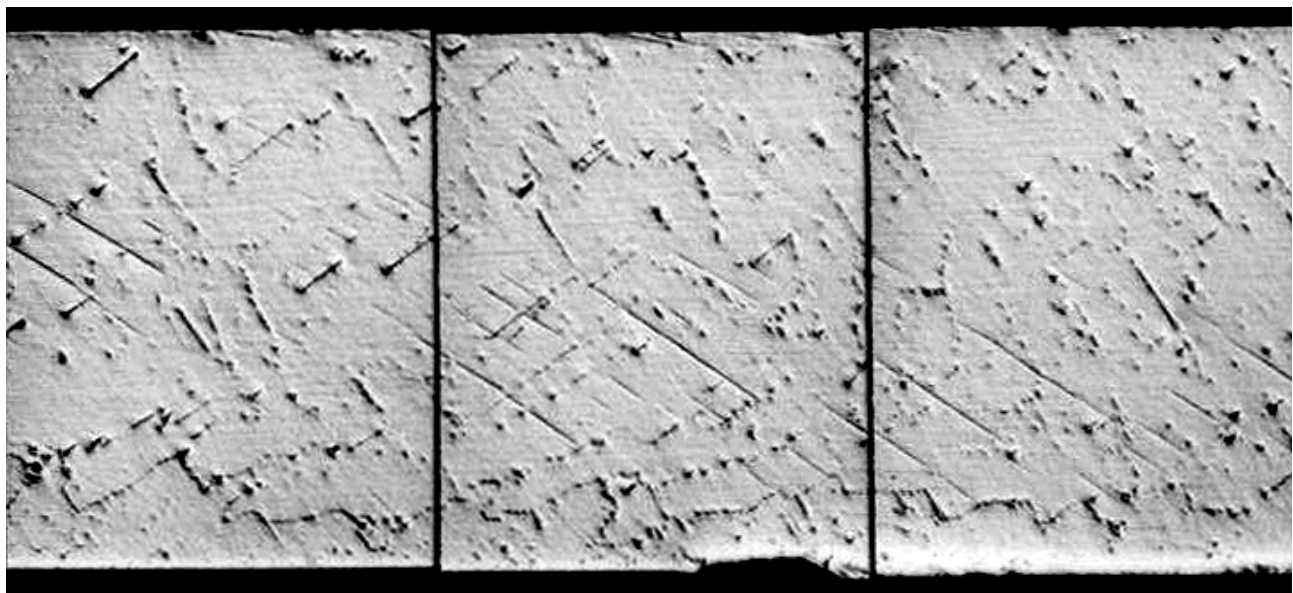


Figure 9. Summary of sample sections preserved during final solidification. Sections with horizontal lines indicate cellular breakdown.



0.5mm

Figure 10. Detail of Earth-grown section showing a faceted cellular/dendritic structure.

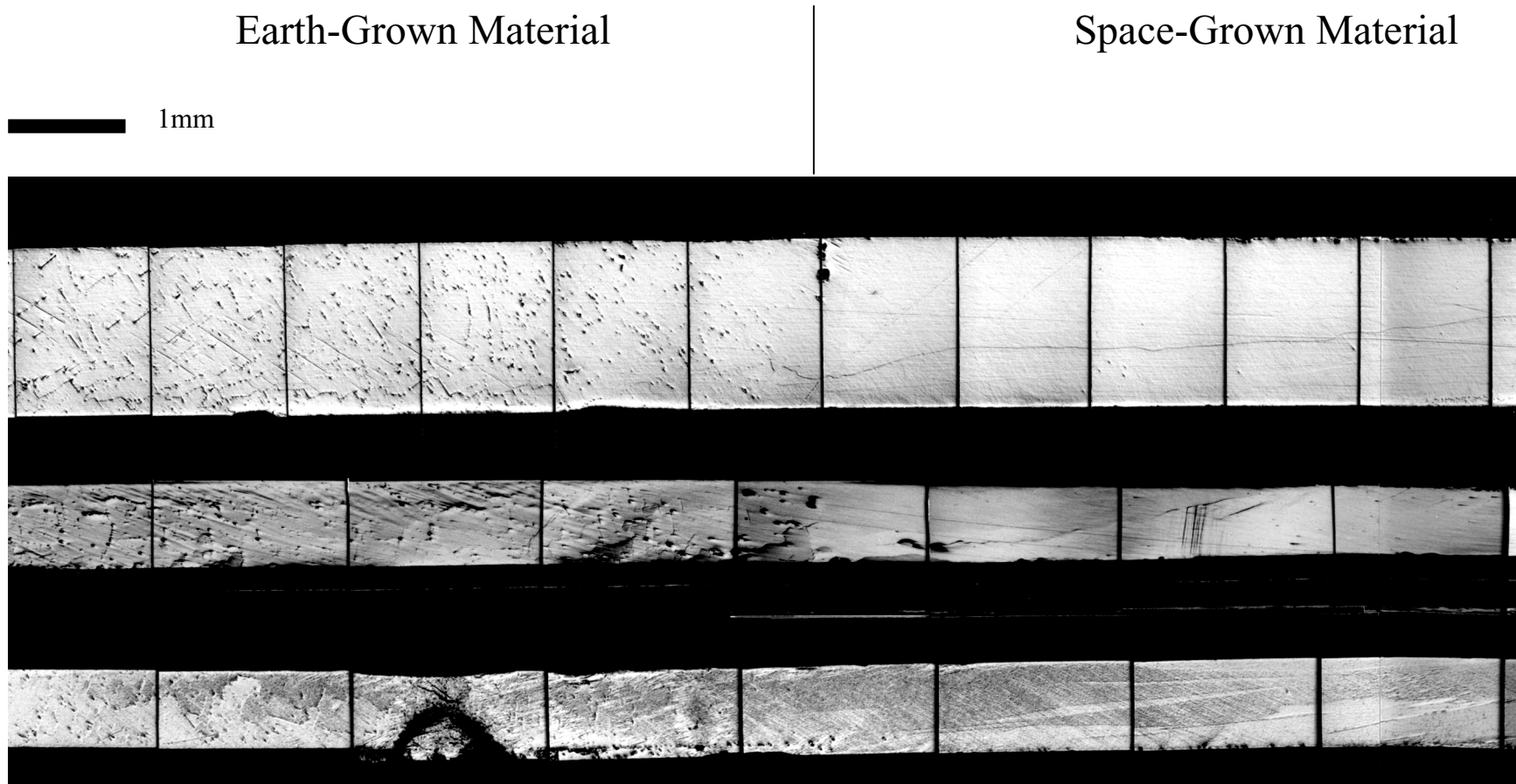


Figure 11(a). Composite image of the initial growth of the quench sample. The initial Earth-grown structure on the left hand side shows a faceted cellular dendritic morphology. The transition to plane-front growth is visible in the space-grown material on the right hand side.

Earth-Grown Material

Space-Grown Material

1mm

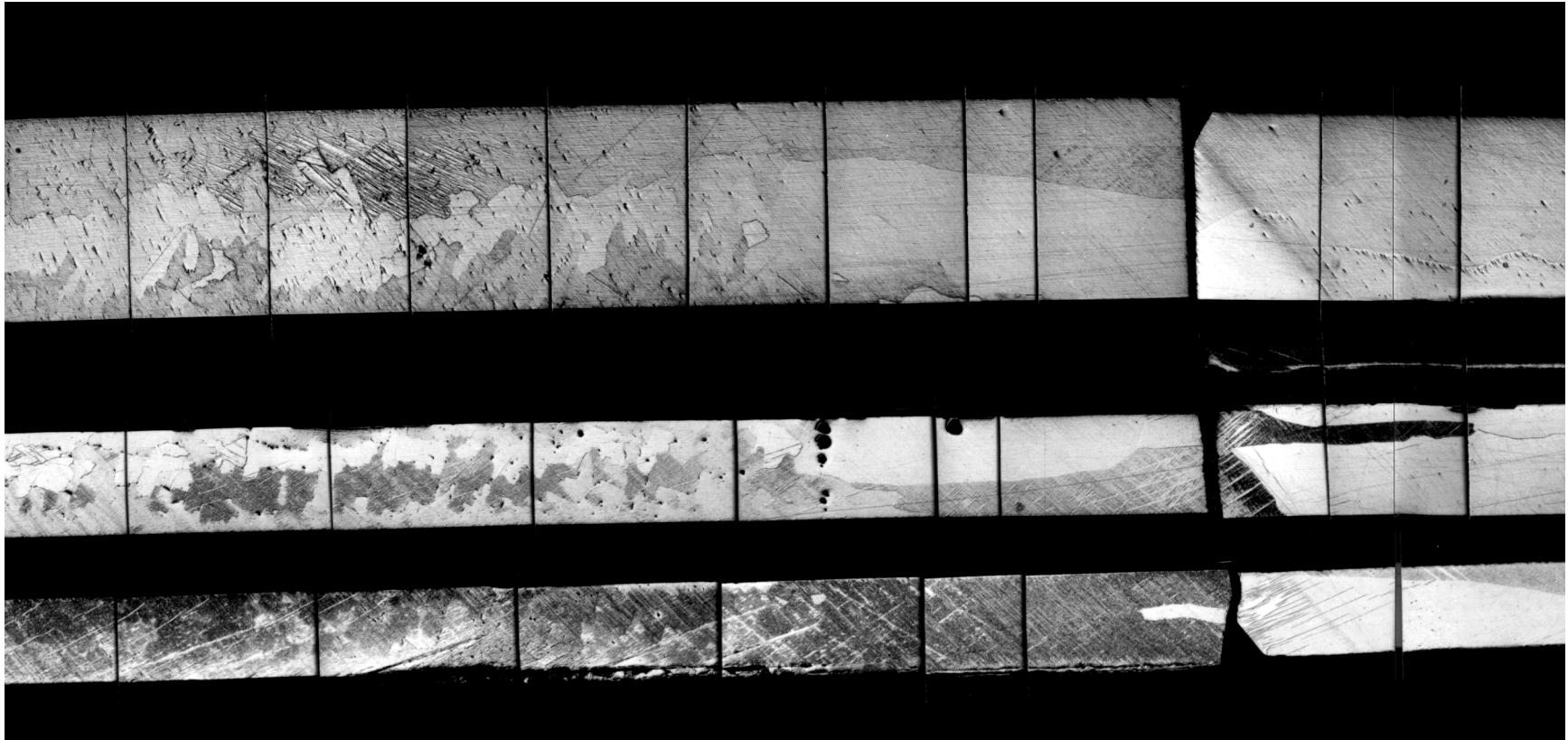


Figure 11(b). Composite image of the initial growth of the Peltier sample showing a similar structure to the quench sample. The break in the micrograph is where the sample was cross sectioned.

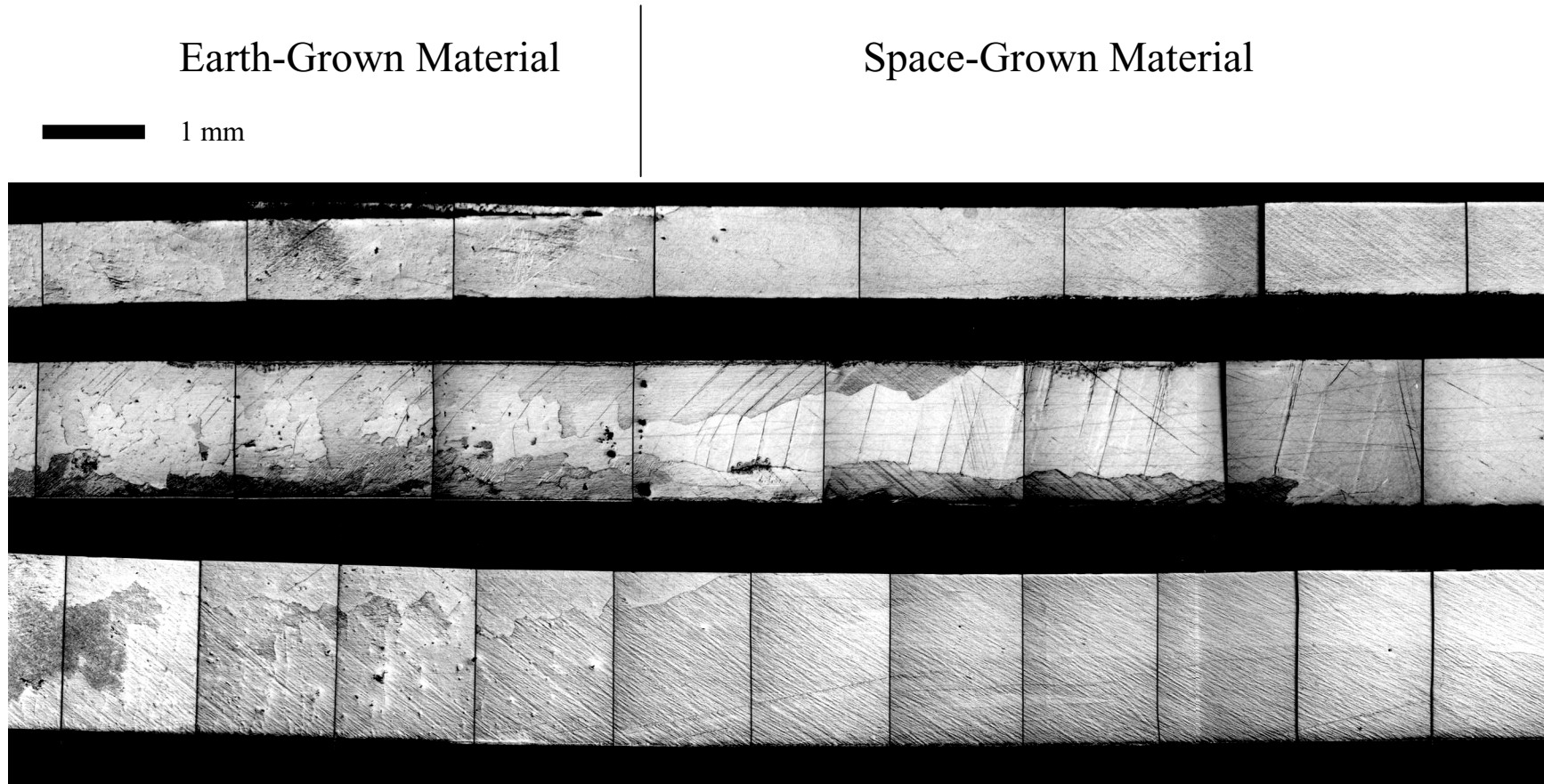
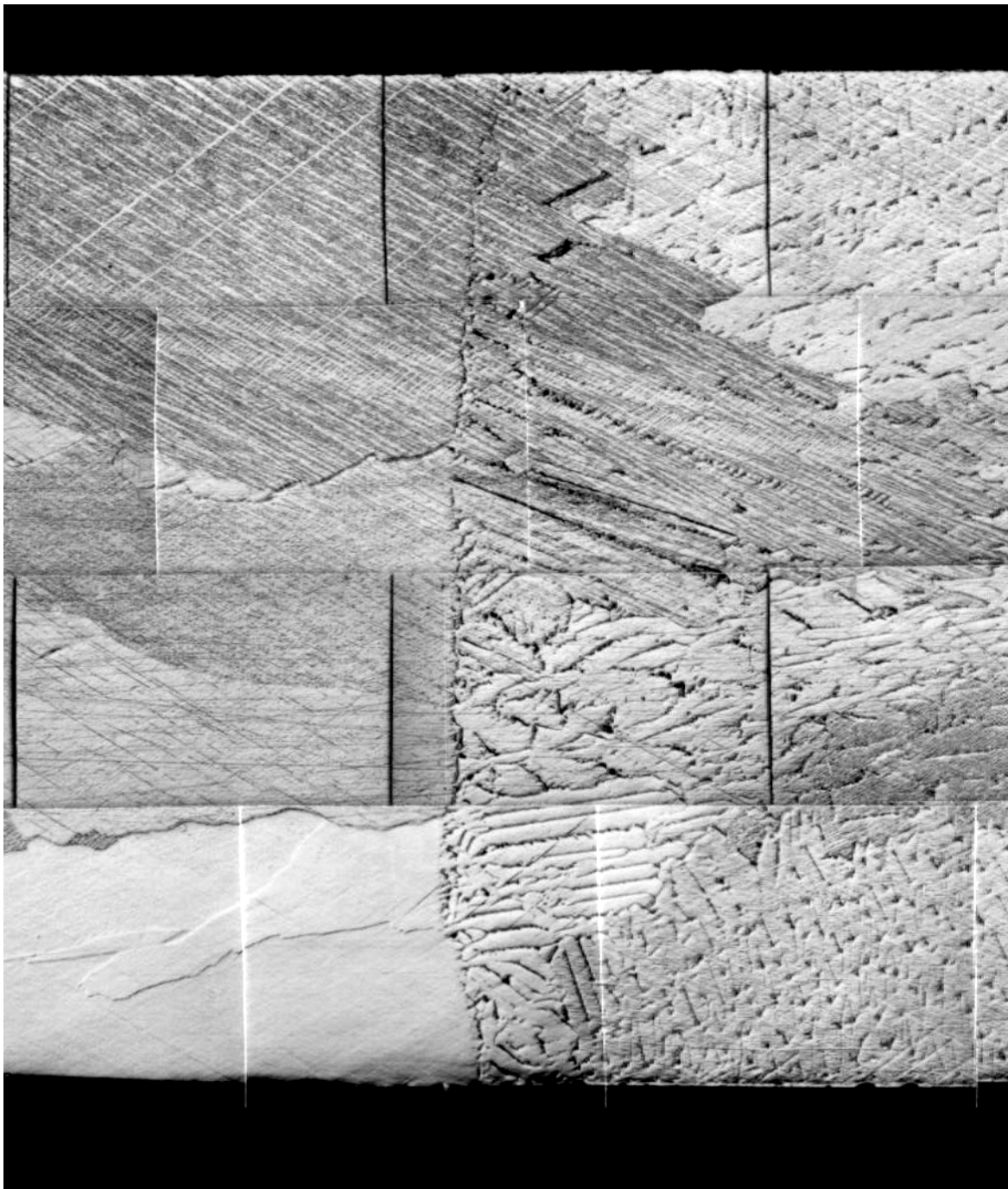


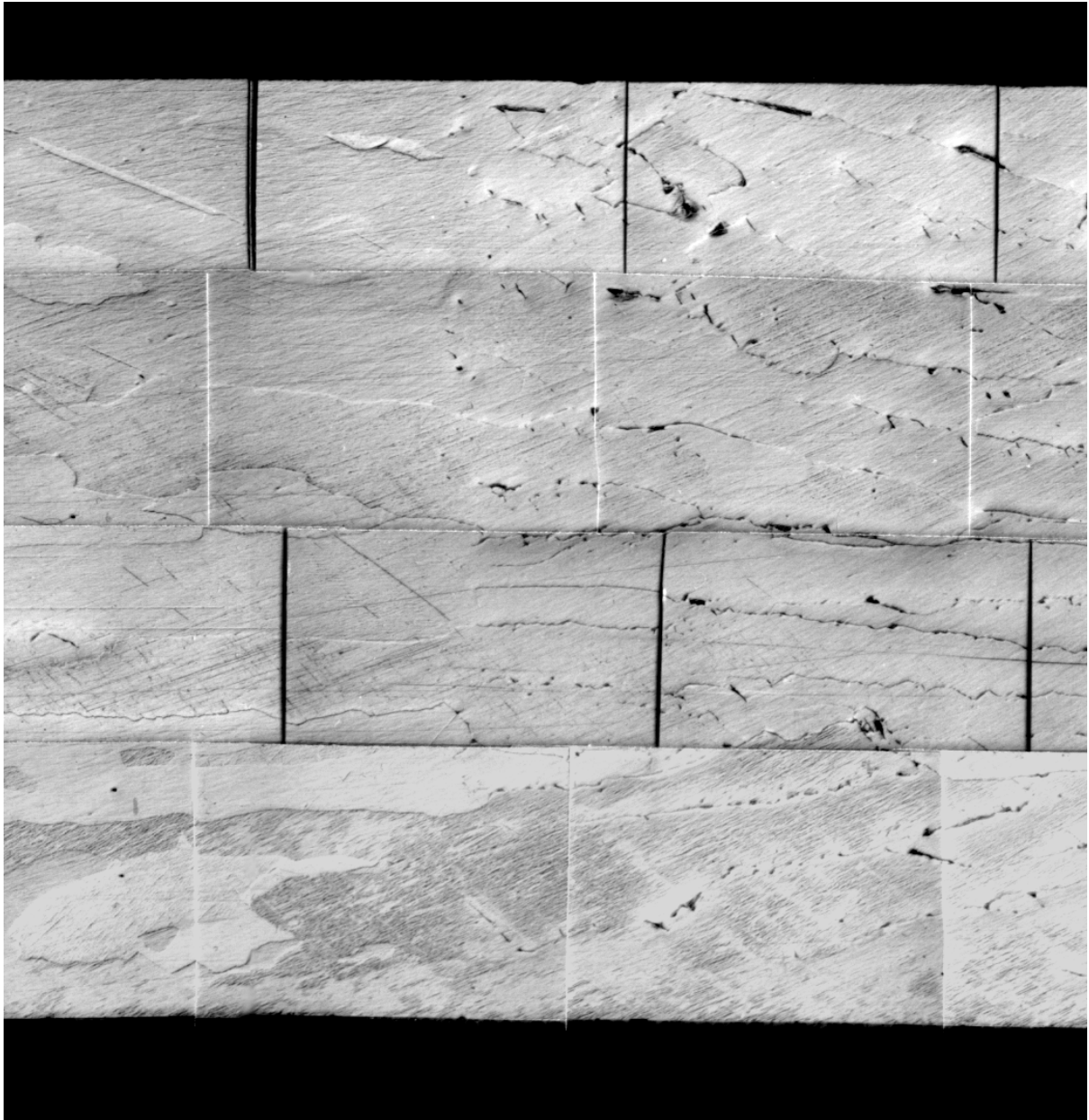
Figure 11(c). Composite image of the initial growth of the Seebeck sample showing a similar structure to the previous samples. Twins are visible in the capillary section.



1 mm

Figure 12. Composite micrograph of quenched section of the quench sample showing the S/L interface shape.

1 mm



Start of
run

Cellular Breakdown at 26.7 μ m/s

Figure 13. Detail of Peltier sample showing a V5 breakdown outside of the capillary region.

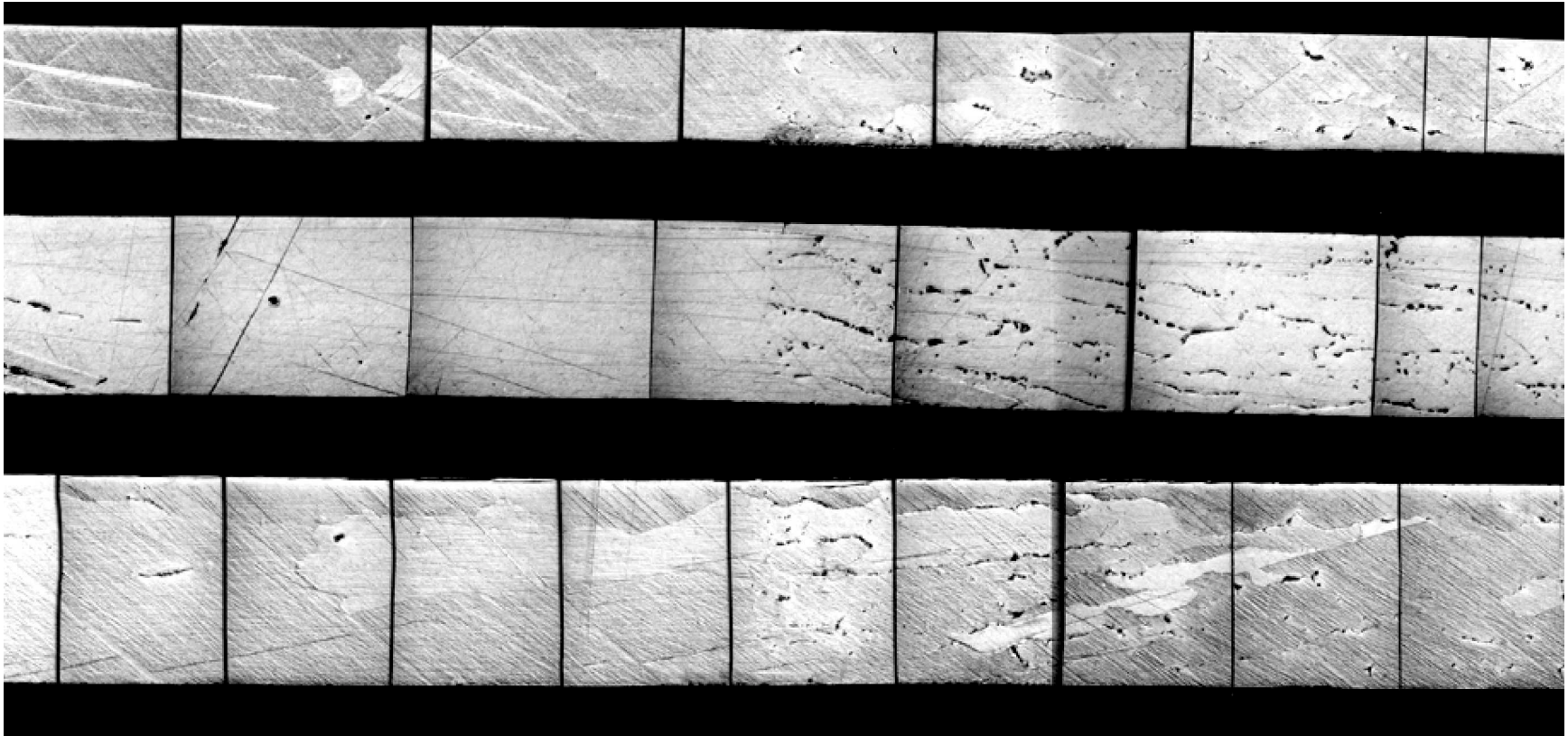


Figure 14. Morphological instability in the Seebeck sample under growth velocity V4.

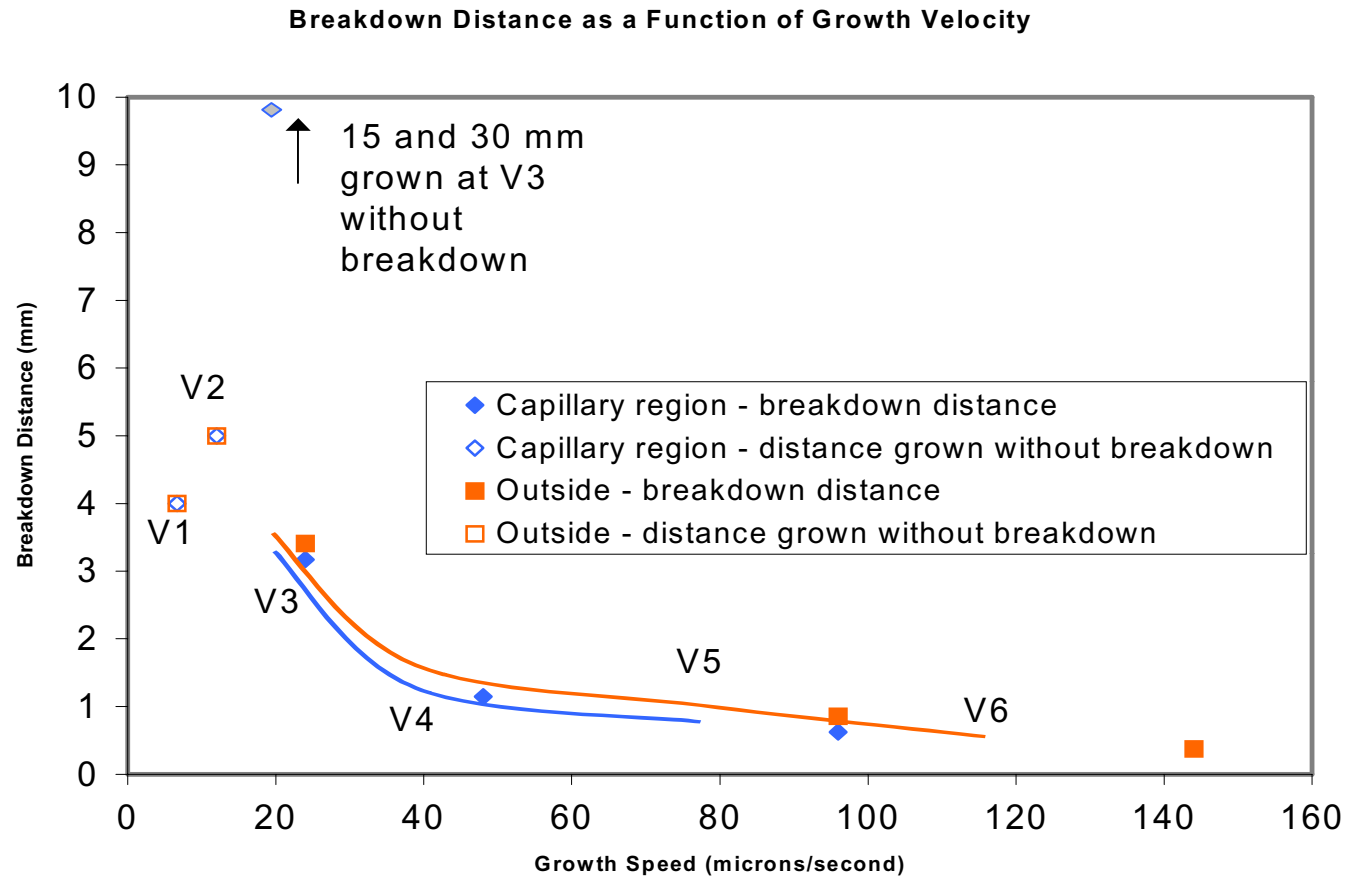


Figure 15. Breakdown distance as a function of growth velocity; solid symbols are the distances solidified to the planar to cellular transition, open symbols indicate planar front growth distances without the planar to cellular transition being reached.

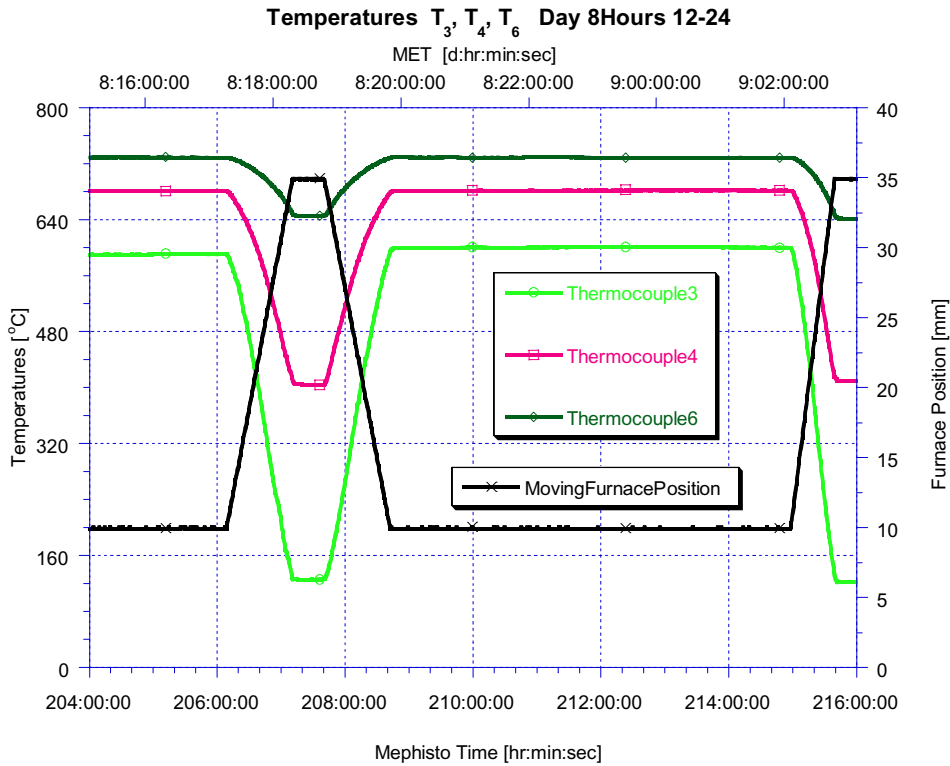


Figure 16. Thermal measurement by three thermocouples placed in the Peltier and Quenching samples.

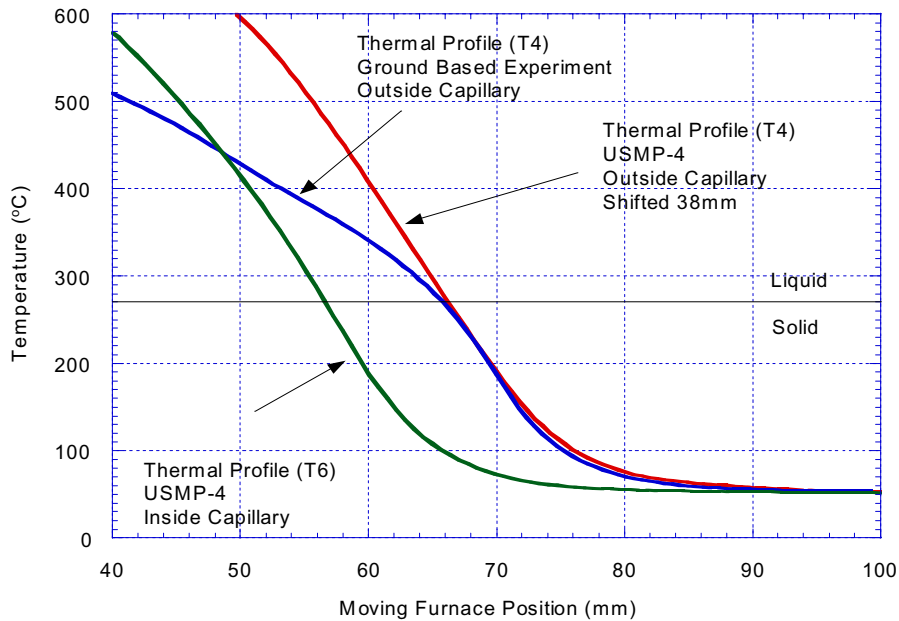


Figure 17. MEPHISTO thermal profile for ground and space based mission. Above the melting point of the liquid the temperature gradient for the ground-based experiments is significantly lower indicating convection. The profile is very similar inside and outside capillary on space-based experiments.

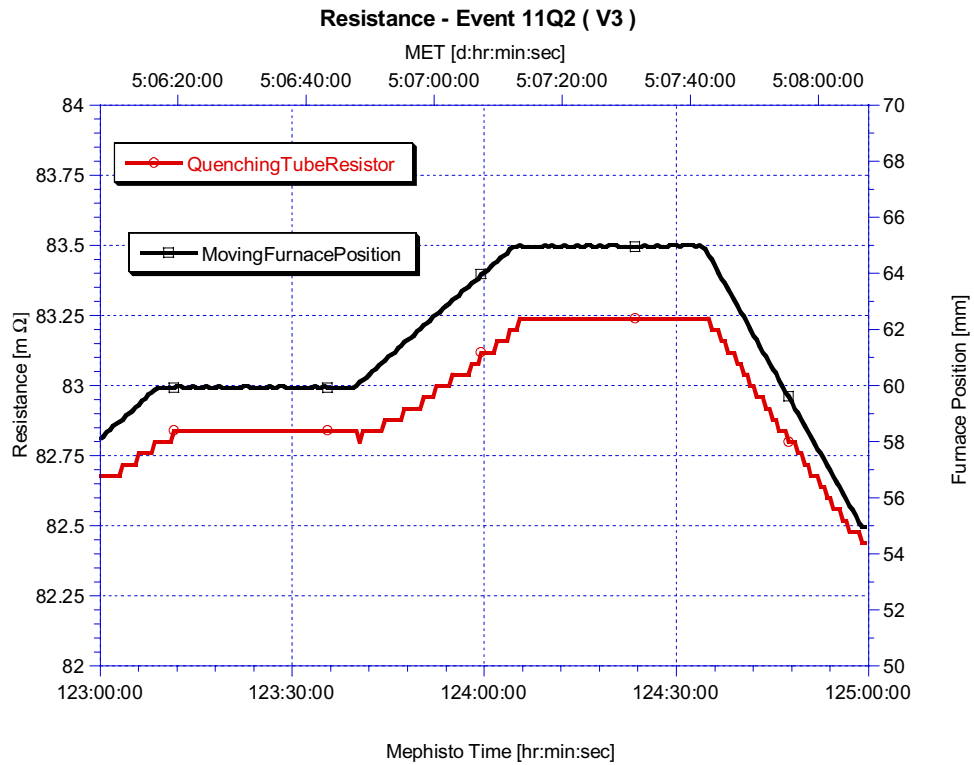


Figure 18. Resistance and furnace position change as a function of processing time during event 11Q2 in MEPHISTO experiment.

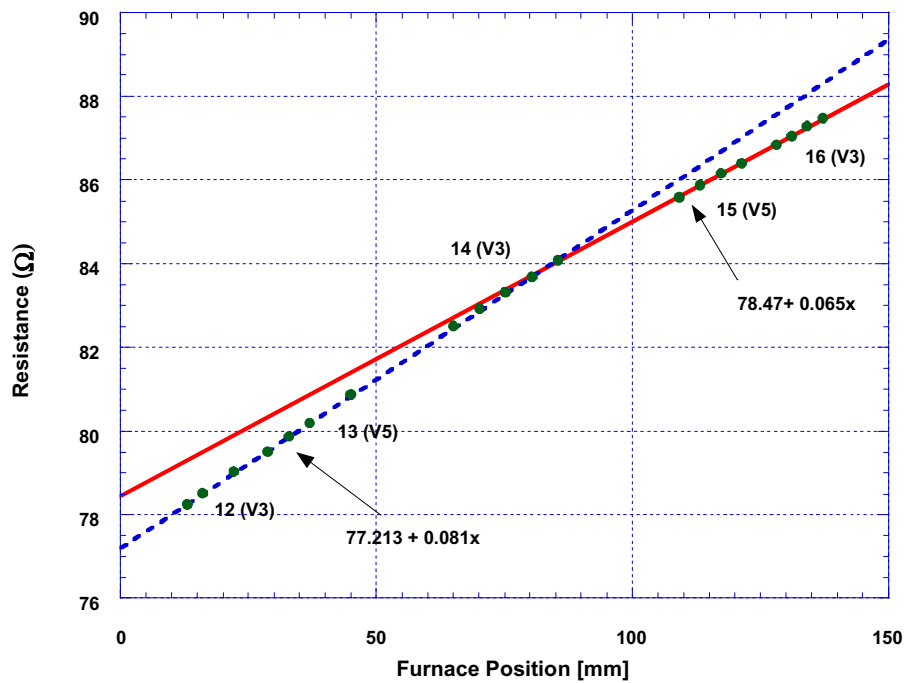


Figure 19. Resistance of Sample versus furnace Position. Crossing of lines is evidence of the end of capillary. Dashed line fits data in the capillary, solid line is fits of data outside.

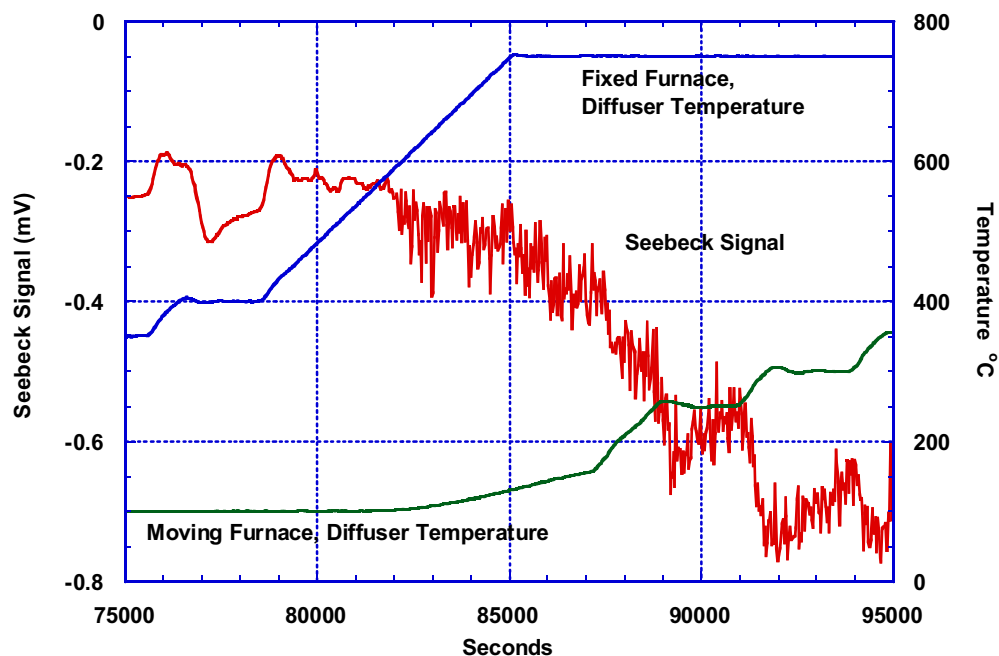


Figure 20. Diffuser temperatures for MEPHISTO furnaces and Seebeck signal during heat-up for ground-based experiments. Fluctuations in the Seebeck signal become apparent as the temperature of the liquid is increased from 400°C to 750°C.

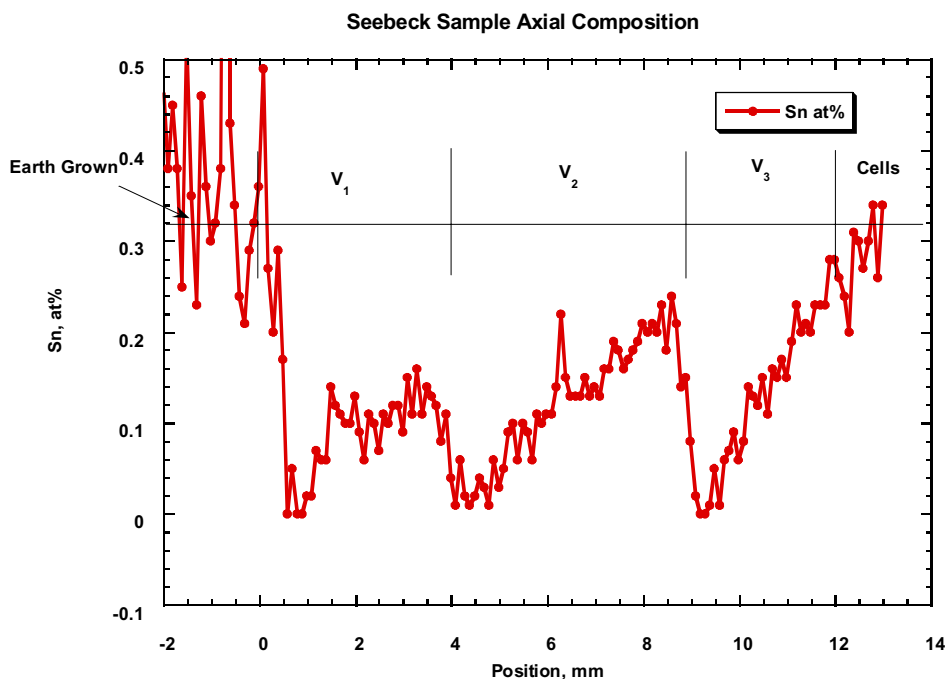


Figure 21. The microprobe compositional line scan for the Seebeck sample during events 11A, 11B, 12, which includes three velocities V1, V2, V3.

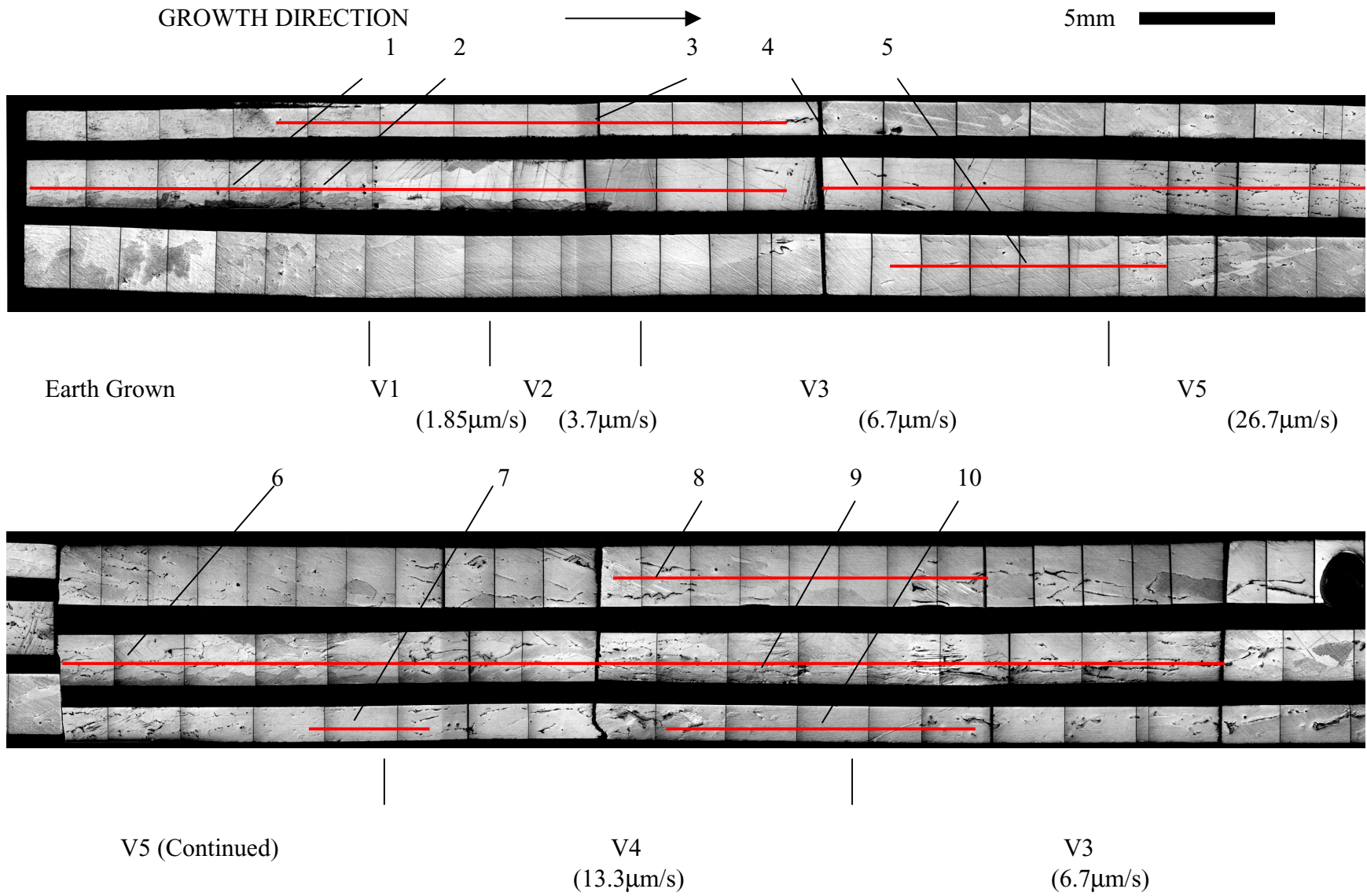


Figure 22(a). Schematic of microprobe analysis position on the Seebeck sample, line numbers included.

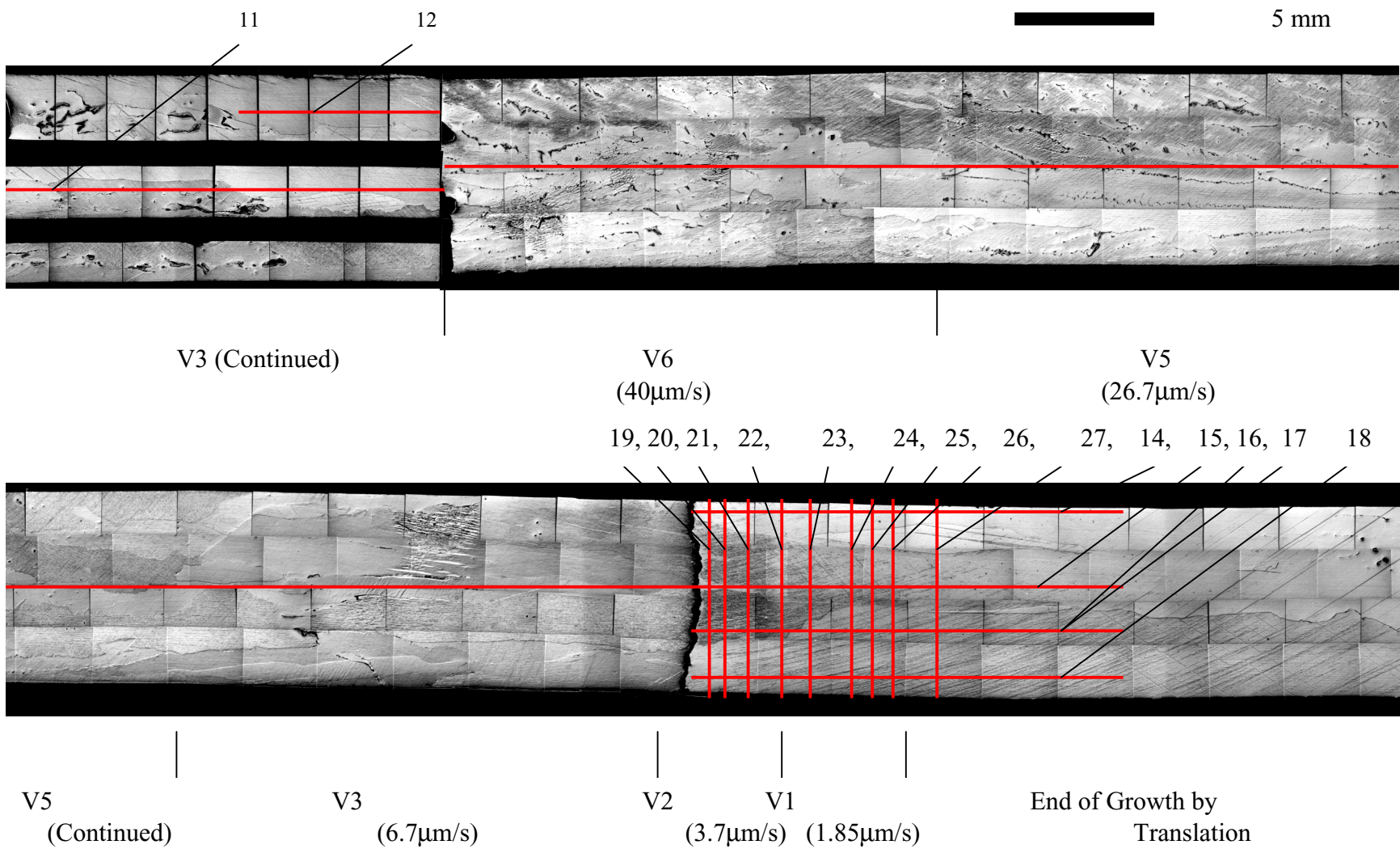


Figure 22(b). Schematic of microprobe analysis position on the Seebeck sample, line numbers included.

Seebeck Sample Radial Composition

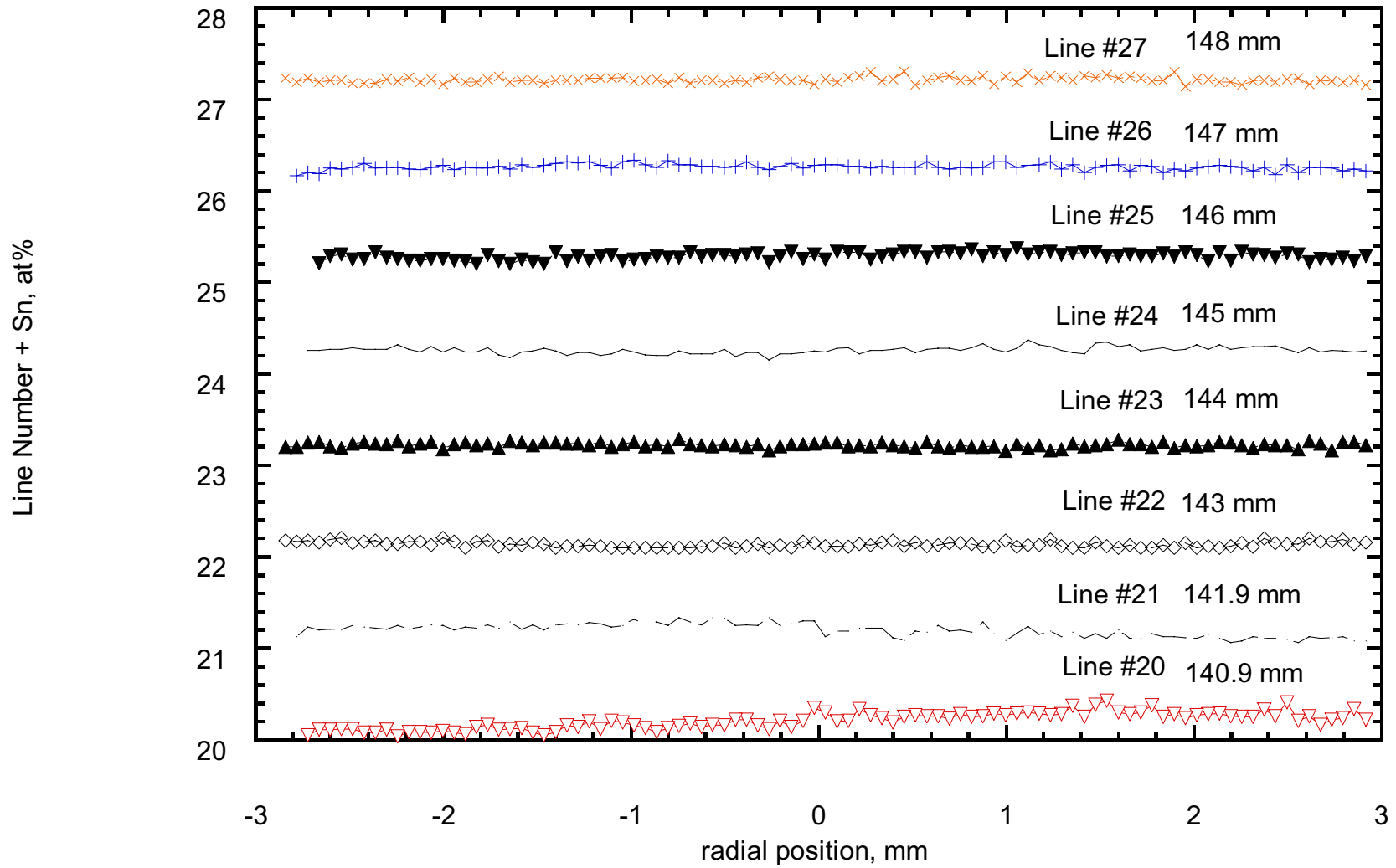


Figure 23. Radial composition profile in the Seebeck sample during solidification at velocity V1, V2.

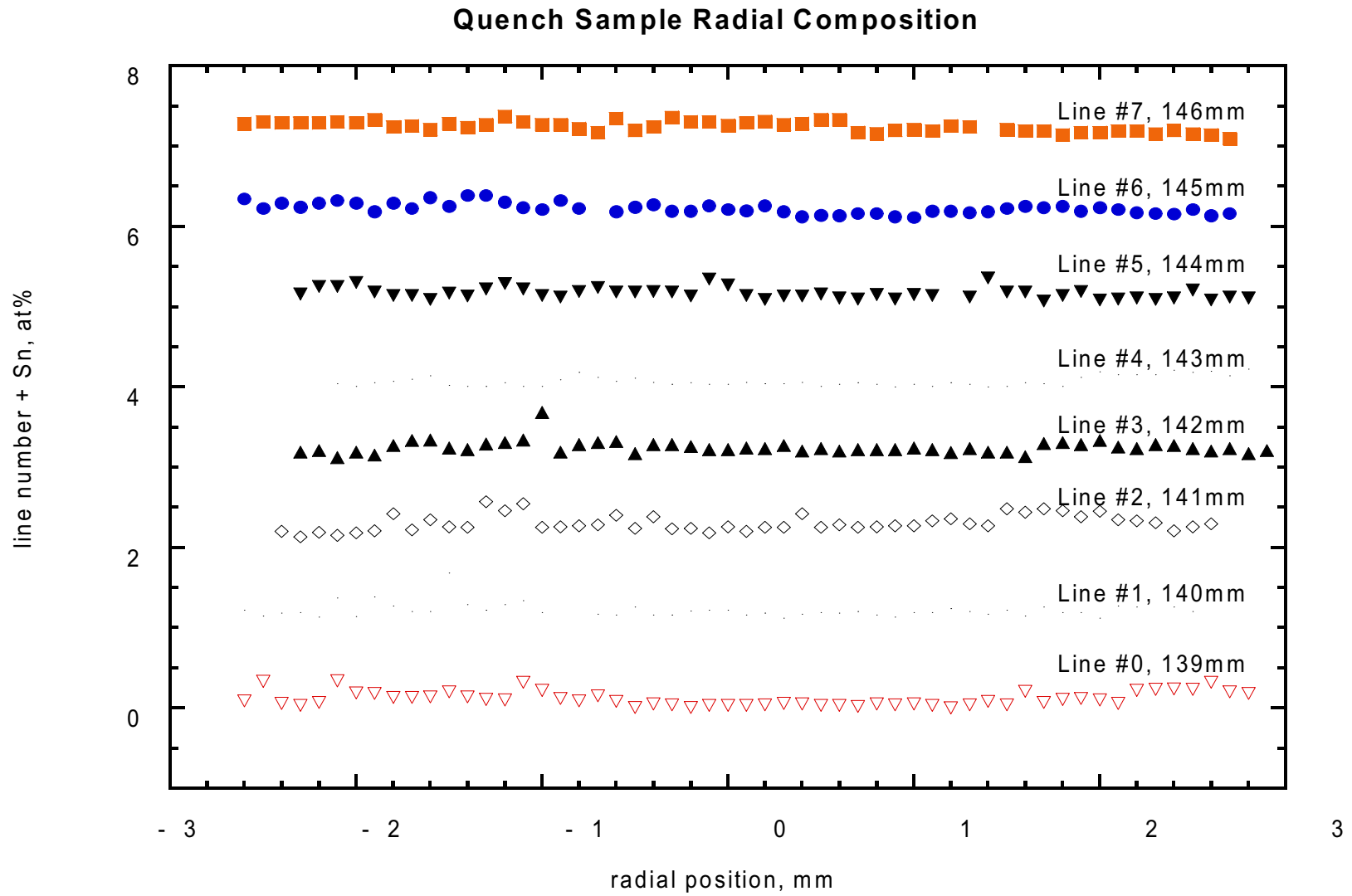


Figure 24. Radial composition profile in the Quench sample during solidification at velocity V1 and V2.

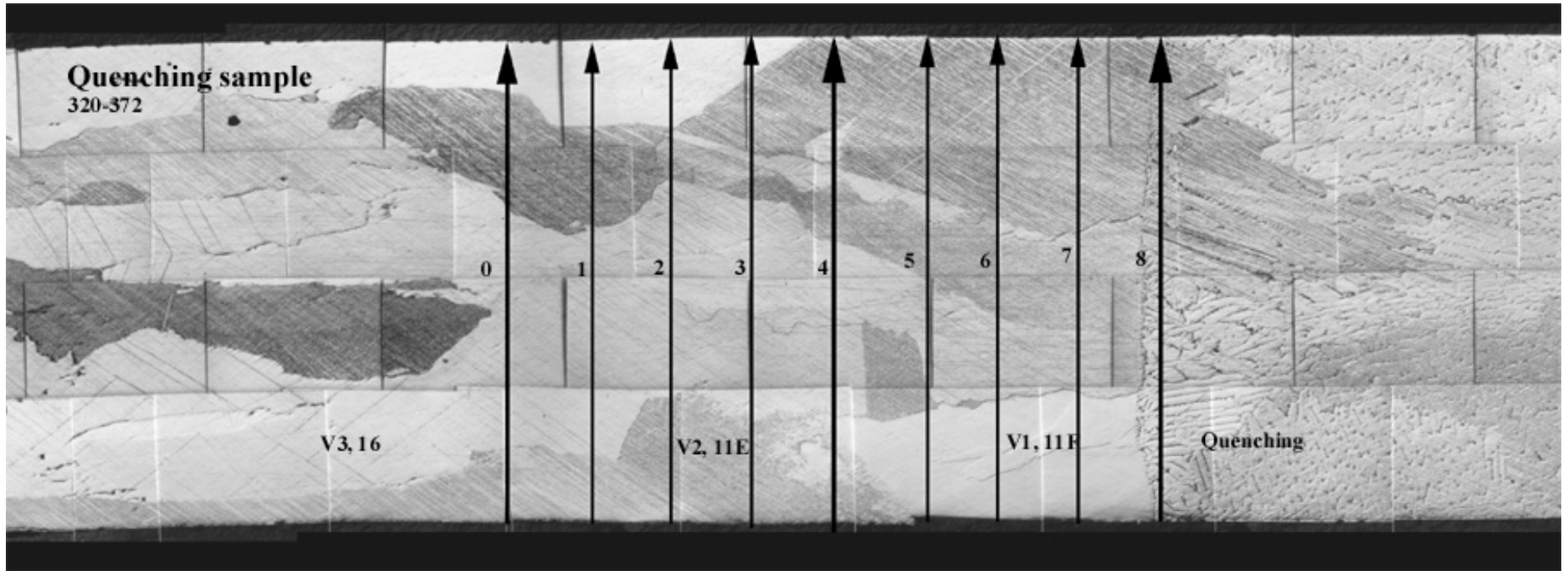


Figure 25. Microprobe analysis position on the quench sample, line numbers represent location of the compositional plots given in figure 24.

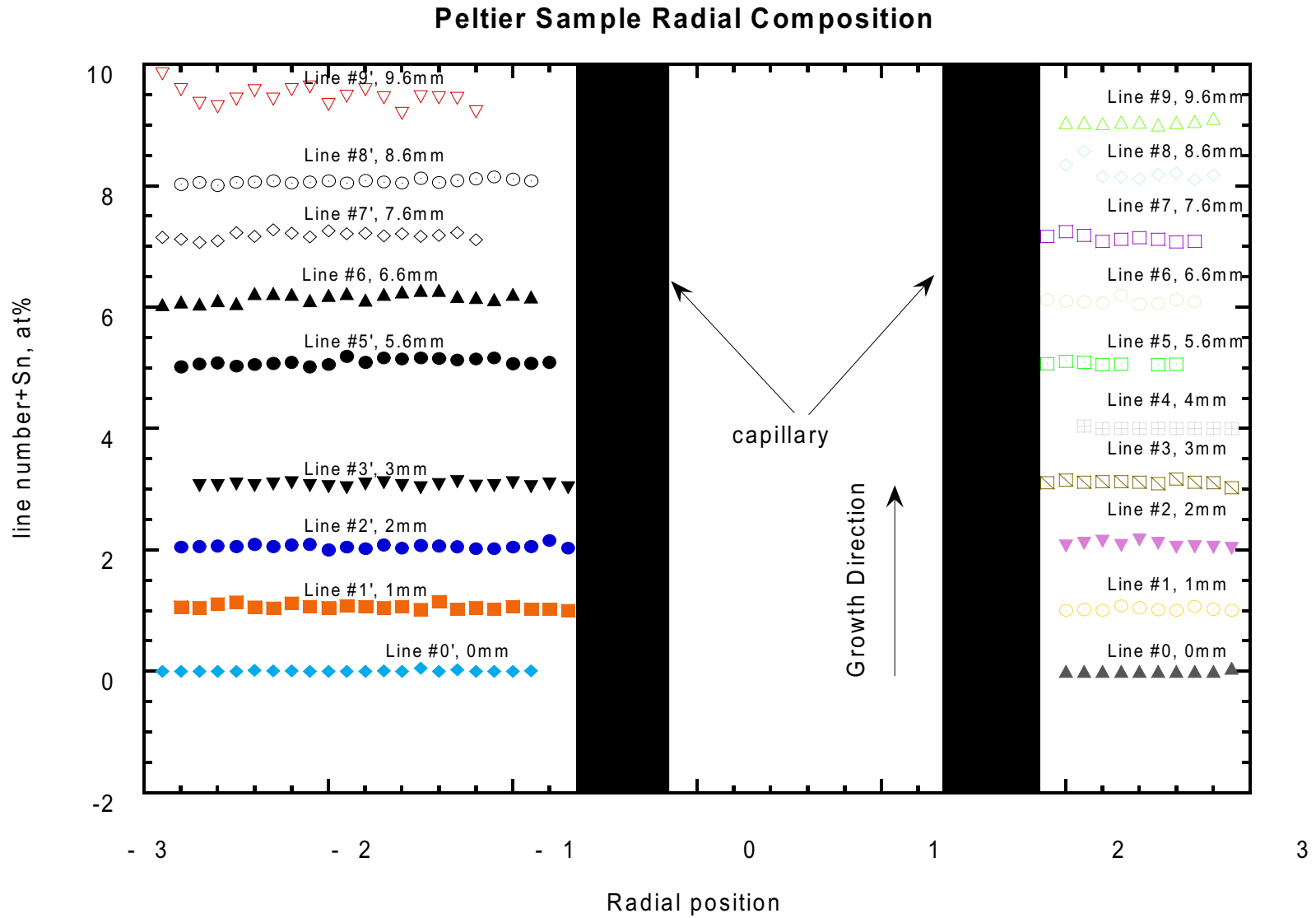


Figure 26. Radial composition profile outside the capillary tube in the Peltier sample during solidification at velocity V1 and V2.

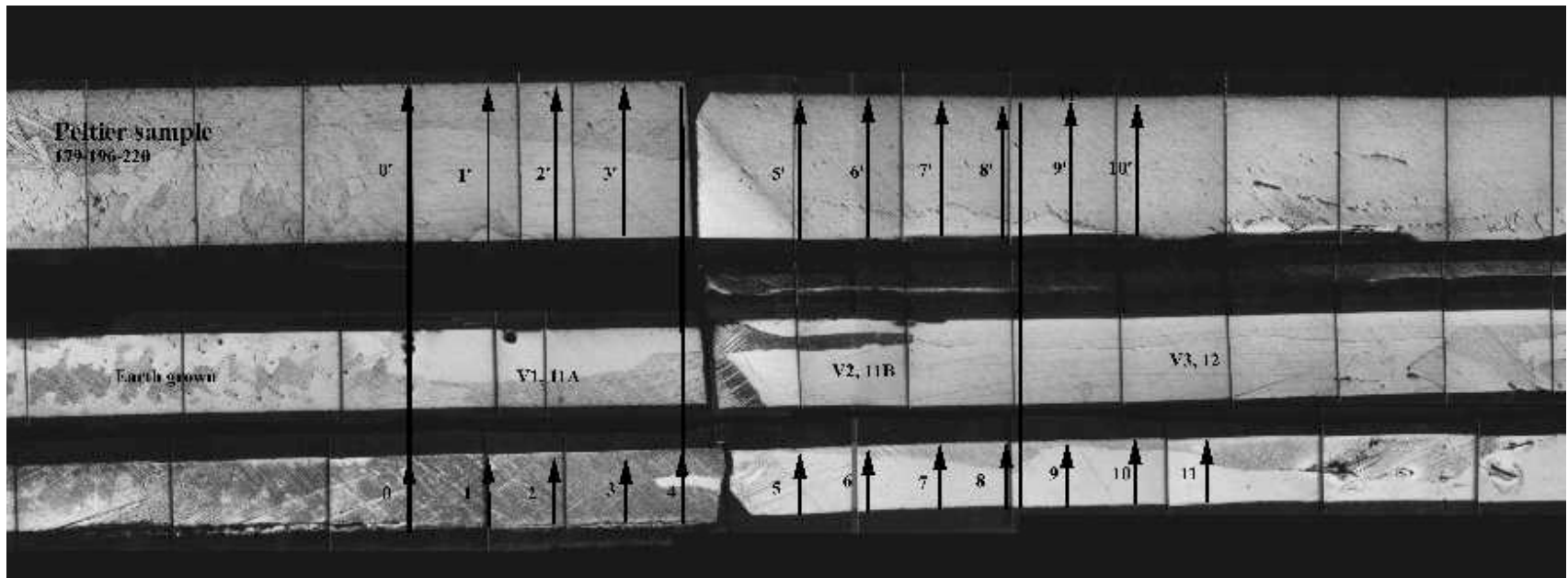


Figure 27. Microprobe analysis position on the peltier sample, line numbers are shown.

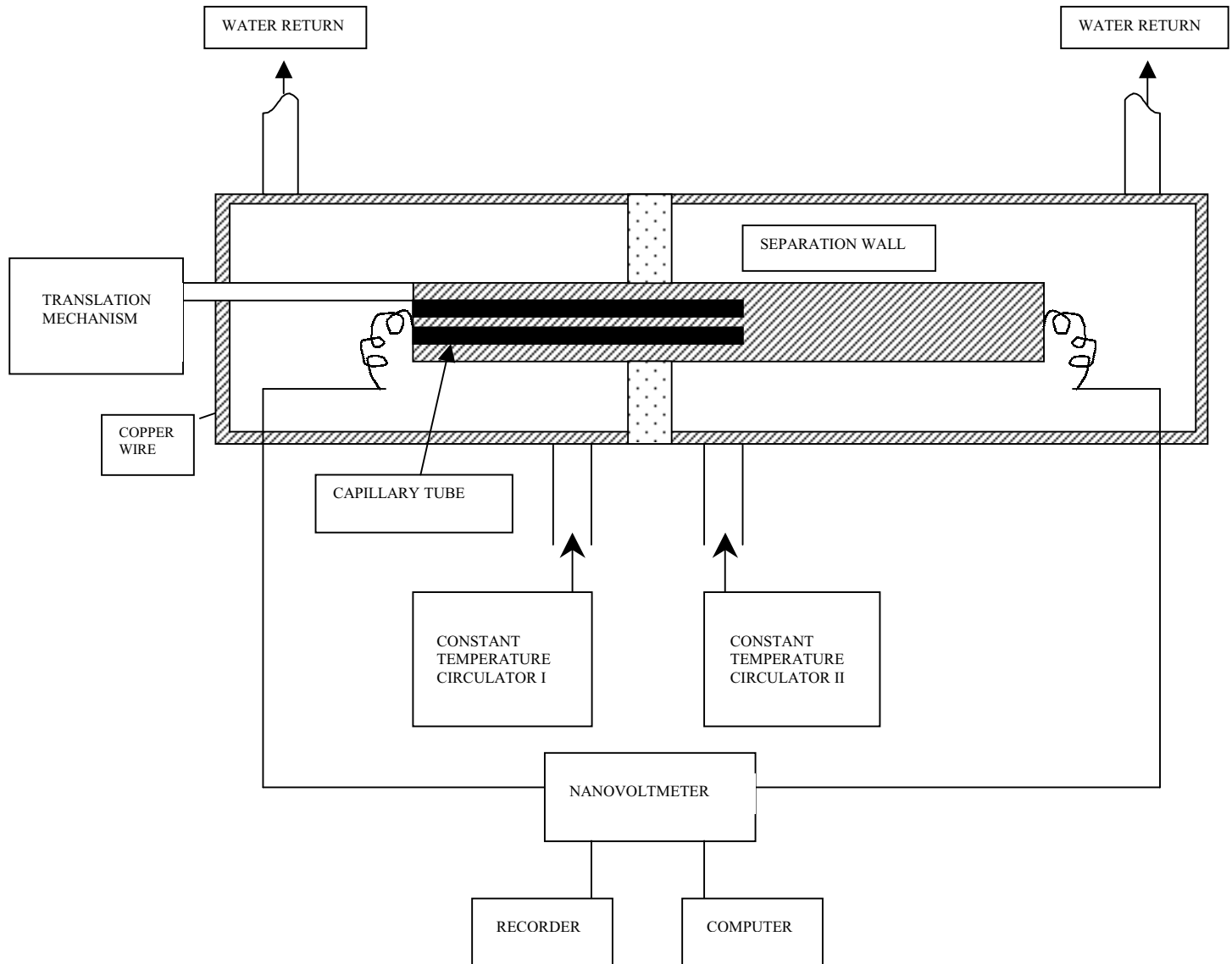


Figure 28. Schematic of Structural Seebeck Measurements.

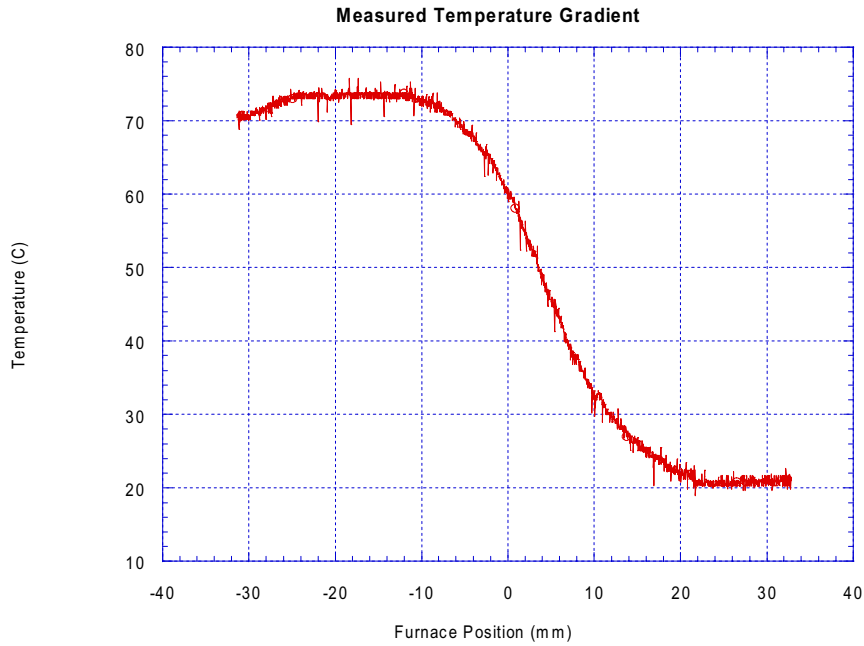


Figure 29. Temperature gradient in the sample for structural Seebeck determination, with the cold and hot ends at 20 and 75°C, respectively.

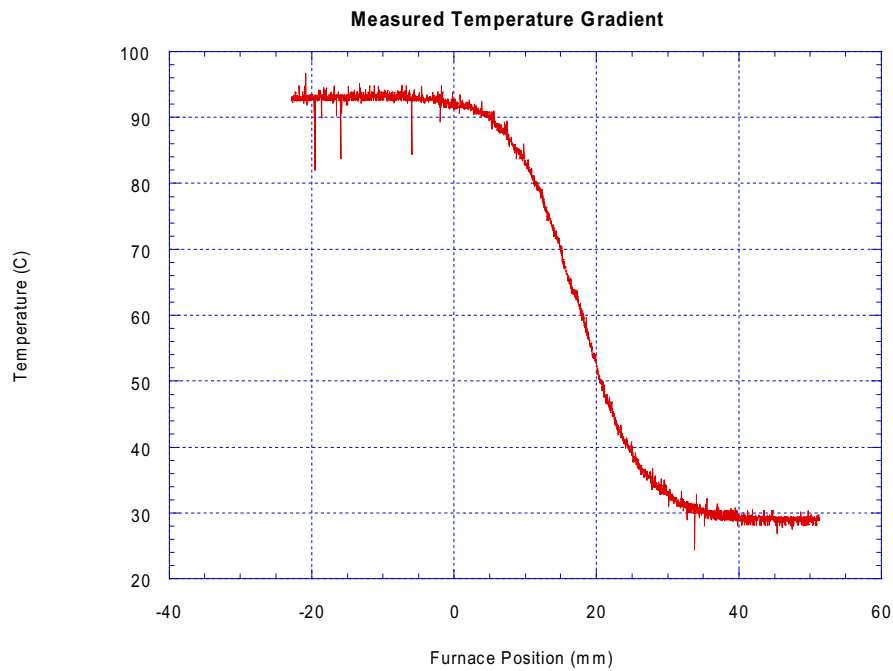


Figure 30. Temperature gradient in the sample for the structural Seebeck determination. The cold end is at 20°C with the hot end at 95°C.

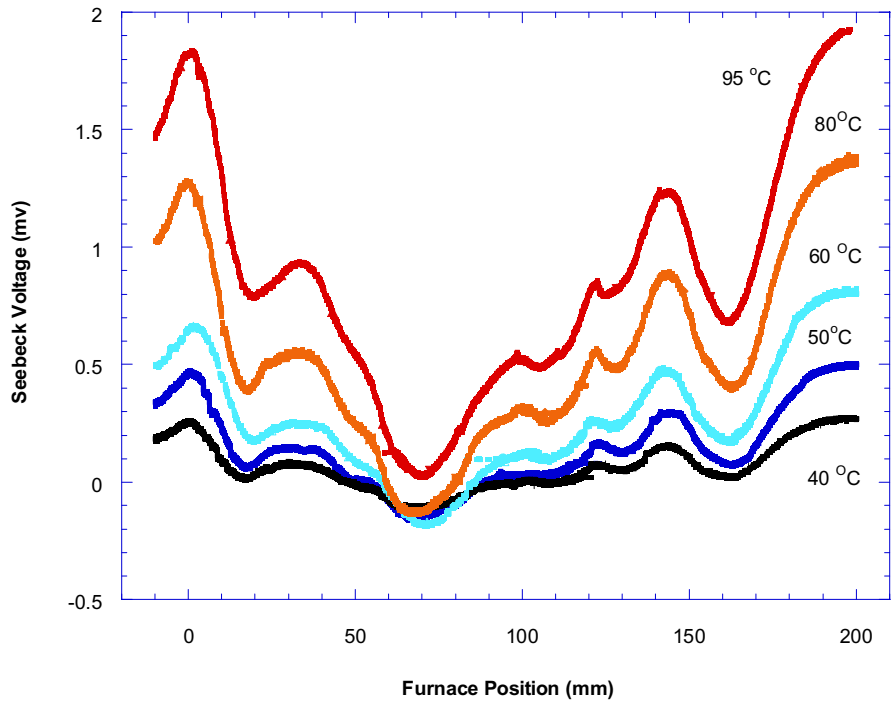


Figure 31. Structural Seebeck voltage under different temperatures, with the cold zone at 20°C and hot zone as indicated.

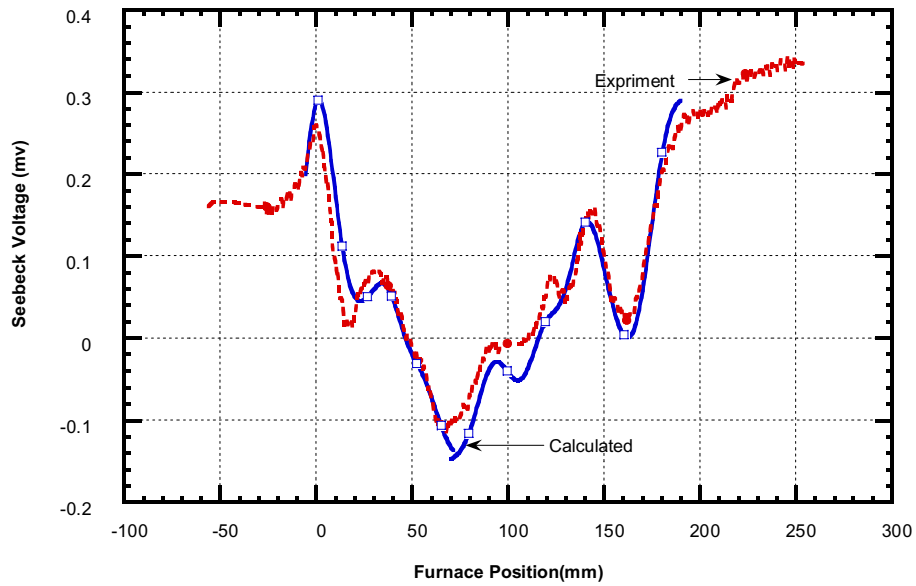


Figure 32. Calculated structural Seebeck voltage compared with experimental data for hot zone at 40°C.

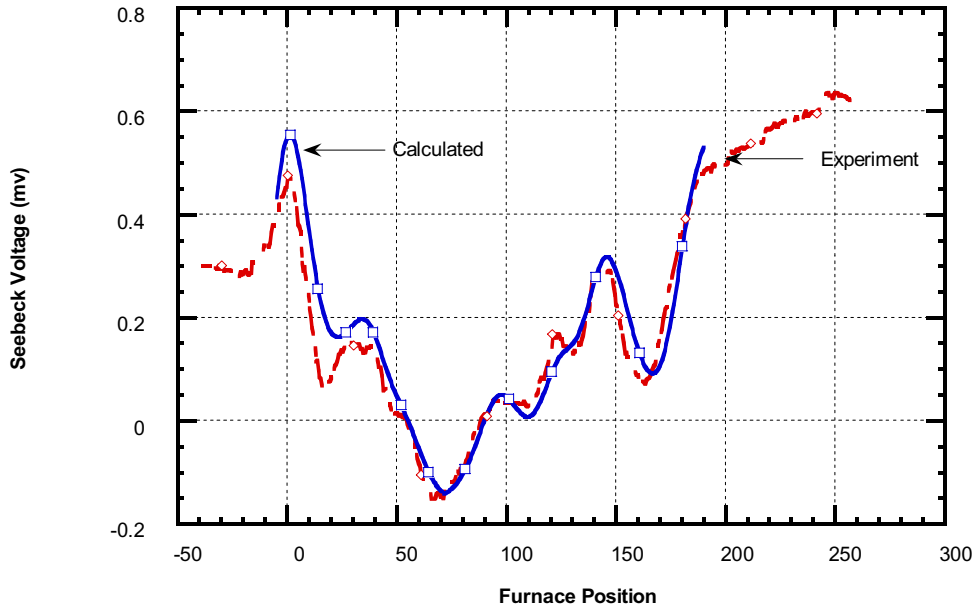


Figure 33. Calculated structural Seebeck voltage compared with the experimental data for hot zone under 50°C.

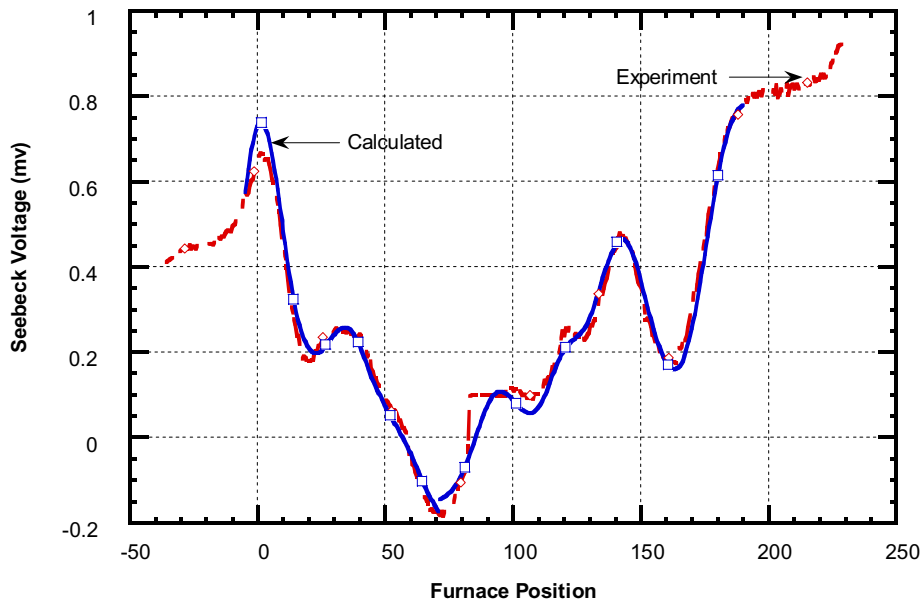


Figure 34. Calculated structural Seebeck voltage compared with experimental data for hot zone at 60°C.

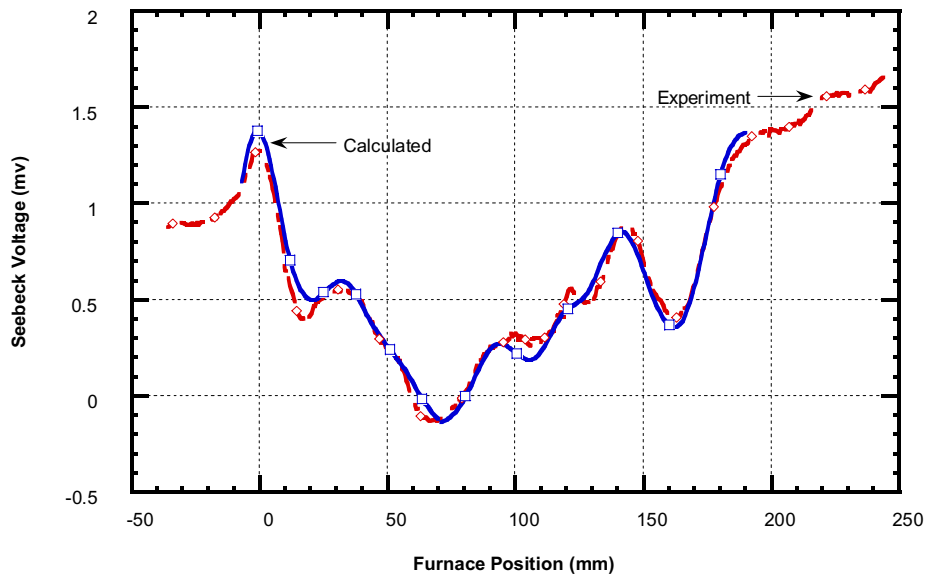


Figure 35. Calculated structural Seebeck voltage compared with experimental data for hot zone at 85°C.

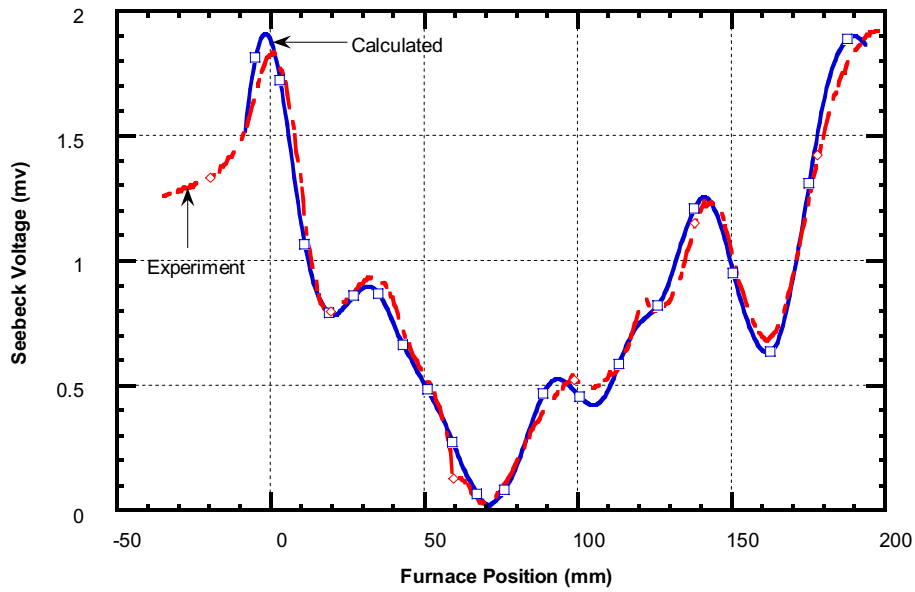
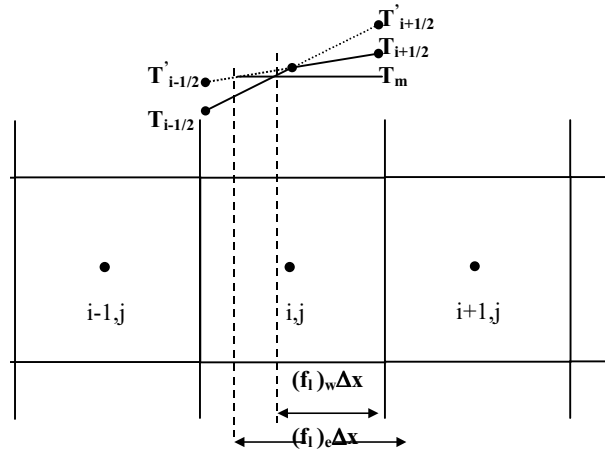


Figure 36. Calculated Structural Seebeck voltage compared with experimental data for hot zone at 95°C.



$$T_{i-1/2} = 0.5 * (T_i + T_{i-j})$$

$$T_{i+1/2} = 0.5 * (T_i + T_{i+1})$$

Figure 37. Calculation of liquid fraction from temperature slopes in liquid and solid (subscripts j omitted for clarity).

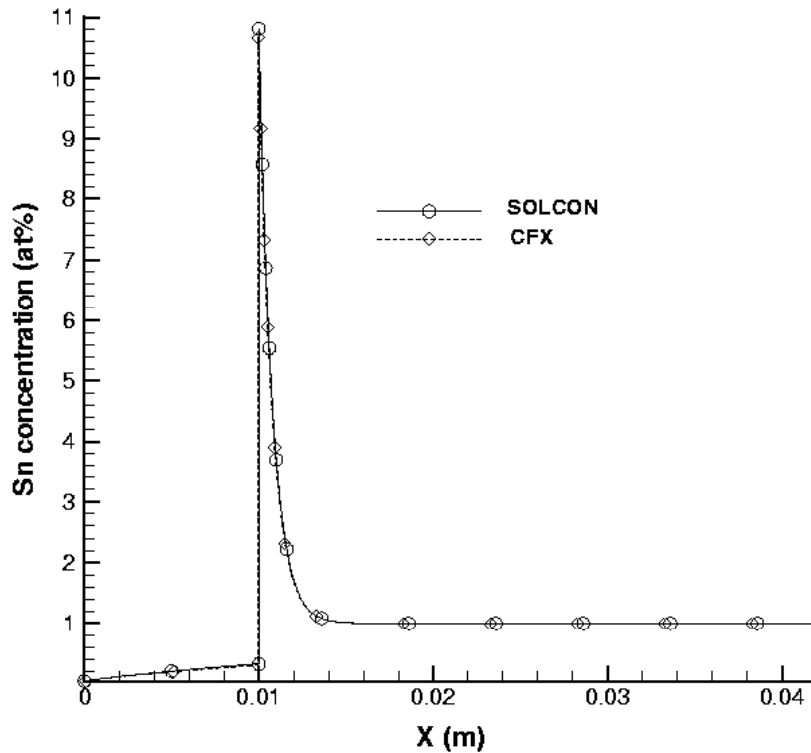


Figure 38. Distribution of solute concentration at the mid-height of the ampoule after 3000 sec of solidification.

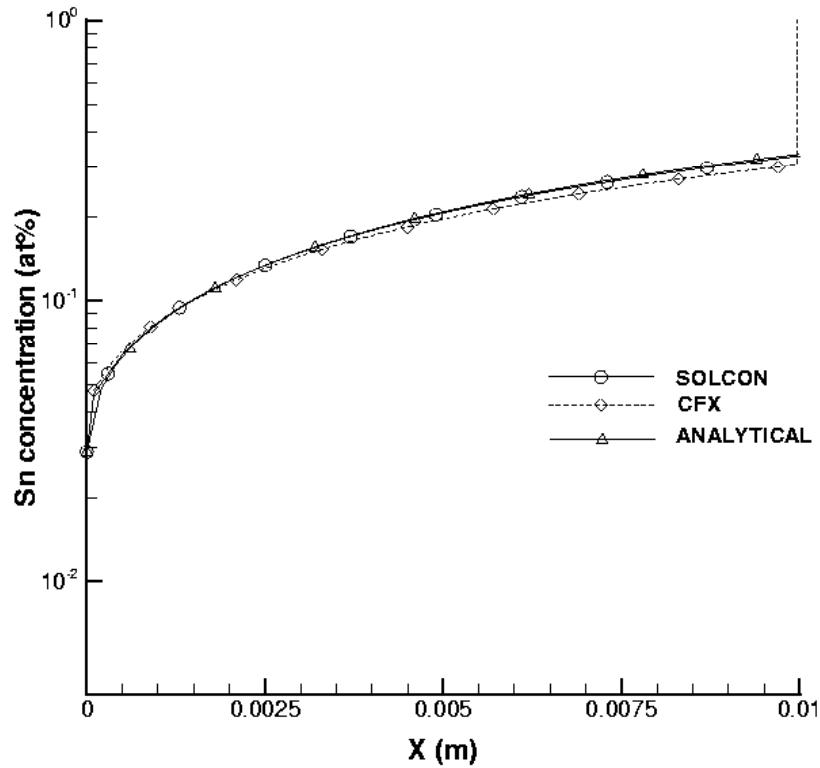


Figure 39. Detailed distribution of solute concentration in the solid part of the sample after 3000 sec of solidification.

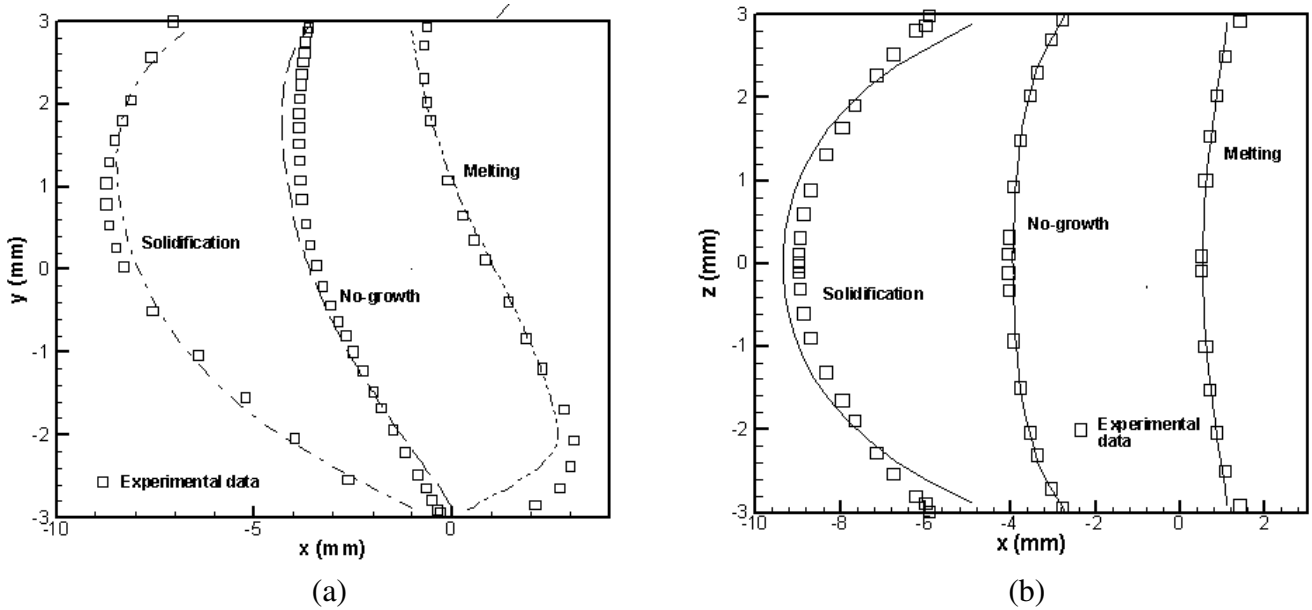


Figure 40. Experimental and computed interface profile at (a) the vertical mid-plane of the ampoule and (b) viewed from above.

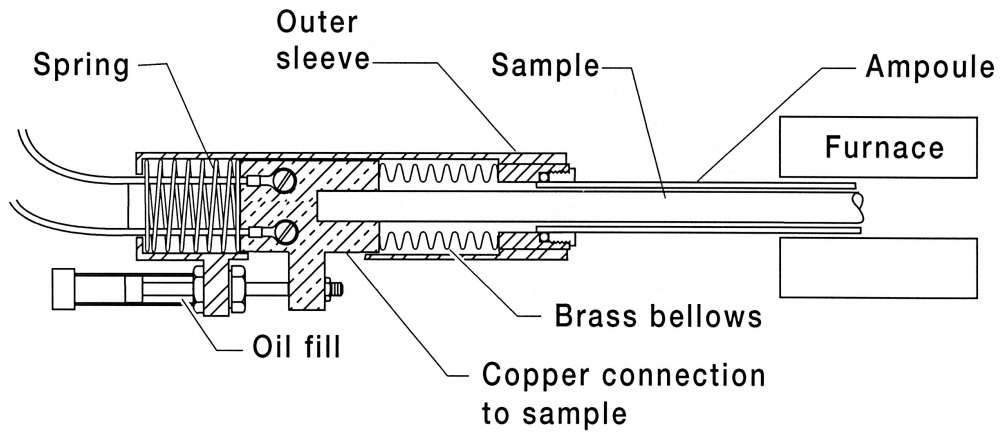


Figure 41. Schematic of the length compensation device used on the MEPHISTO furnace. The spring applies approximately 45 N, pushing on a precision fit piston and rod, which move slowly due to the oil slipping around the tight fitting piston, collapsing the bellows and moving the sample further into the ampoule. The piston moves about 5 mm in compression, to accommodate expansion of the initial solid during heating; then, from the completely compressed position, can move up to about 25 mm.

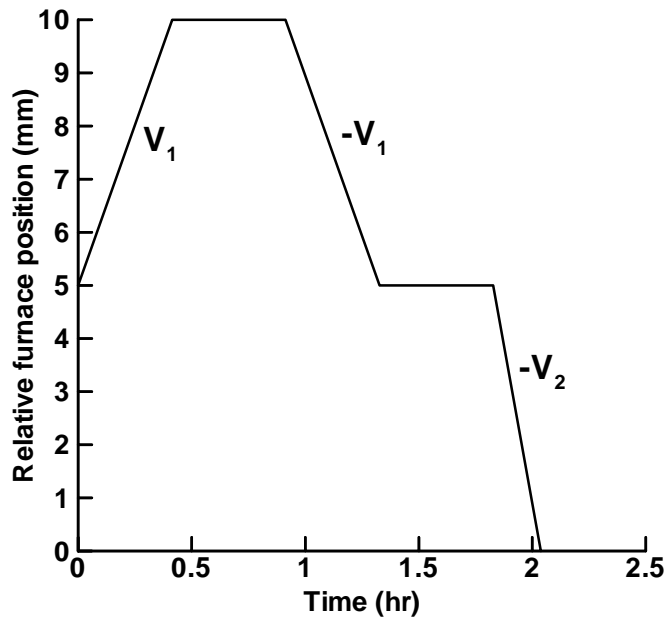


Figure 42. Furnace position as a function of time. V_1 is the furnace velocity during solidification. $-V_1$ and $-V_2$ denote melt stages.

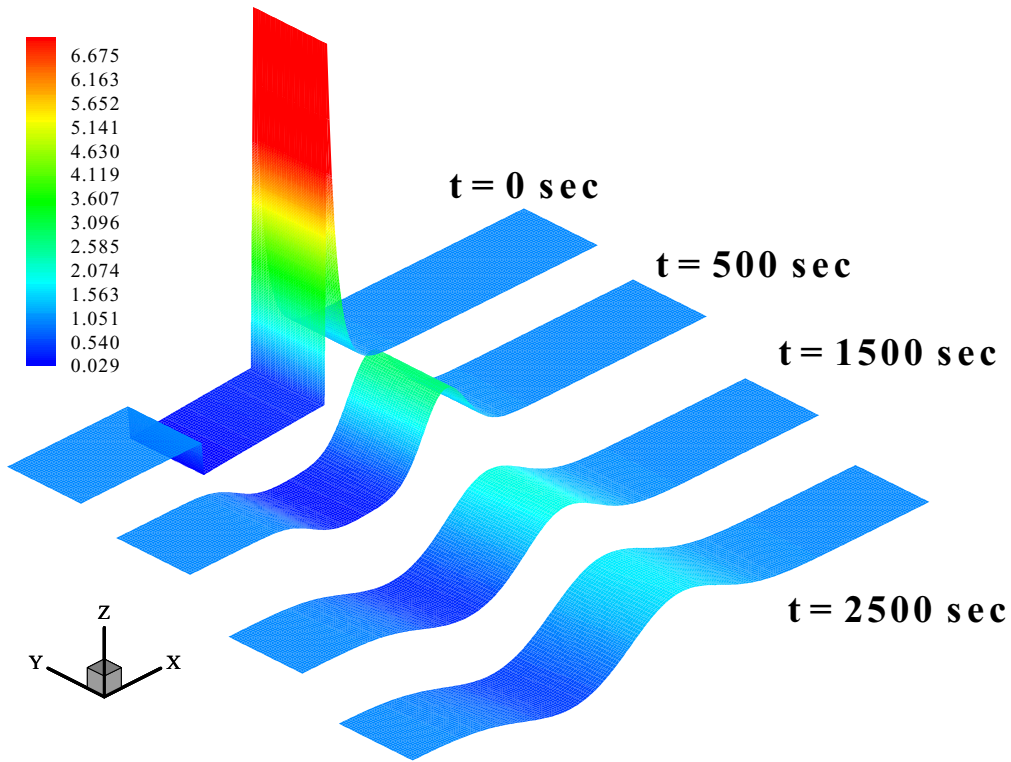


Figure 43(a). Solute concentration decay as a function of time.

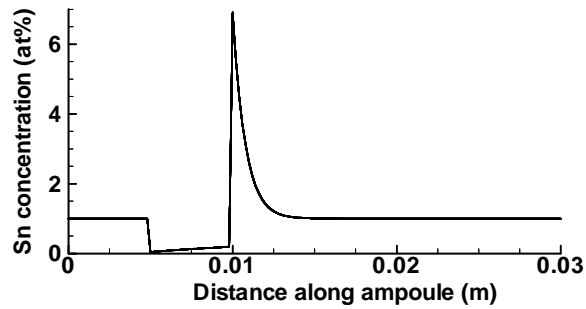


Figure 43(b). Solute concentration along the mid-height of the ampoule after solidification of 5 mm of liquid at $V_1 = 3.34 \mu\text{m s}^{-1}$.

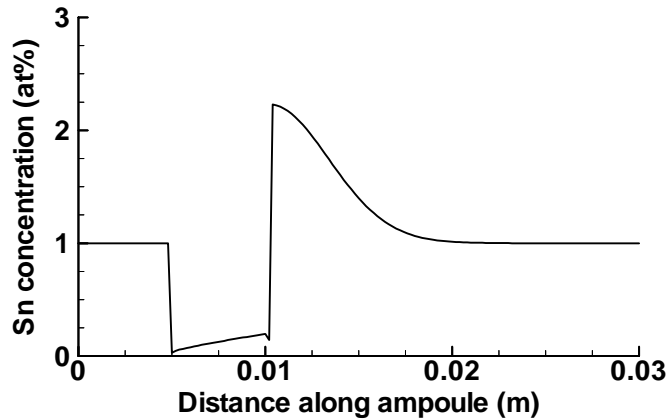


Figure 43(c). Solute concentration along the mid-height of the ampoule following the first 30 min hold.

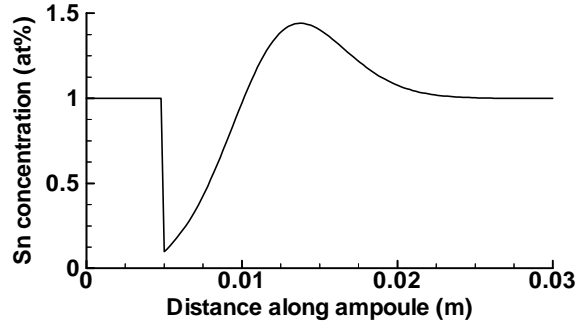


Figure 43(d). Solute concentration along the mid-height of the ampoule after 5 mm of solid has been melted at $V_1 = -3.34 \mu\text{m s}^{-1}$.

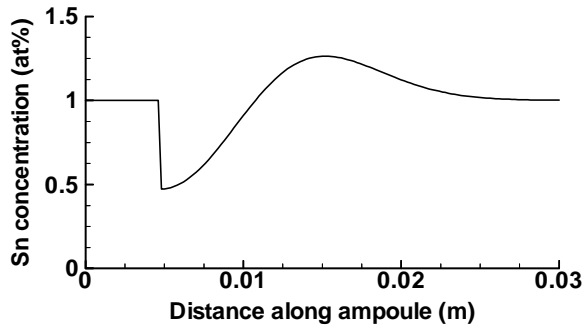


Figure 43(e). Solute concentration along the mid-height of the ampoule following the second 30 min hold.

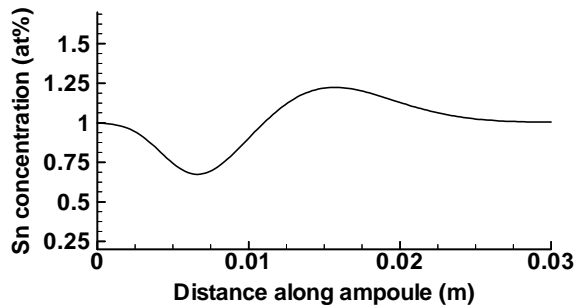


Figure 43(f). Solute concentration along the mid-height of the ampoule after a further 5 mm of solid has been melted at $V_2 = -6.6 \mu\text{m s}^{-1}$.

Level	1	2	3	4	5	6	7	8	9	10	11
C:	0.665	0.721	0.777	0.833	0.889	0.945	1.000	1.056	1.112	1.168	1.224

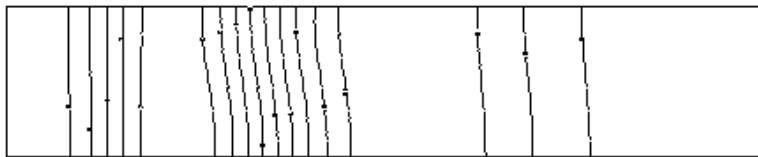


Figure 44. Contours of concentration in the ampoule at the same time as for Figure 43e, showing evidence of transverse (radial) segregation.

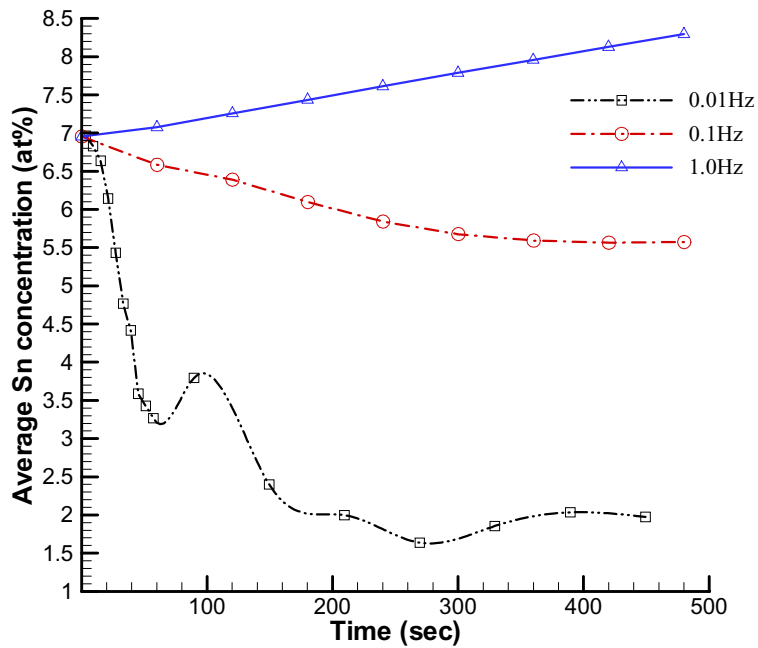


Figure 45. Average concentration at the interface for the disturbances with an amplitude of $10^{-2}g$ and frequencies of 10^{-2} , 10^{-1} and 1 Hz.

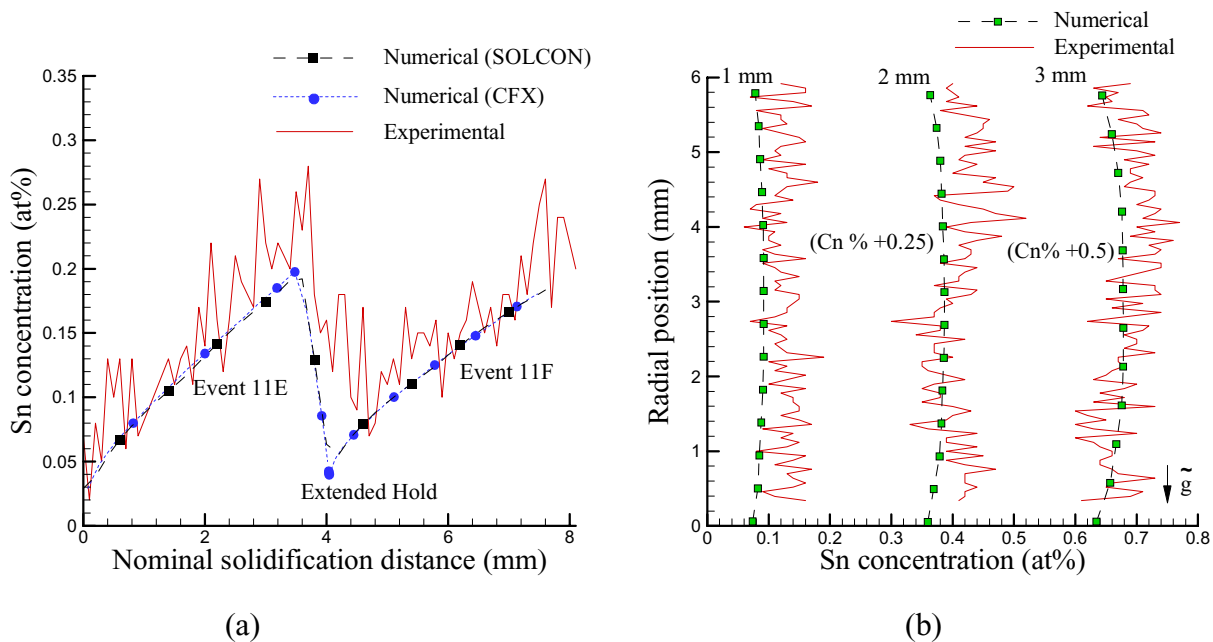


Figure 46. Solute concentration in the solid along the (a) ampoule centre line and (b) across the ampoule for Event 11E and 11F.

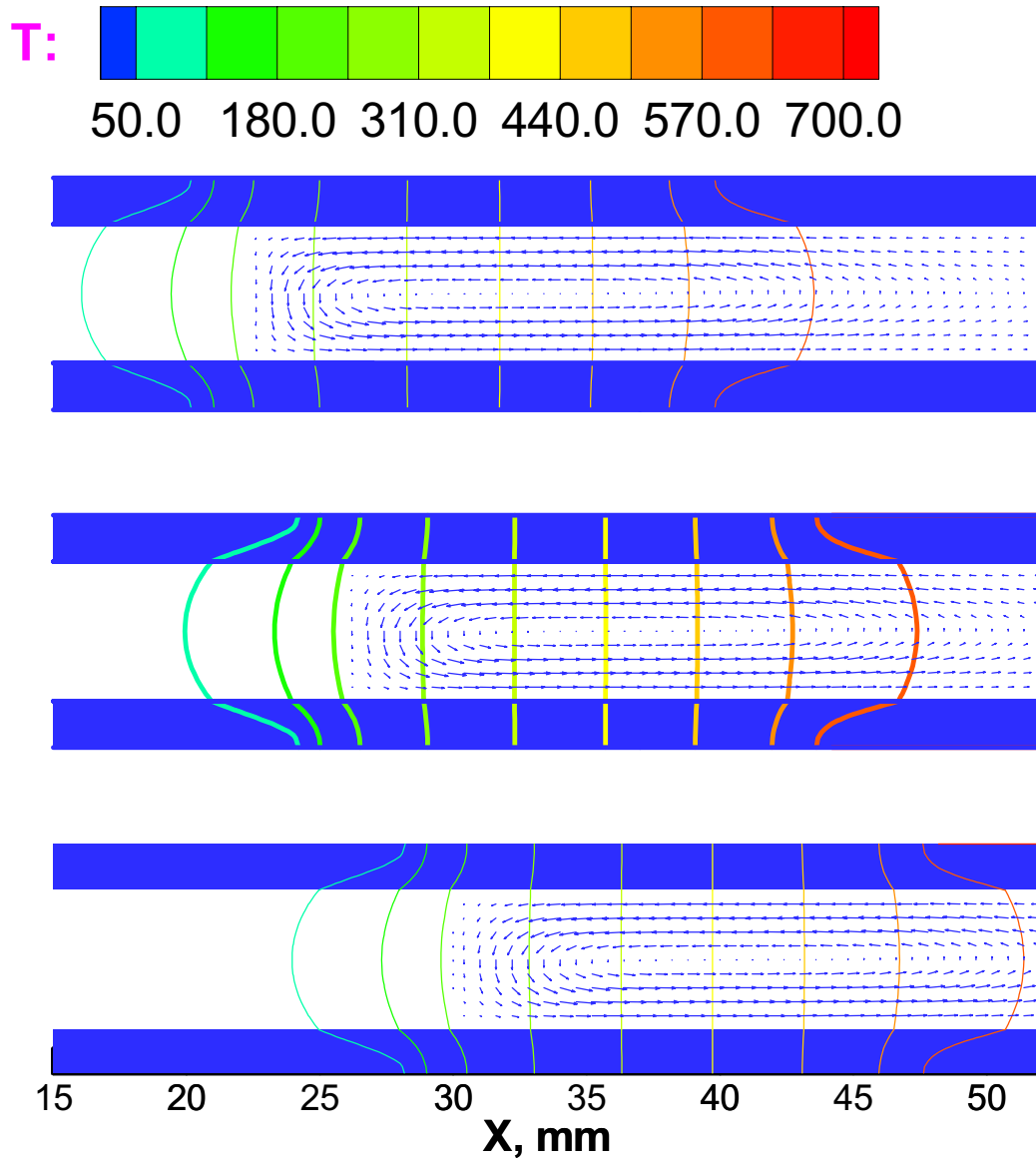


Figure 46(c). Temperature contours and velocity vectors during Event 11E, hold, and Event 11F.

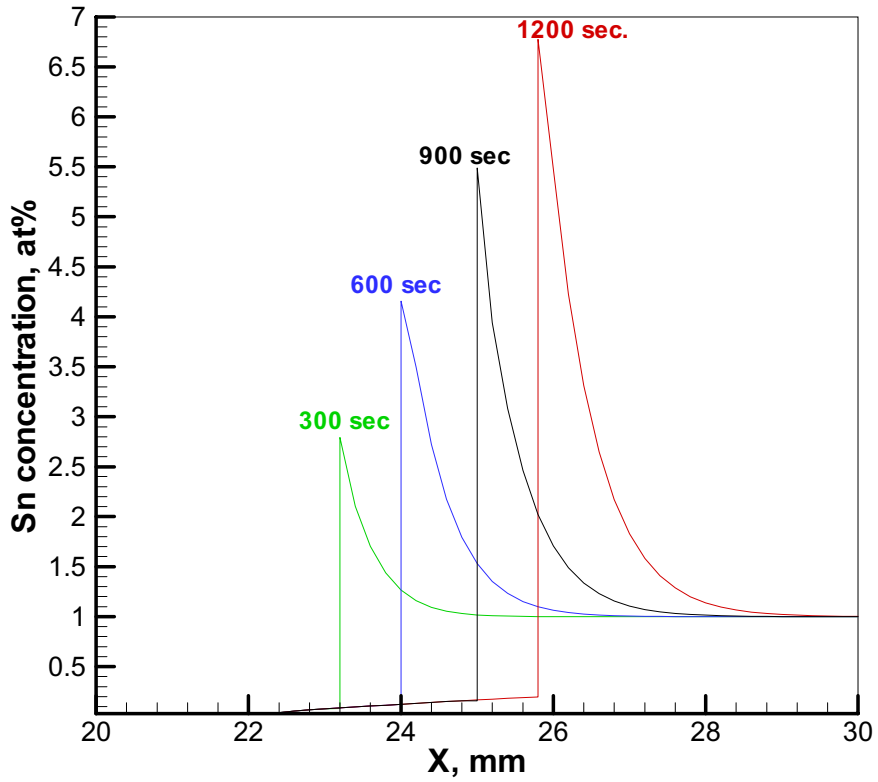


Figure 46(d). Solute build-up during Event 11F solidification.

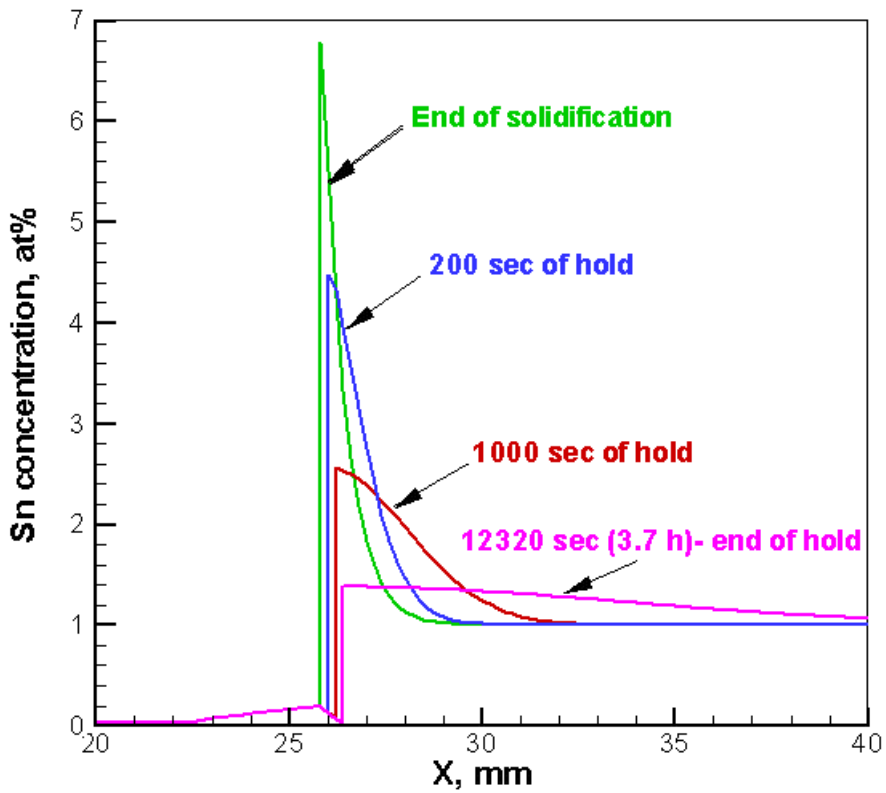


Figure 46(e). Solute decay during extended hold between Event 11E and 11F.

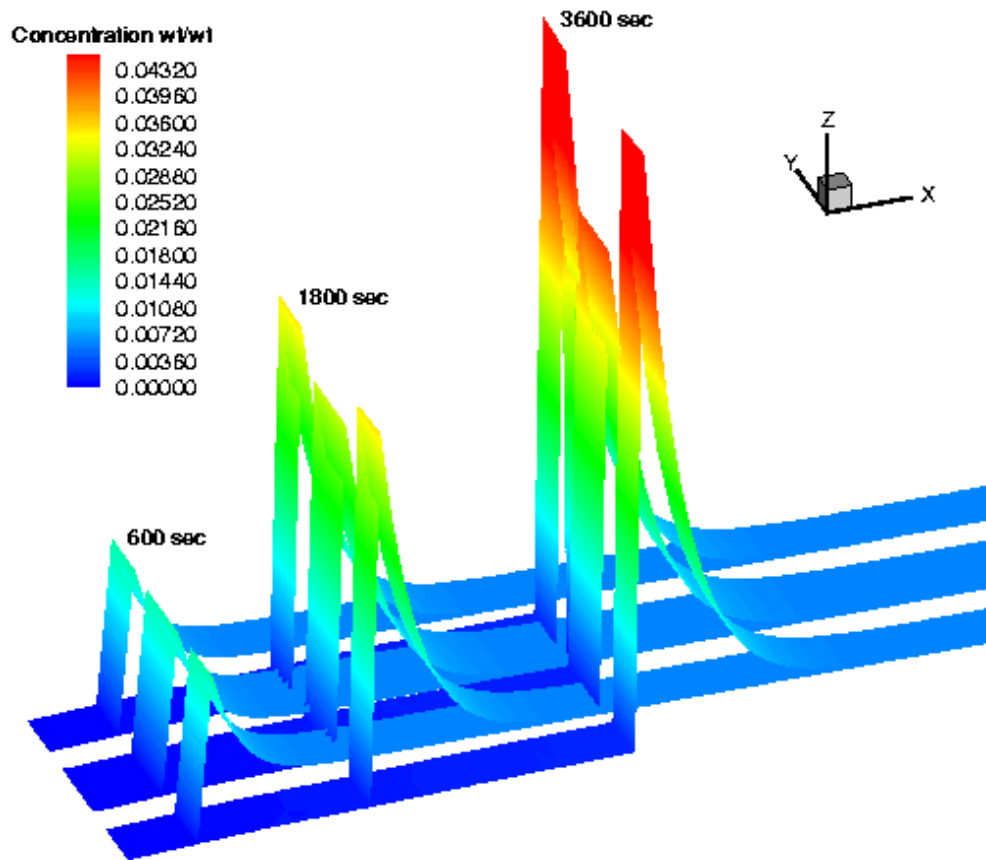


Figure 46(f). Solute build-up inside and outside the capillary.

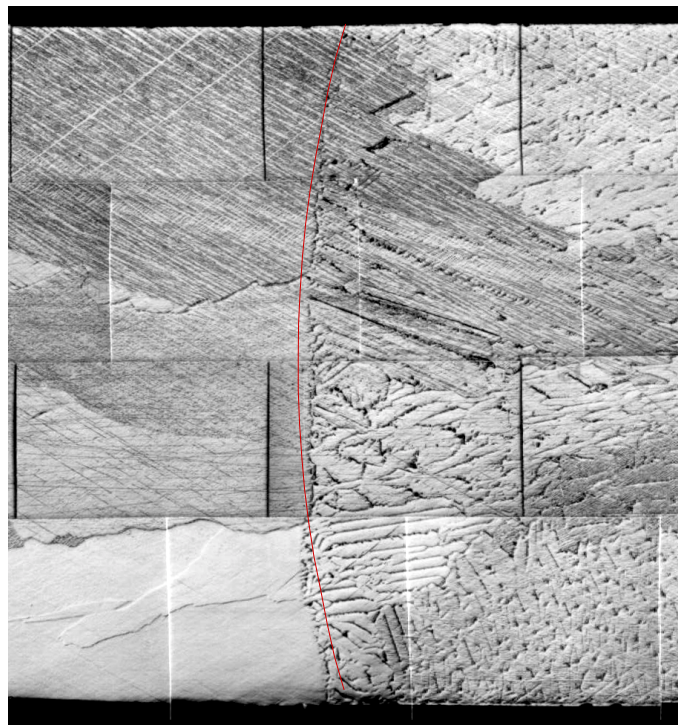


Figure 46(g). Interface Shape.

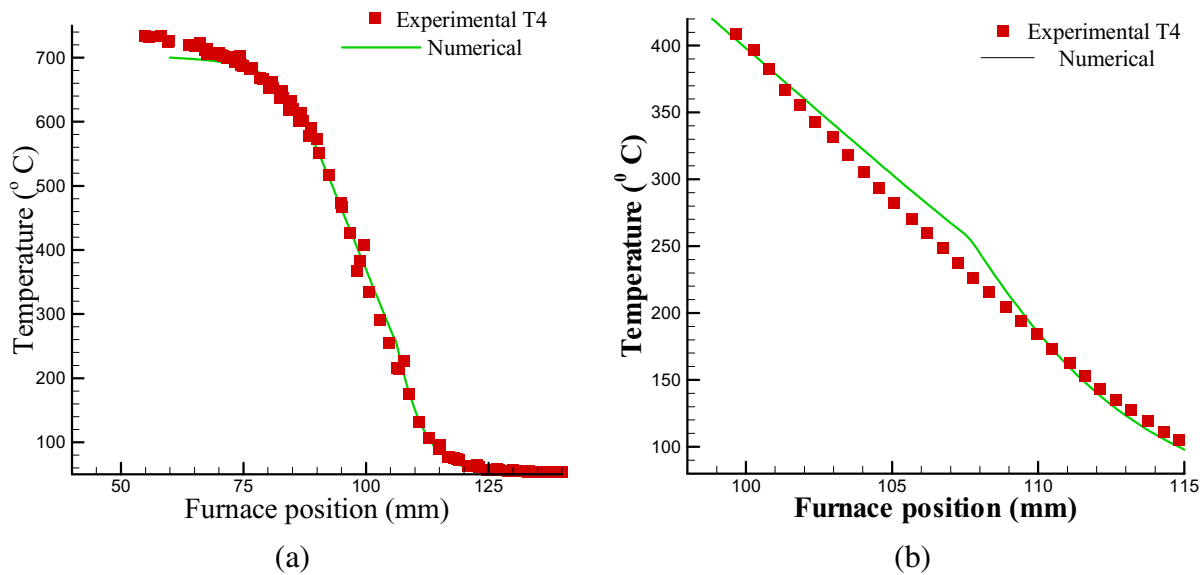


Figure 47. (a) Temperature distribution along the centre line and (b) in the vicinity of interface.

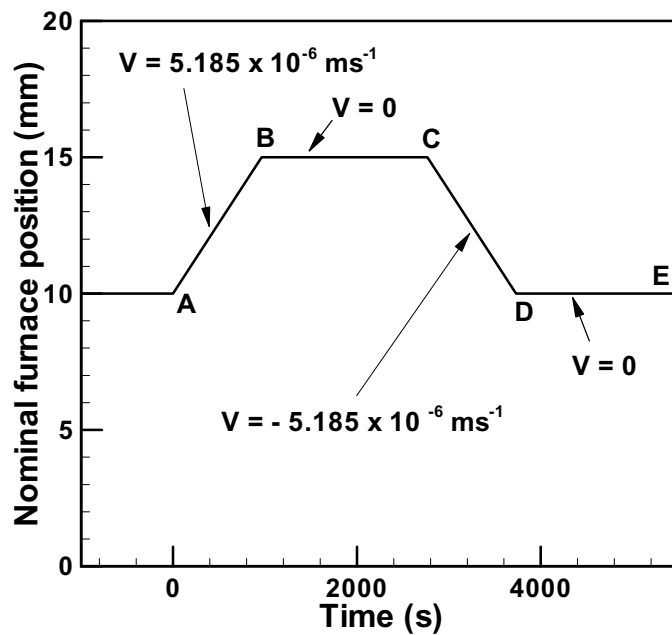


Figure 48. Timeline for the event 9W.

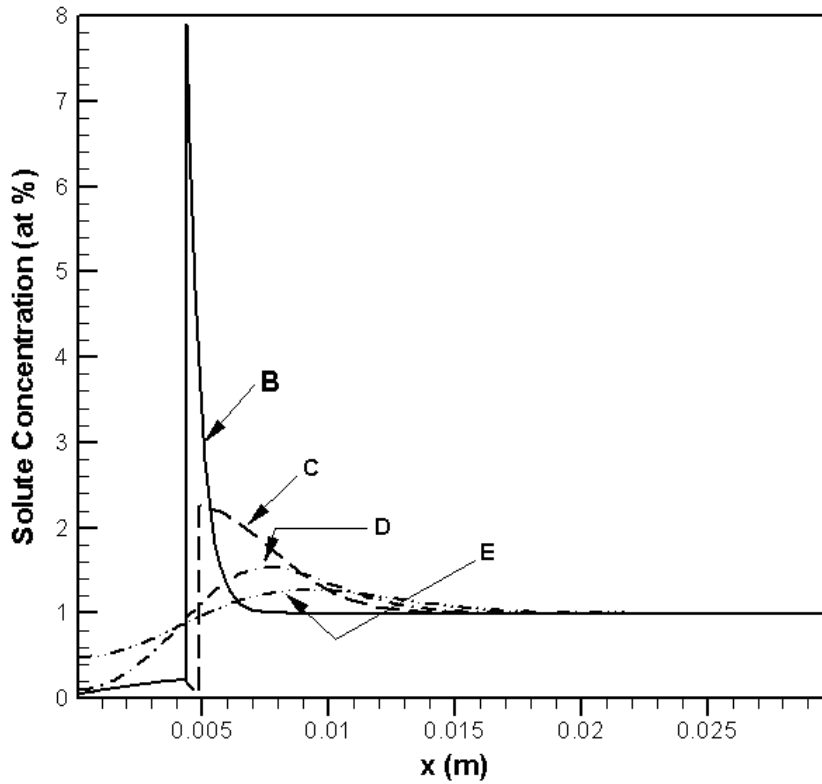


Figure 49. Solute concentration along the horizontal centreline of the ampoule at four different stages of the event.

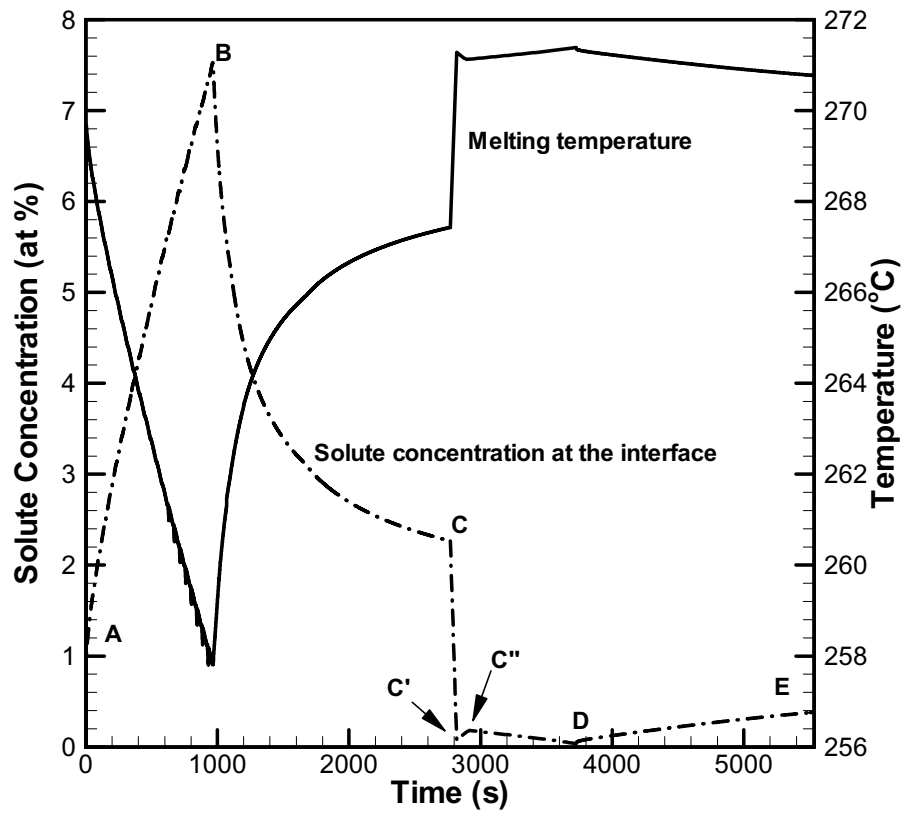


Figure 50. Interface solute concentration and melting temperature at the mid-height of the ampoule.

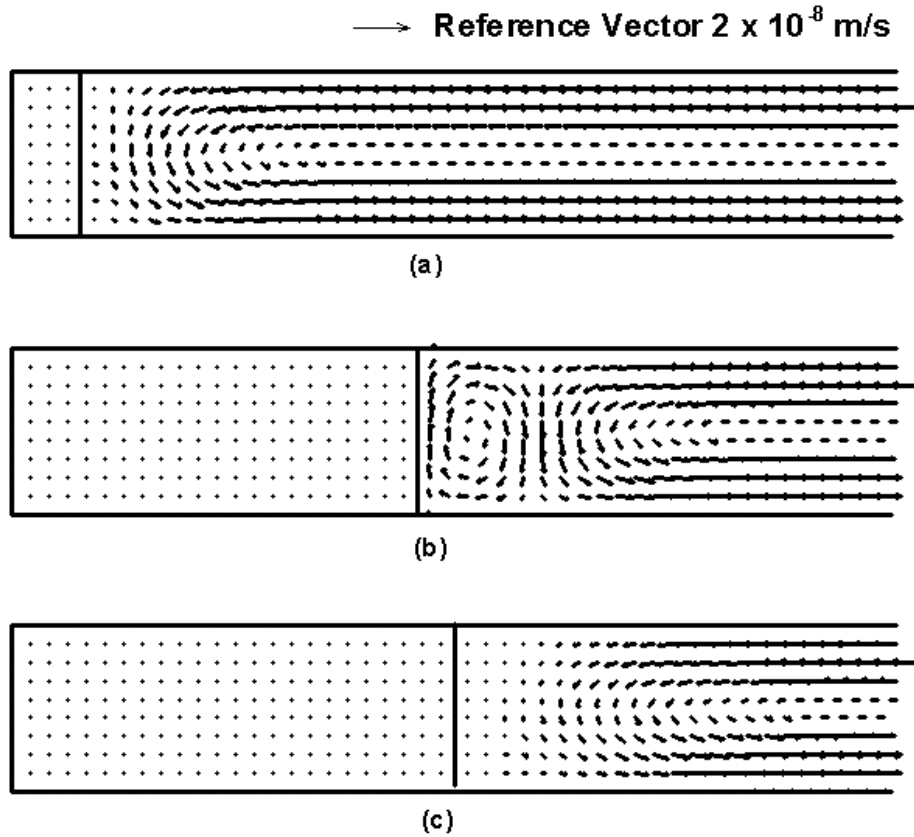


Figure 51. Velocity vectors. (a) early in the solidification; (b) at the end of the solidification; (c) during the first rehomogenization for Event 9w.

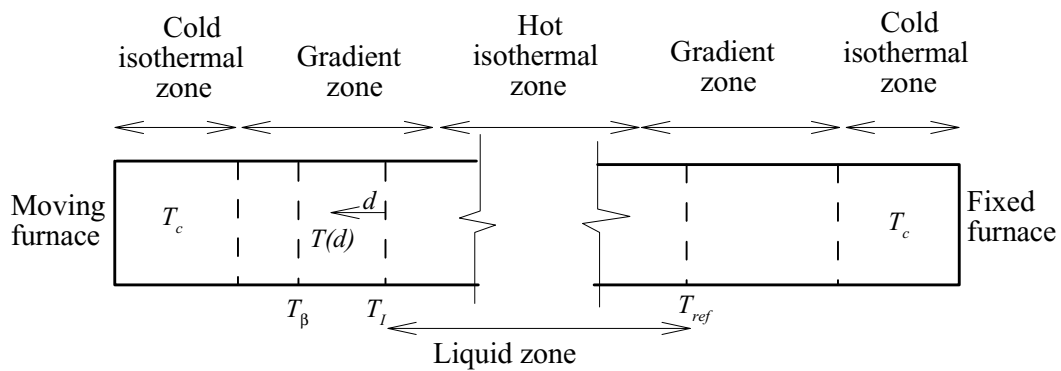
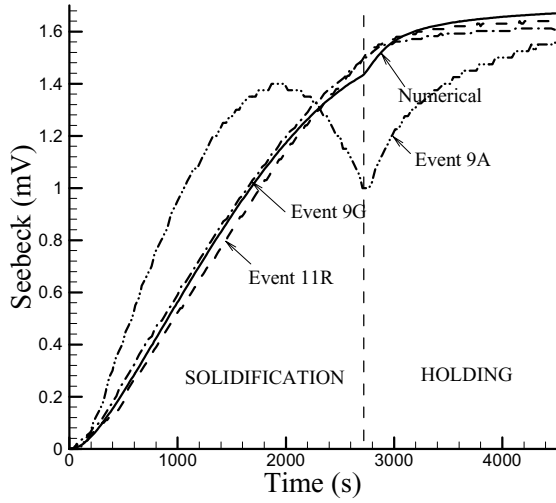
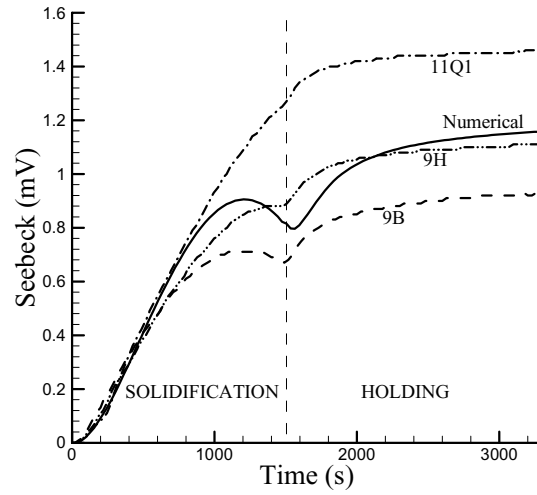


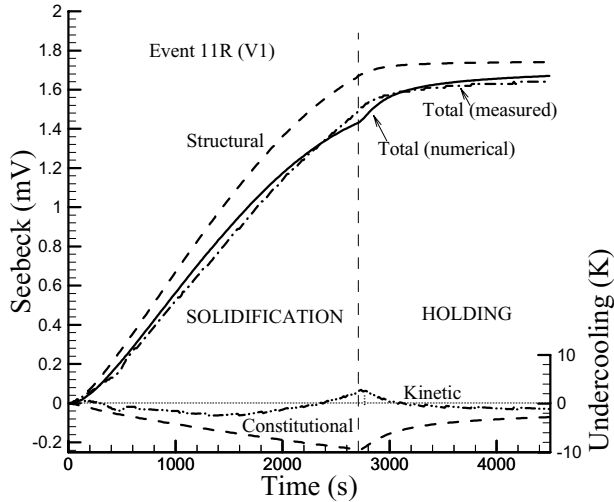
Figure 52. Thermal fields involved in Seebeck signals.



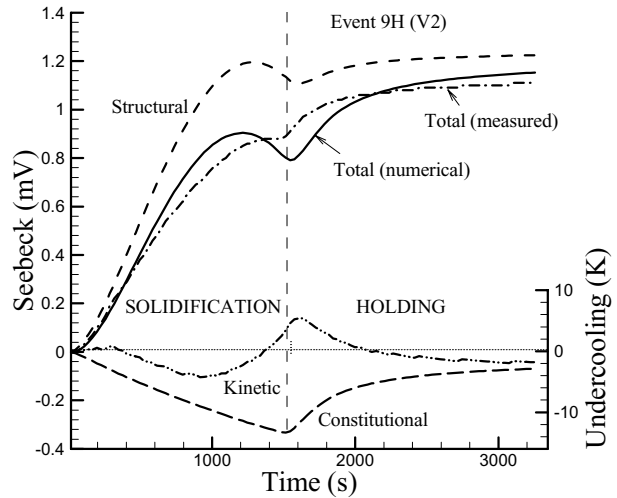
(a)



(b)



(c)



(d)

Figure 53. Seebeck signals (a) V1 events, (b) V2 events, (c) Event 11R and (d) Event 9H.

